

AD _____
(Leave blank)

Award Number: **W81XWH-09-1-0577**

(Enter Army Award number assigned to research, i.e., DAMD17-00-1-0296)

TITLE: **Three Dimensional Projection Environment for Molecular Design and Surgical Simulation**

(Enter title of award)

PRINCIPAL INVESTIGATOR: **Eric Wickstrom, Ph.D.**

(Enter the name and degree of Principal Investigator and any Associates)

CONTRACTING ORGANIZATION: **Thomas Jefferson University**

(Enter the Name, City, State and Zip Code of the Contracting Organization)

REPORT DATE: **August 2011**

(Enter month and year, i.e., January 2001)

TYPE OF REPORT: **Final**

(Enter type of report, i.e., annual, midterm, annual summary, final)

PREPARED FOR: U.S. Army Medical Research and Materiel Command
Fort Detrick, Maryland 21702-5012

DISTRIBUTION STATEMENT: (Check one)

Approved for public release; distribution unlimited

The views, opinions and/or findings contained in this report are those of the author(s) and should not be construed as an official Department of the Army position, policy or decision unless so designated by other documentation.

Table of Contents

	<u>Page</u>
A. Introduction.....	4
B. Body.....	4
C. Key Research Accomplishments.....	34
D. Reportable Outcomes.....	34
E. Conclusion.....	35
F. References.....	36
Appendices.....	37

A. INTRODUCTION

We hypothesized that our fusion of genetic, visual, and tactile information would improve surgeons' understanding of the extent of disease and will ultimately permit surgeons to better plan operations and to prepare for the actual pathology found. We proposed to combine current medical imaging technologies with genetic imaging to leverage our ability to present and use multi-sensory imaging information. We planned not only to view, but also to physically interact with a virtual construct of a specific patient's tissues and organs in a manner that would be immediately intuitive and useful to a surgeon. We hypothesized that *in silico* practice would shorten the time of surgeries and reduce surgical complications. For genetic imaging of pancreatic cancer gene expression, we proposed to design a new ligand for EGFR by molecular dynamics, with haptic sensing of the kinetic binding pathway. For *in silico* practice surgery on an individual patient, we proposed merging of pancreatic cancer PET/CT scans into 3D images, and haptic manipulation of PET/CT pancreatic cancer images.

B. BODY

Task 1.1. Acquisition of molecular dynamics hardware and software (Leads: Wickstrom/Thakur)

Milestone 1.1.1. Acquisition and installation of computer plus Amber 10 molecular dynamics software packages. Quotes will be obtained, permission from TATRC will be requested, purchase orders will be issued, computer hardware and software will be received, installed, and put into operation.

- Amber 10 [4] acquired and installed on Linux 64-bit High Performance Computer Cluster "Egypt" at TJU.
- VH Dissector and 3D Slicer [5] acquired and installed on existing Dell Inspiron 531.
- The volumetric-haptic 3DBoxx 8570 computer system "Kollman" was delivered from Boxx Technologies on 12 Feb 2010. Through negotiations, we spent about half as much as originally budgeted for the 3D haptic system.
- 3D projections of peptides (Fig. 1), PNAs, and RNAs on Kollman with PyMol were sharp and clear from across Room 209 when wearing the specified white light-controlled 3D glasses.

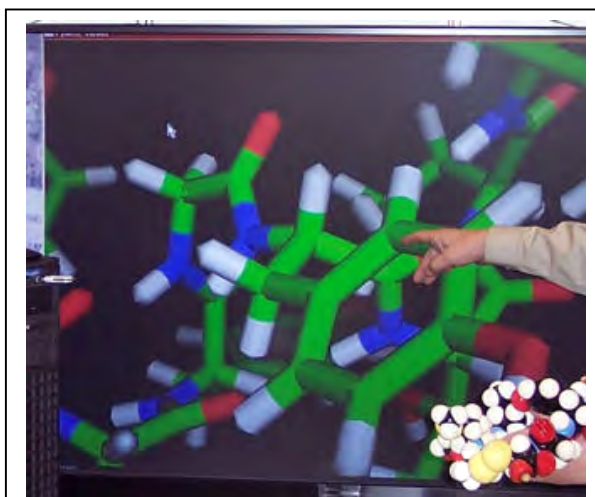


Fig. 1. 3D projection of EGF20-31, after energy minimization, on the 3D Boxx 8570 Kollman at TJU.

- 3D Slicer [5], Amber 11 [4], and Amira 5 (<http://www.amira.com/amira.html>) acquired and installed on Kollman and on Egypt.

Task 1.2. Molecular design of EGFR ligand for gene imaging probe (Leads: Wickstrom/Thakur)

Milestone 1.2.1. Selection of ligand for EGFR uptake of gene imaging probe. In view of the widespread overexpression of EGFR on cancer cells, generating a successful endocytic analog of EGF for mounting on our mRNA probes could expand the spectrum of cancers for imaging. EGFR, (ErbB-1, Her-1), is a 1250-aa, 165 kDa transmembrane glycoprotein tyrosine kinase cell surface protein that binds EGF, a 53-aa, 6 kDa extracellular signaling peptide. Based on the existing crystal structure of EGF-EGFR, we will select a peptide loop of EGF that interacts with EGFR as our first candidate ligand.

- EGF central loop, amino acids 20-31, CMYIEALDKYAC, with Cys-Cys disulfide bridge between Cys20 and Cys31 (Fig. 2B), was selected in Q1 from the crystal structure [1] as the first candidate ligand. The linear version (Fig. 2A) is expected to serve as a control.
- EGF amino acids 32-48, NCVVGYIGERCQYRDLK (Fig. 2C), was selected in Q2 as a second candidate ligand, based on binding to EGFR on cells [2]. Cys-Cys cyclized version (Fig. 2D) also exhibited EGFR binding.
- GE11, YHWYGYTPQNVI, an EGFR-binding peptide identified by phage display [3] (Fig. 2E), was selected as a third candidate ligand, along with its Cys-Cys cyclized version (Fig. 2F).

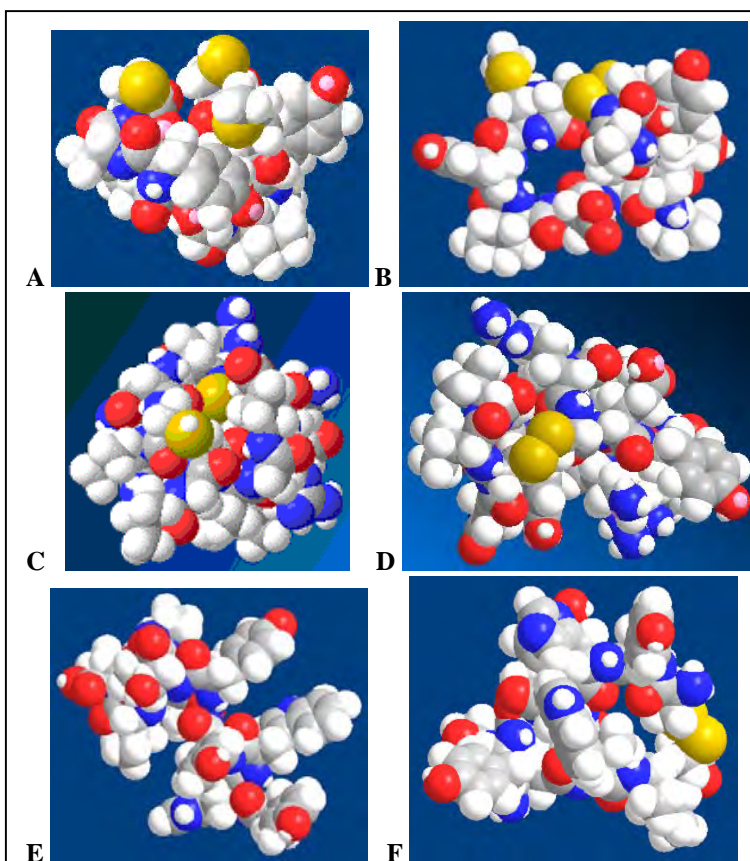
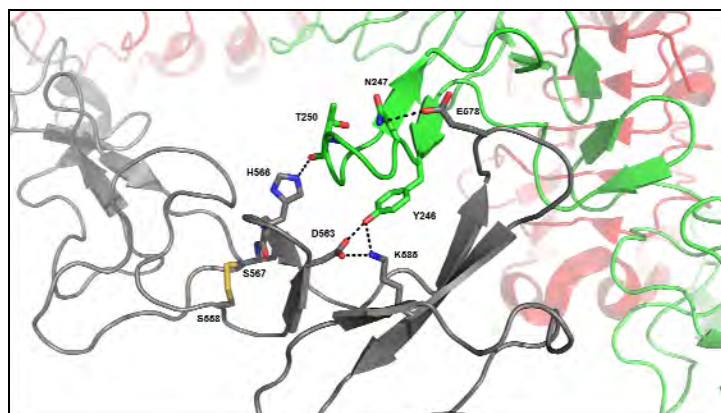
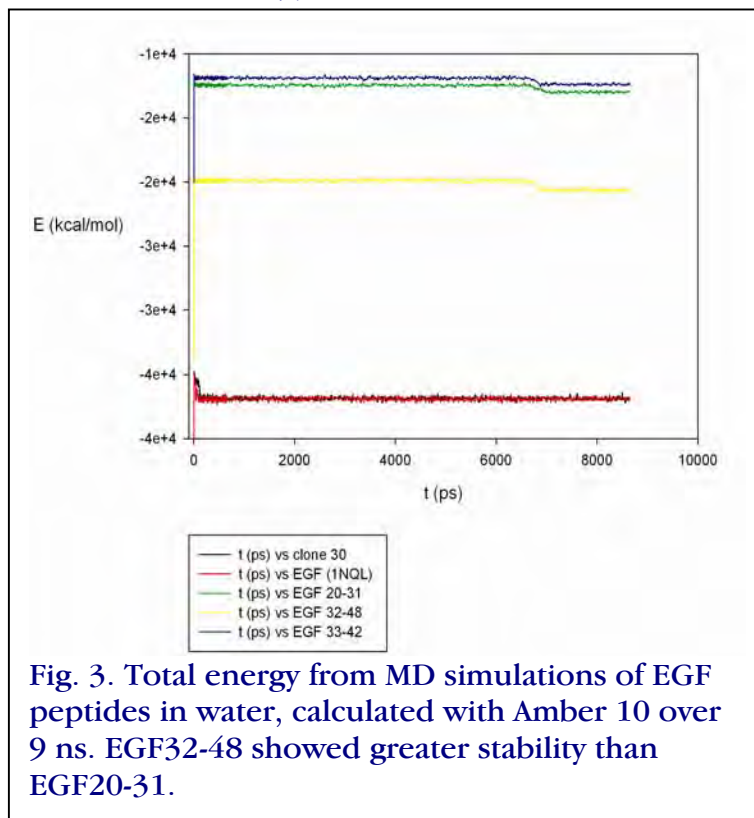


Fig. 2. Potential EGF ligands, energy-minimized by molecular dynamics in Chem3D. A, EGF20-31 selected from crystal structure [1]; B, cyclized EGF20-31; C, EGFR-binding EGF32-48 identified by cell binding [2]; D, latter peptide cyclized via Cys33 and Cys42; E, EGFR-binding peptide identified by phage display [3]; F, latter peptide cyclized by N and C terminal cysteines.

Milestone 1.2.2. Molecular dynamics calculations of selected EGFR ligand binding (1000 ps minimum energy). Calculation of the most probable structure of the selected EGFR ligand in water will predict its ability to bind to its intended EGFR target. Using Amber 10 in house, or on Salk at the Pittsburgh Supercomputer Center, we will calculate the potential function, $U(x)$, and solve the negative gradient of the potential energy function, $-\nabla U(x)$, along the kinetic docking pathways for the selected peptide loop of EGF that interacts with EGFR, at every 1 Å of separation between the peptide and EGFR from 30 Å out to 0 Å, the final docked state. Using the two manipulators, we will guide the candidate peptide into the EGFR binding site, from 30 Å separation to 0 Å, with haptic responses controlled by the docking calculations. We will sense kinetic barriers, or difficult rearrangements, through our hands, as well as by examining the numbers from the calculation. The criterion

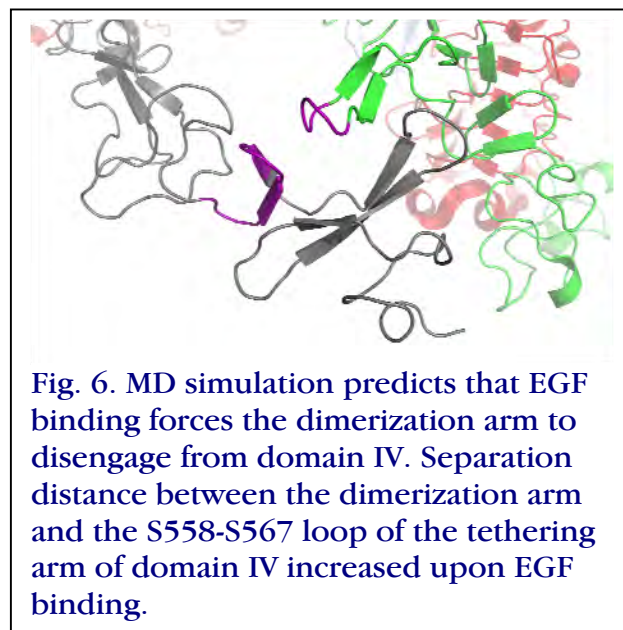
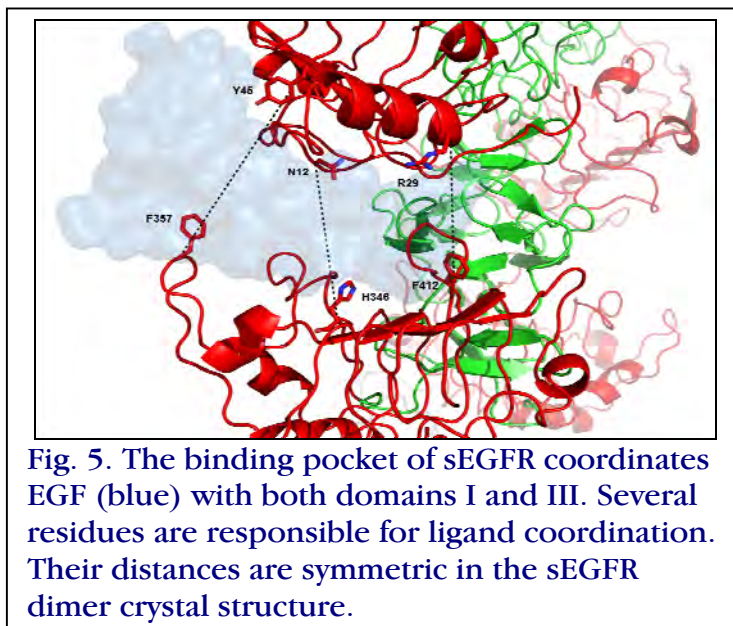
for favorable energetics of binding to EGFR will be a predicted $K_d < 100$ nM. Unfavorable energetics would be indicated by a predicted $K_d > 1 \mu\text{M}$.

- Molecular dynamics simulations of EGF and EGF peptides over 9 ns were performed for the fragments chosen in Fig. 2, in the presence of explicit water molecules. Large scale Amber 10 calculations required use of Salk at the Pittsburgh supercomputer system. Total energy plots were constructed to evaluate stability of each peptide in



explicit solvent. EGF 32-48 had the lowest peptide fragment energy after equilibration and the high affinity mutant EGF had a profile similar to that of wild type EGF (Fig. 3). The increase in energy most likely results from increased entropy due to size and amino acid composition of each cyclic peptide. EGF32-48 has two tryptophans near the C terminus that may participate in base stacking, decreasing entropy and stabilizing its structure.

- Minimum energies of the extracellular ligand binding domain of EGFR, with and without EGF bound, were calculated in the presence of water with Amber 11 [6] (Appendix). We demonstrated that EGF binding to the extracellular domain of EGFR (sEGFR) disrupts auto-inhibitory intramolecular interactions (Fig. 4) by increasing the distance between the so-called “dimerization arm” and domain IV (Fig. 5). To investigate early ligand binding effects on sEGFR dimers, we constructed a singly ligated sEGFR dimer for simulation. MD simulations of the singly ligated sEGFR dimer exhibited asymmetrical motion in each monomer and a decrease in the size of the second EGF binding pocket by 10 Å (Fig. 6). Free energy calculations indicated that asymmetrical dimerization with only one EGF-sEGFR monomer is more energetically favorable than dimerization of two ligated sEGFR monomers by 2.88 kcal/mol.
- The molecular dynamics docking pathway of EGF into the ligand binding pocket of EGFR was then calculated with ZDOCK, an online server that performs rigid body docking calculations and determines their relative energies in implicit water with the appropriate dielectric constant, on Salk at the Pittsburgh supercomputer system (Fig. 7). We discovered that the entire kinetic docking pathway could be calculated in a single run, beginning with EGF outside of the EGFR ligand binding site. The ZDOCK force fields were sufficient to draw EGF into the ligand binding pocket. This insight eliminates the need for separate



calculations over a series of specific separations.

- MD simulations for EGFR complexes with the candidate peptides of Fig. 2 were also performed and energy plots were generated (Fig. 8). The EGFR receptor alone (EGFR apo) displayed the lowest energy, while the two complexes showed slightly increased energies overall. For EGF binding to EGFR, $\Delta G = -68 \pm 10$ kcal/mol. For EGF32-48 binding to EGFR, $\Delta G = -40 \pm 8$ kcal/mol. This could be a result of conformational changes occurring and interactions between the peptides and the receptor. Neither complex underwent substantial conformational changes within this time frame, suggesting that longer simulation times need to be performed in order to capture the receptor activation event. The molecular dynamics insight above that EGFR activation requires a conformational shift that depends on all domains of EGF implies that a single loop of EGF will be insufficient to induce internalization of EGFR with cargo.

Task 1.3. Synthesis and validation of EGFR ligand for gene imaging probe (Leads: Wickstrom/Thakur)

Milestone 1.3.1. Synthesis and purification of chelator-PNA gene probe with selected EGFR ligand (95% homogeneity). The energetically optimal peptide selected above will be extended from a solid phase support by solid phase coupling of Fmoc-L-amino acid monomers. The terminal Cys residues will be cyclized. A diethyleneglycol spacer

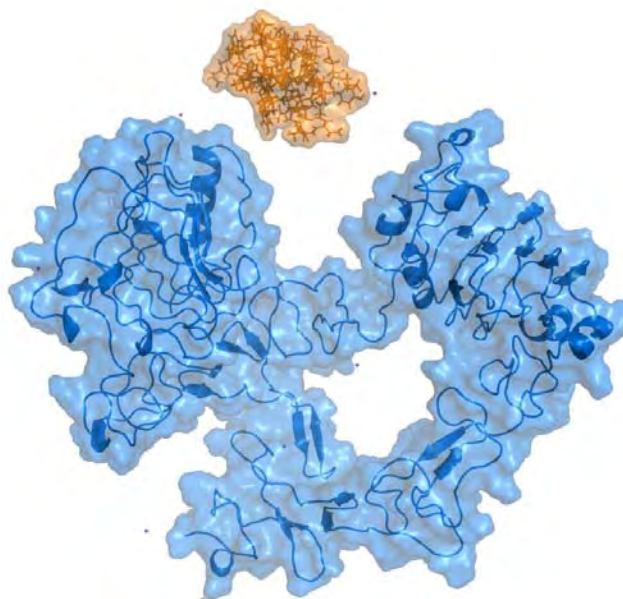


Fig. 7. Graphic image of EGF docking with EGFR at 20 Å out of the ligand binding pocket, during a kinetic docking pathway molecular dynamics energy minimization using ZDOCK on the Salk 64-bit high performance computer of the Pittsburgh supercomputer system. This structure was reached after 250 ns of motion

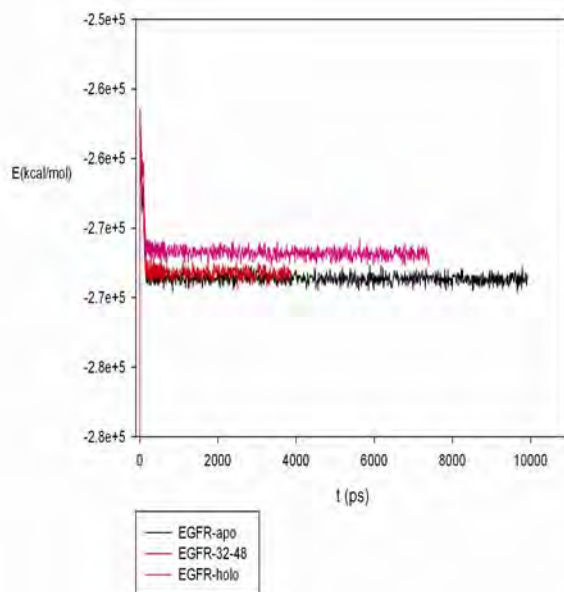
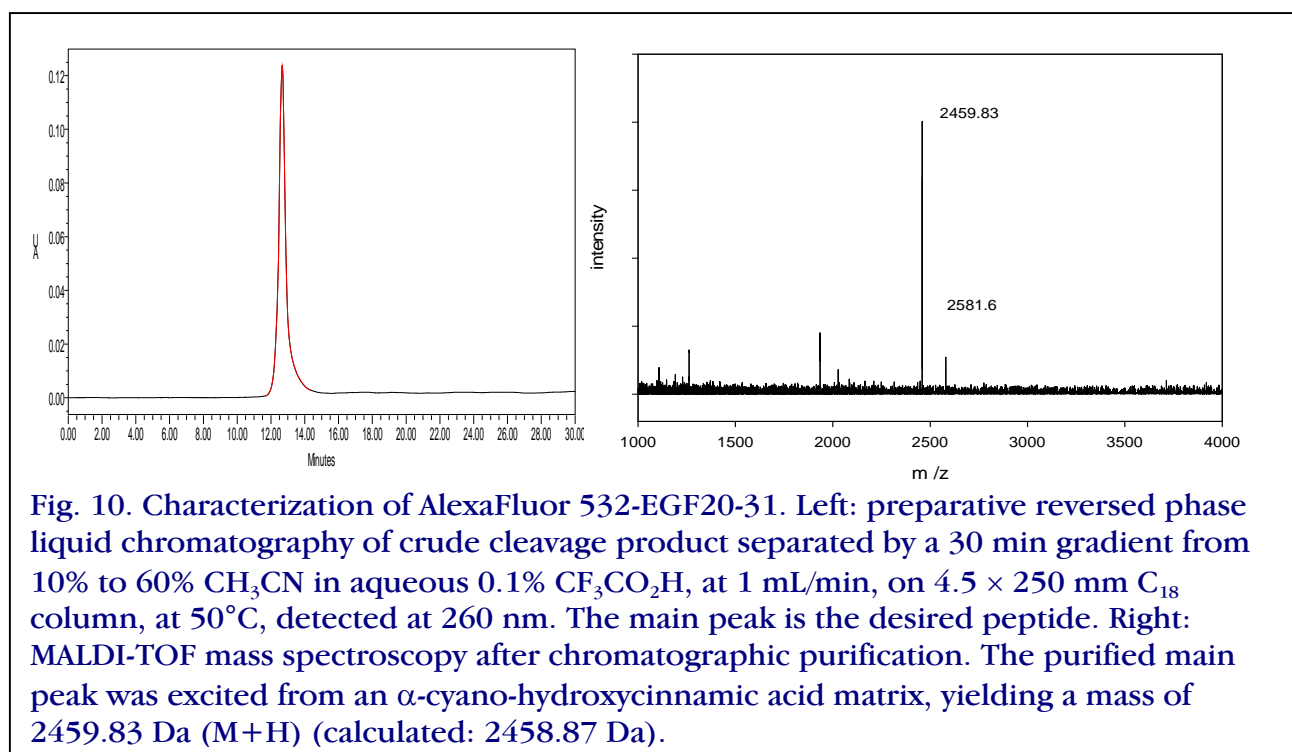
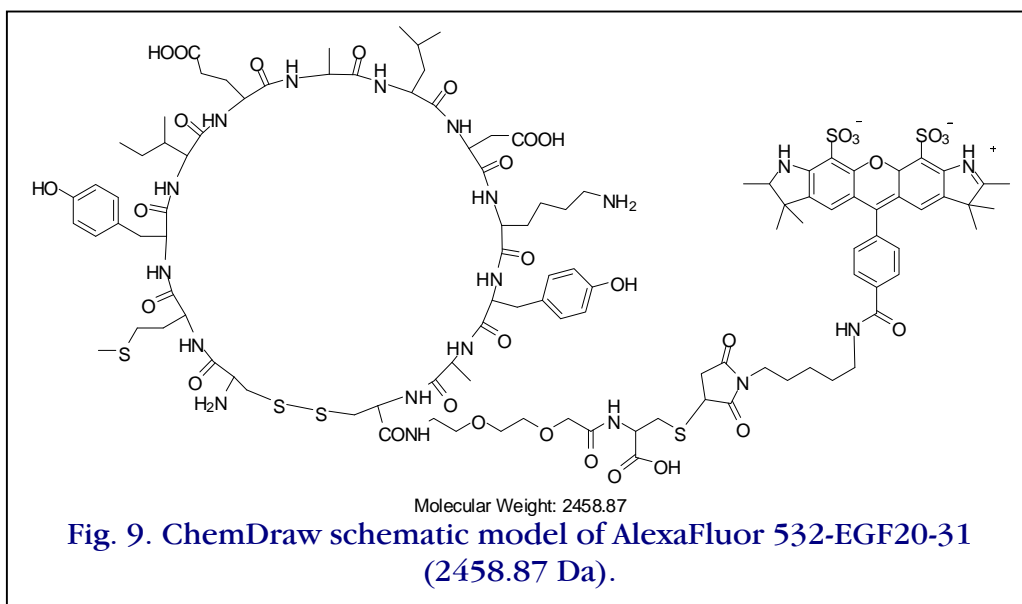


Fig. 8. Total energy from MD simulations of EGF and EGF32-48 interacting with EGFR in water, calculated with Amber 10 over 4-10 ns.

will be coupled, followed by the *KRAS2* G12D PNA sequence, a second diethyleneglycol spacer, then a DOTA chelator. The finished DO3A-PNA-peptide will be cleaved from the solid support, deprotected, purified by reversed phase liquid chromatography, and analyzed by mass spectroscopy to determine whether the desired sequence was synthesized correctly.

- AlexaFluor 532-EGF20-31 (Fig. 9) was synthesized by solid phase coupling. HPLC and MS (Fig. 10) were satisfactory.



- AlexaFluor 532-EGF32-48 (Fig. 11) was synthesized by solid phase coupling. HPLC and MS (Fig. 12) were satisfactory.

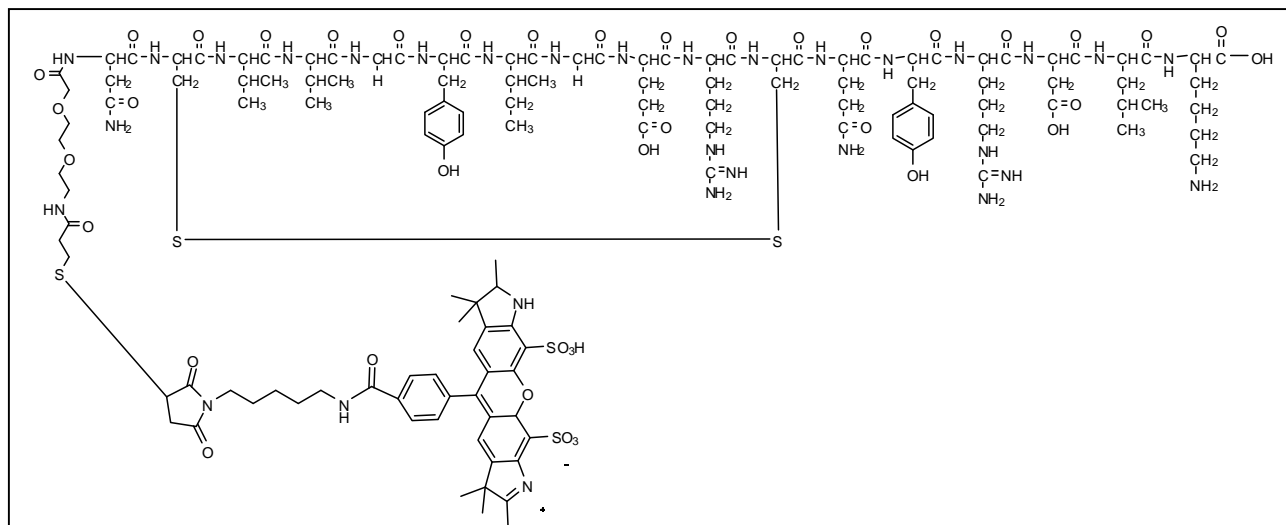
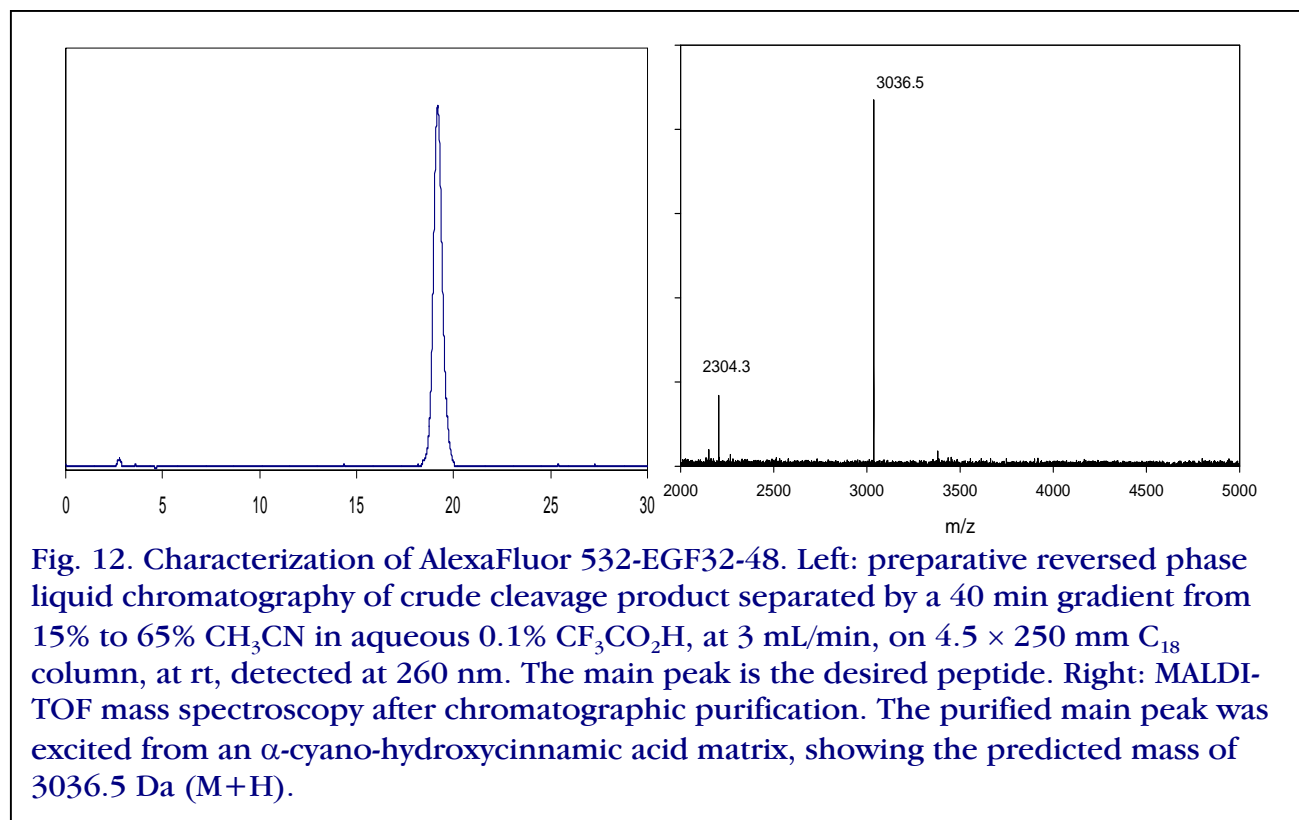
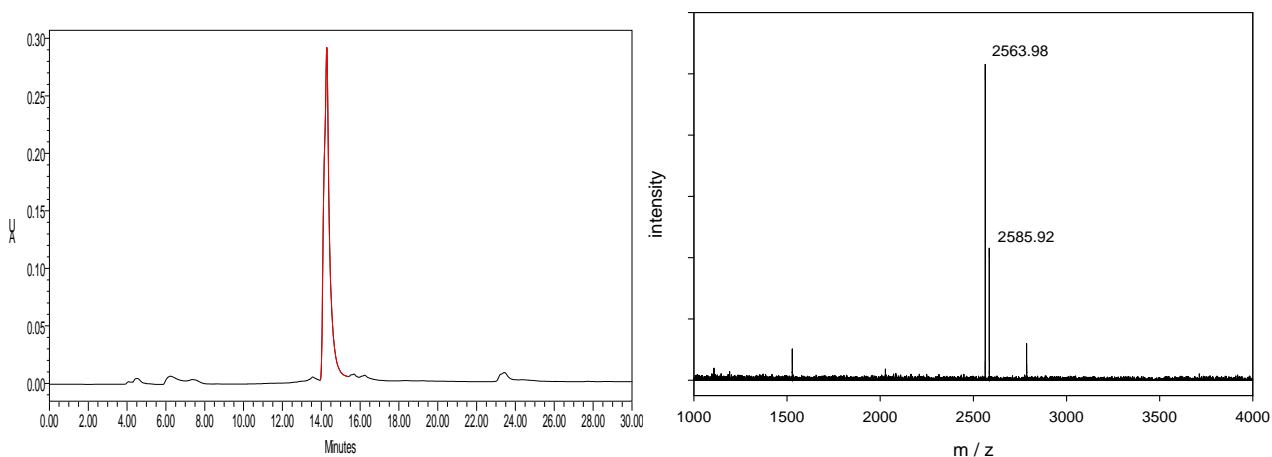
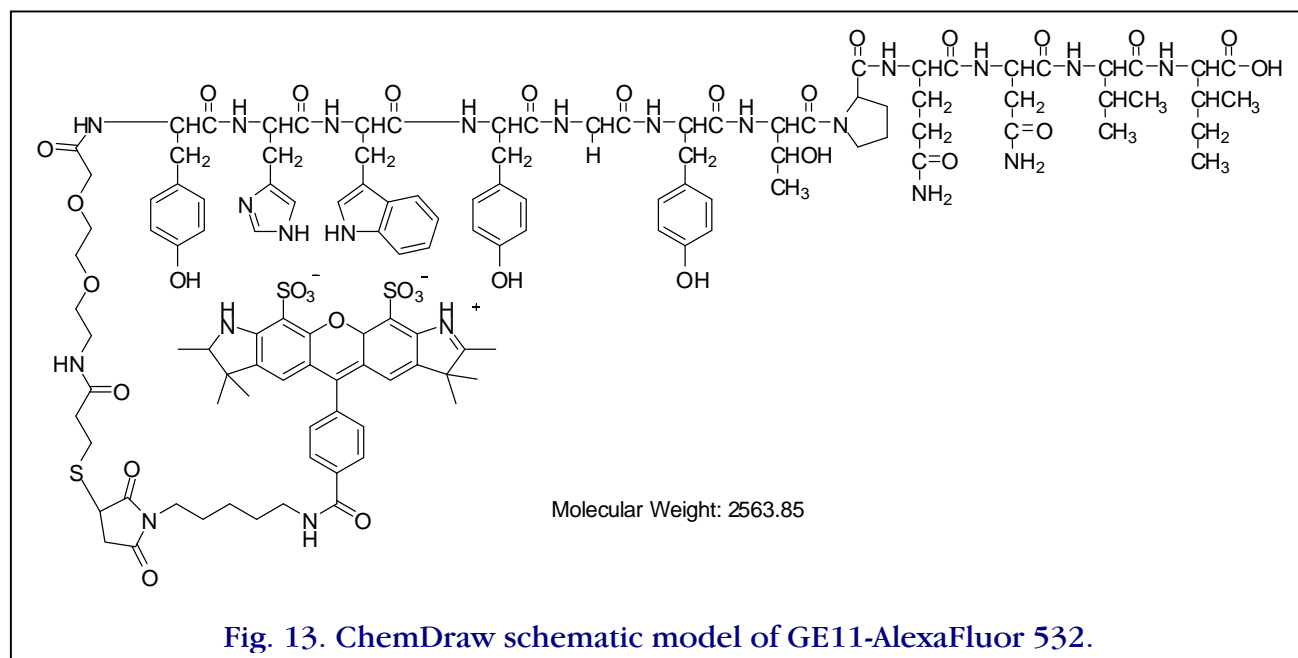


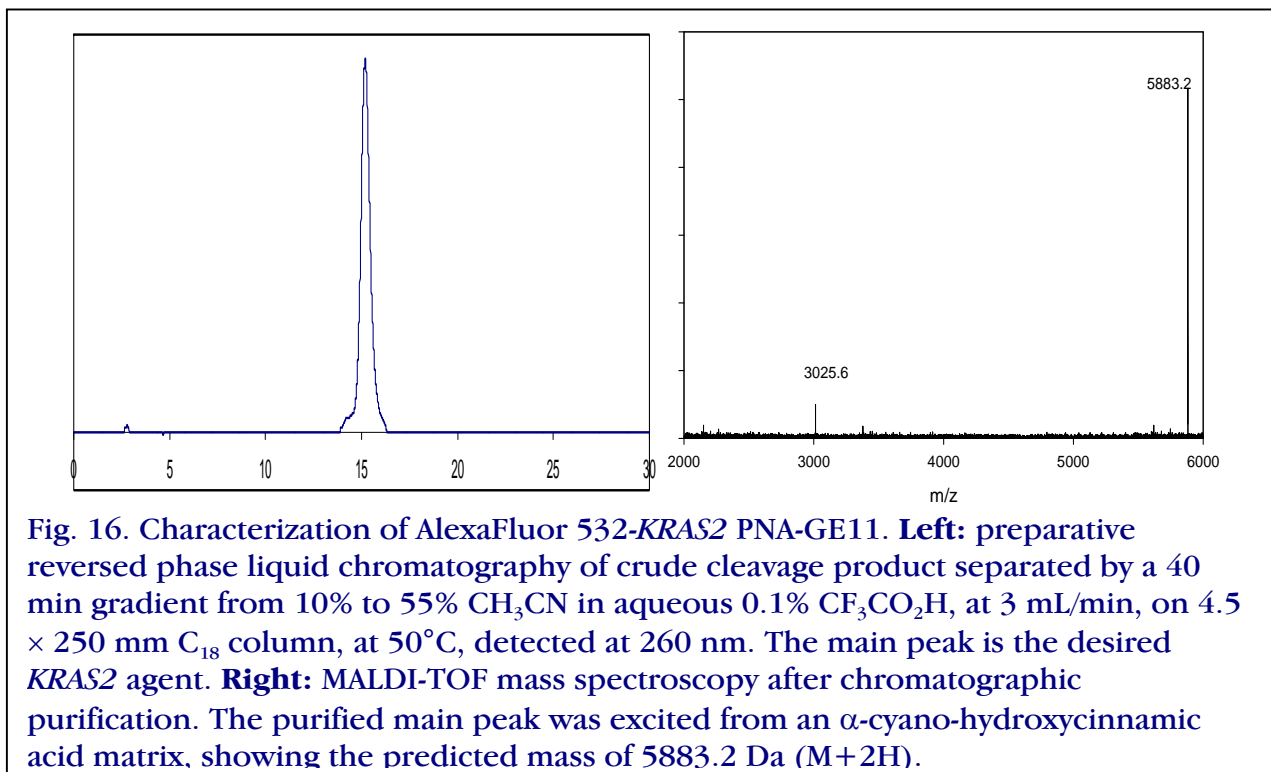
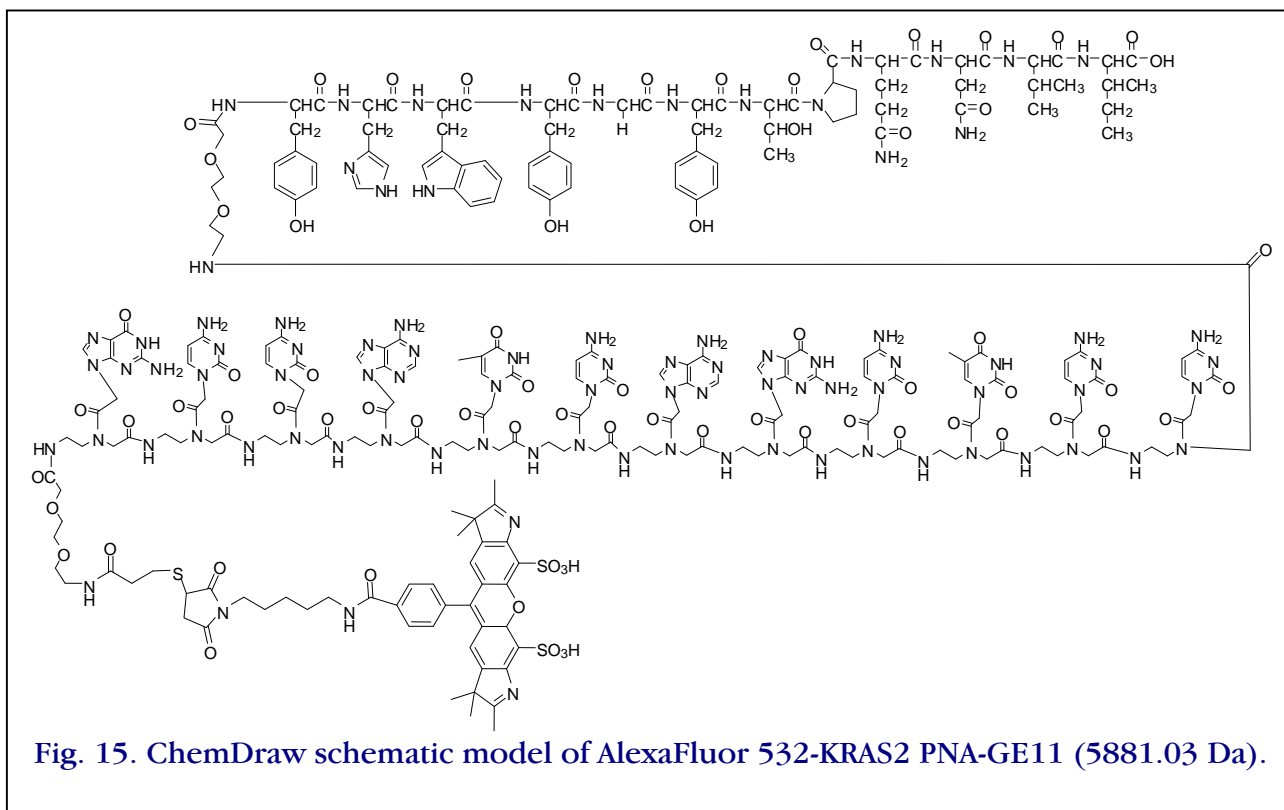
Fig. 11. ChemDraw schematic model of of AlexaFluor 532-EGF32-48 (3035.26 Da).



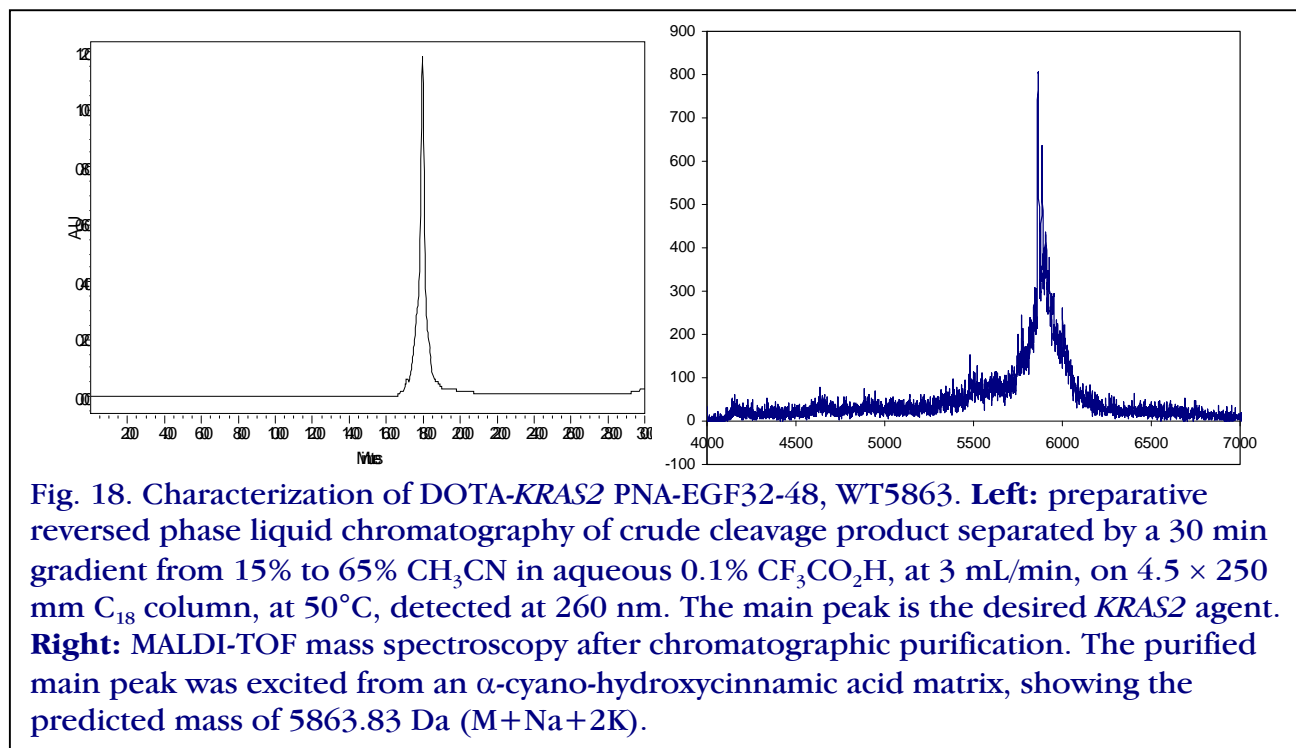
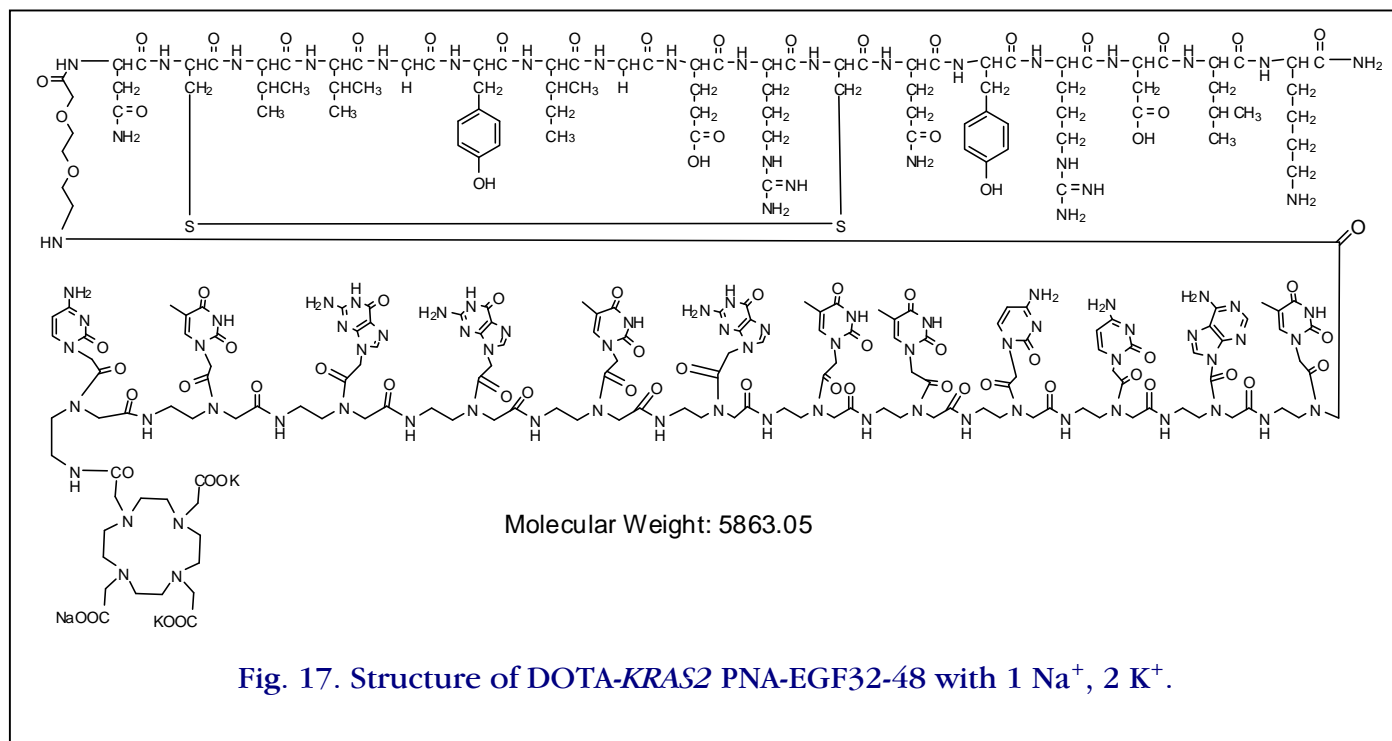
- AlexaFluor 532-GE11 (Fig. 13) was synthesized by solid phase coupling. HPLC and MS (Fig. 14) were satisfactory.



- Alexa Fluor 532-KRAS2 PNA-GE11 (Fig. 15) was synthesized by solid phase coupling. HPLC and MS (Fig. 16) were satisfactory.



- DOTA-KRAS2 PNA-EGF32-48 with cyclized peptide ring (Fig. 17) was synthesized by solid phase coupling. HPLC and MS (Fig. 18) were satisfactory.



Milestone 1.3.2. Validation of chelator-PNA gene probe with selected EGFR ligand by binding to cells expressing EGFR vs. control peptide (agreement with calculation, 5-fold greater). The purified DO3A-PNA-peptide will be labeled with ^{64}Cu , then used to measure the binding affinities of the [^{64}Cu]chelator-PNA-peptides to EGFR on human AsPC1 pancreas cancer cells that overexpress EGFR, plus blocking controls with full-length unlabeled EGF to test for EGFR specificity.

- We measured by confocal microscopy the uptake of AlexaFluor488-EGF, AlexaFluor488-EGF3248, and AlexaFluor647-EGF2031 by AsPC1 pancreas cancer cells that overexpress EGFR. Fluorescent agents were synthesized to enable visualization of intracellular localization. AsPC1 cells were seeded in 8-chamber slides (Lab-Tek, Nunc Inc.) and grew to 50% confluency. Cells in each chamber were washed once and incubated for 1 hr at 37°C in EGF-AlexaFluor488 (50 nM) or EGF3248-AlexaFluor488 (50 nM or 1 μM) in complete RPMI 1640 medium. At the end of incubation, cells were washed three times with PBS and fixed with 1% paraformaldehyde in PBS. Then, the chamber structures were removed and slides were covered with coverslips for imaging. Confocal images were taken on a Zeiss LSM 510 Meta confocal microscope with a 40x/1.3 oil DIC objective. At 50 nM, internalized EGF-AlexaFluor488 molecules were concentrated as puncta throughout the cytoplasm of AsPC1 cells, but not in the nucleus. The characteristic could be the result of concentrated molecules in vesicles (Fig. 19).

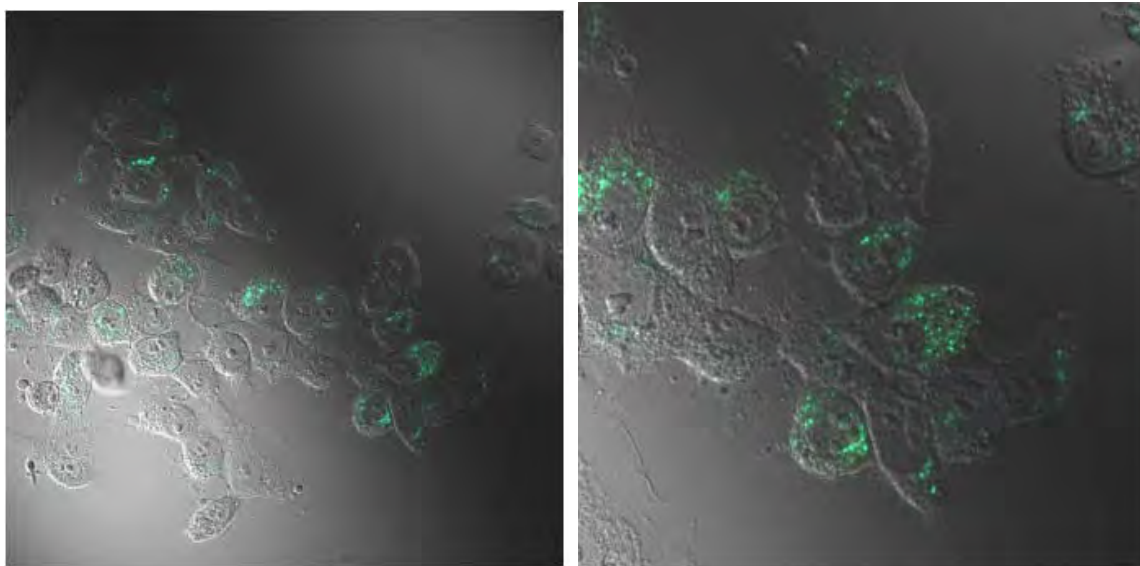
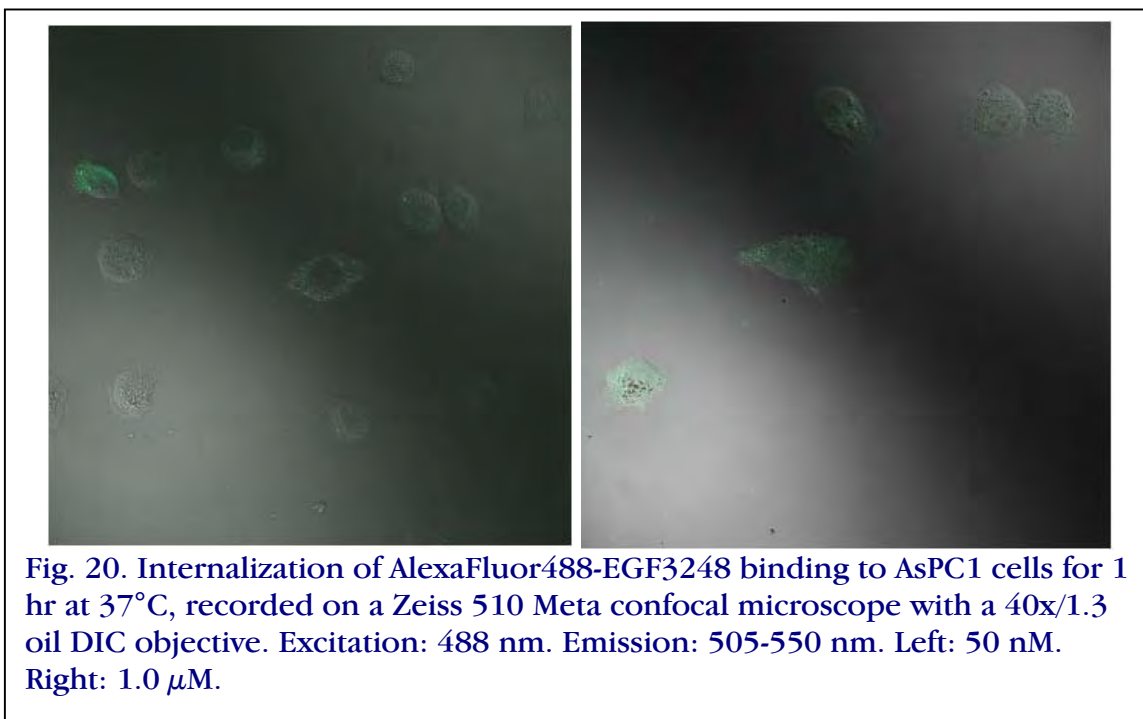
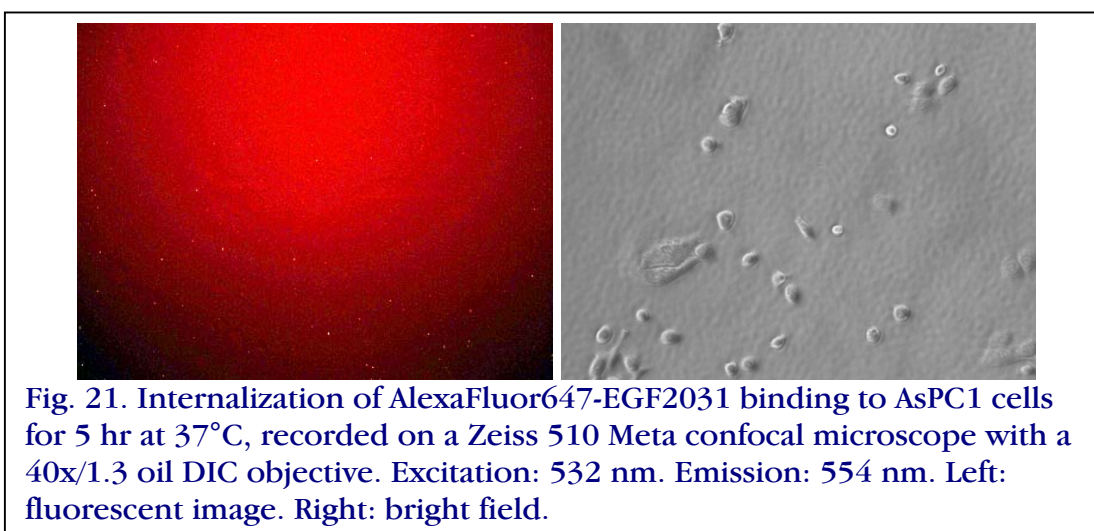


Fig. 19. Internalization of 50 nM AlexaFluor488-EGF binding to AsPC1 cells for 1 hr at 37°C, recorded on a Zeiss LSM 510 Meta confocal microscope with a 40x/1.3 Oil DIC objective. Excitation: 488 nm. Emission: 505-550 nm. Righthand image shows 2 \times zoom of center of left image.

- After one hr of incubation at 37°C, AlexaFluor488-EGF3248 showed moderate internalization (Fig. 20). With 50 nM AlexaFluor488-EGF3248, the fluorescent signals are distributed outside the nucleus. With 1 μ M AlexaFluor488-EGF3248, the fluorescent signals are distributed throughout the entire cell. This could be explained by different mechanisms of internalization. At low concentration of peptide, the internalization mechanism could be clathrin-mediated endocytosis. At high concentration of peptide, the internalization mechanism could also be pinocytosis.



- In contrast, even 1 μ M AlexaFluor647-EGF2031 showed no uptake by AsPC1 pancreas cancer cells after 1 hour at 37°C (Fig. 21). Furthermore, AlexaFluor532-GE11 was taken up equally well by AsPC1 cells, that overexpress EGFR, and by CHO cells, that do not make human EGFR (not shown), implying that GE11 uptake is nonspecific to EGFR.



- We measured by flow cytometry the uptake of AlexaFluor488-EGF (Fig. 22), AlexaFluor488-EGF20-31 (Fig. 23) and AlexaFluor488-EGF3248 (Fig. 23) by AsPC1 pancreas cancer cells that overexpress EGFR. Cells were seeded in 10-cm cell culture dishes and grew to 80% confluency. Cells were then incubated in complete medium containing 50 nM EGF-AlexaFluor488 or EGF3248-AlexaFluor488 at 4°C for 2 hr. After that, cells were washed three times with cold PBS, followed by incubation at 37°C for 30 min to allow internalization. Non-specific binding was measured by adding a 20-fold excess of EGF. After that, cells were collected by using a cell scraper and suspended in FACS buffer (2% fetal bovine serum and 0.01% sodium azide in PBS) before fixation

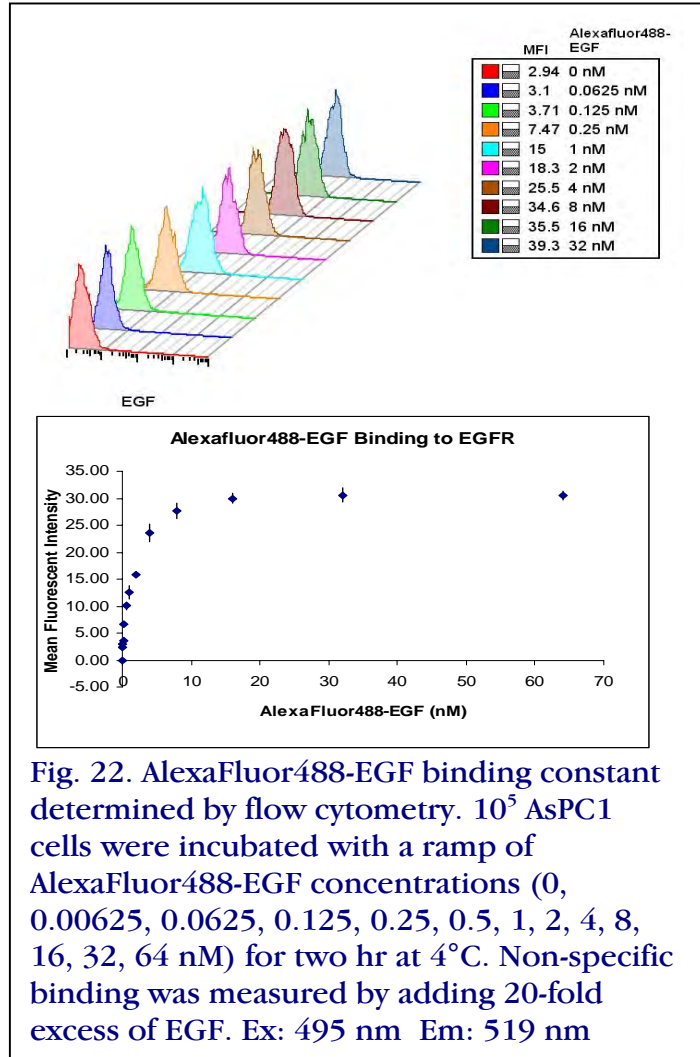


Fig. 22. AlexaFluor488-EGF binding constant determined by flow cytometry. 10^5 AsPC1 cells were incubated with a ramp of AlexaFluor488-EGF concentrations (0, 0.00625, 0.0625, 0.125, 0.25, 0.5, 1, 2, 4, 8, 16, 32, 64 nM) for two hr at 4°C. Non-specific binding was measured by adding 20-fold excess of EGF. Ex: 495 nm Em: 519 nm

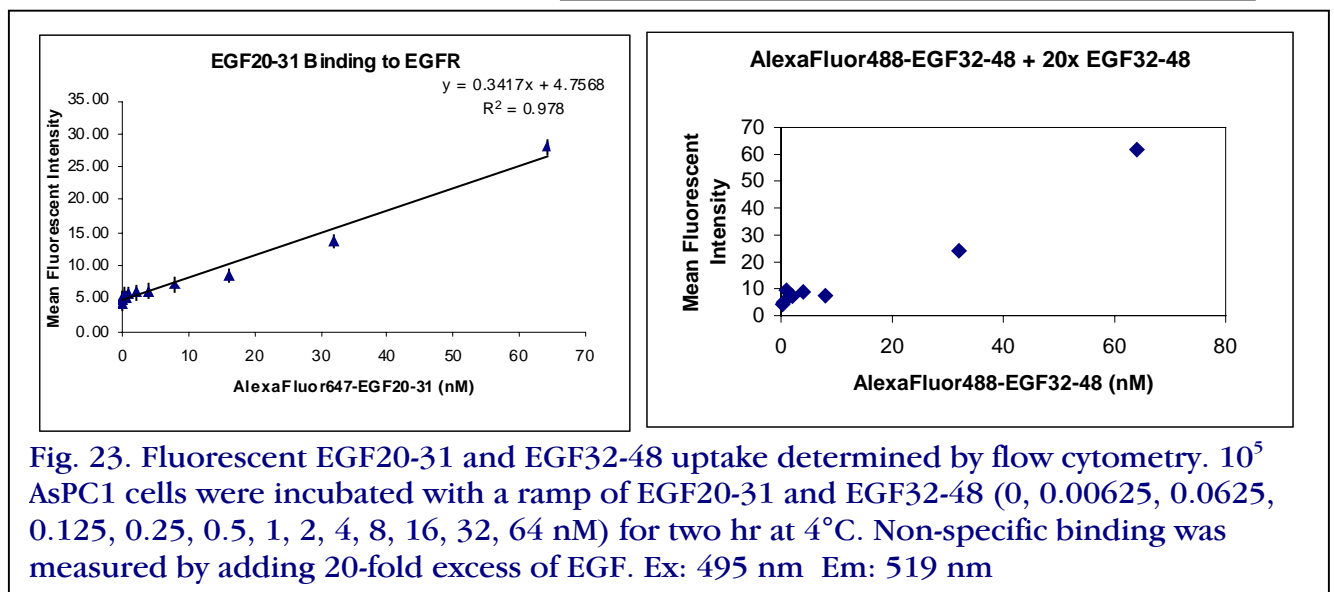


Fig. 23. Fluorescent EGF20-31 and EGF32-48 uptake determined by flow cytometry. 10^5 AsPC1 cells were incubated with a ramp of EGF20-31 and EGF32-48 (0, 0.00625, 0.0625, 0.125, 0.25, 0.5, 1, 2, 4, 8, 16, 32, 64 nM) for two hr at 4°C. Non-specific binding was measured by adding 20-fold excess of EGF. Ex: 495 nm Em: 519 nm

by adding an equal volume of 1% paraformaldehyde. Fluorescence emission due to internalized fluorophore-EGF/EGF3248 was determined by flow cytometry on a BD FACS Calibur. The starting fluorescence intensity of cells after fluorophore-EGF/EGF3248 binding but without excess unlabeled EGF was set to 100%. AlexaFluor488-EGF binding fit a hyperbolic curve with a K_D fit to 1.24 nM, but AlexaFluor488-EGF20-31 (Fig. 23) and AlexaFluor488-EGF3248 (Fig. 23) fit a linear, nonspecific binding plot.

- Uptake of [^{64}Cu]DOTA-KRAS2 PNA-EGF32-48 (WT5863) by AsPC1 cells showed nonspecific uptake (Fig. 24). 10^6 AsPC1 cells were incubated in DMEM growth medium with increasing concentrations of [^{64}Cu]DOTA-KRAS2 PNA-EGF32-48 at 37°C for 60 min. Cells were sedimented at 450×g for 5 min, and the supernatants were saved. Cells were washed twice with DMEM. The three supernatants were combined. Cell pellets were then lysed with 1 M NaOH. Cell pellet gamma counts yielded bound agent vs. free agent in supernatants.
- Both the fluorescence and radiouptake results imply that EGF32-48 induces insufficient internalization for effective imaging of *KRAS2* mRNA. This result agrees with the molecular dynamics insight [6], above, that EGFR activation requires a conformational shift that depends on all domains of EGF, not just one loop.

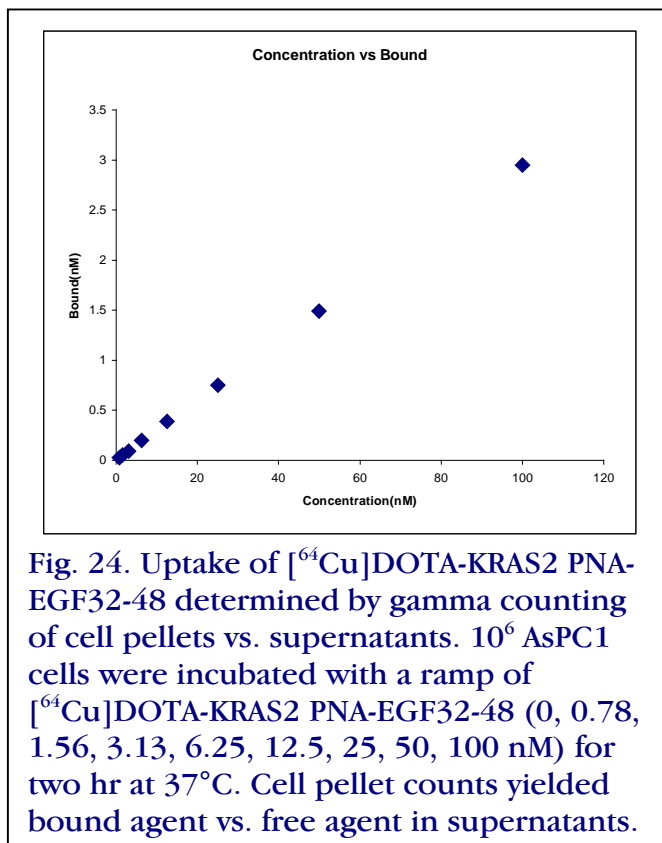


Fig. 24. Uptake of [^{64}Cu]DOTA-KRAS2 PNA-EGF32-48 determined by gamma counting of cell pellets vs. supernatants. 10^6 AsPC1 cells were incubated with a ramp of [^{64}Cu]DOTA-KRAS2 PNA-EGF32-48 (0, 0.78, 1.56, 3.13, 6.25, 12.5, 25, 50, 100 nM) for two hr at 37°C. Cell pellet counts yielded bound agent vs. free agent in supernatants.

Task 2.1. Acquisition of haptic hardware and software (Leads: Wickstrom/Thakur)

Milestone 2.1.1. Acquisition and installation of computer plus Amira 5 simulation and Phantom software packages. Quotes will be obtained, permission from TATRC will be requested, purchase orders will be issued, computer hardware and software will be received, installed, and put into operation.

- Omni Manipulators and Phantom software acquired and installed on existing Dell Inspiron 531 “Sammelweis”.
- The volumetric-haptic 3DBoxx 8570 computer system “Kollman” was delivered from Boxx Technologies on 12 Feb 2010. Through negotiations, we spent about half as much as originally budgeted for the 3D haptic system.

- Amira 5 was purchased from Visage Imaging, San Diego, and installed on Kollman.
- SOFA was downloaded from the supporting CNRS lab in Lyon, France, and installed on Kollman.

Task 2.2. Acquisition of pancreatic cancer FDG PET/CT data (Leads: Thakur/Kairys)

Milestone 2.2.1. Amira 5 integration and conditioning of pancreatic cancer FDG PET/CT data to a resolution of 5 mm. PET imaging scans of FDG accumulation in suspect human pancreatic cancers plus anatomical CT images will be registered to a common coordinate system, appropriately scaled and aligned to account for differences in acquisition and patient conditions (e.g., movements, positioning, etc.), and stored in a common (lossless) format for subsequent visual and haptic display.



Fig. 25. 3D projection of thorax of patient A on the 3D Boxx 8570 at TJU. Advanced pancreatic tumor (yellow) extends from the head of the pancreas (green). The liver (burgundy), aorta (orange), and kidneys (blue) are also emphasized.

- CT data and PET data were obtained with IRB and HRPO approval for one deceased TJU pancreatic cancer patient, de-identified as Patient A.
- CT data at 1 mm resolution were rendered into a 3D image using Slicer 3, prior to acquisition of Amira 5 (Fig. 25).
- PET and CT data at 5 mm resolution were rendered into a 3D image using 3DSlicer 3 (Fig. 26).

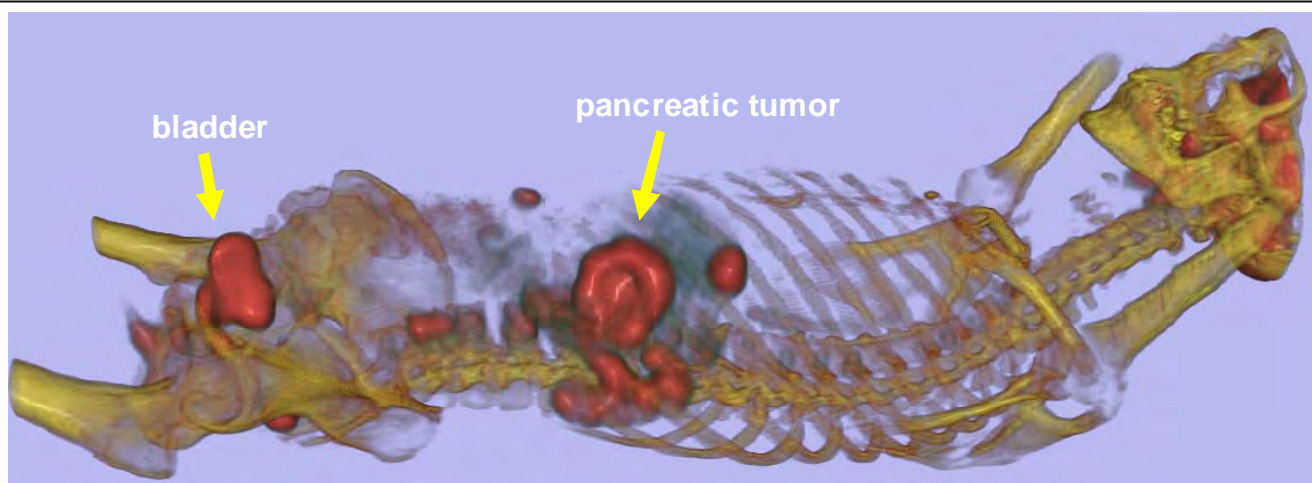


Fig. 26. 3D projection of fused PET/CT data at 5 mm resolution of patient A on the 3D Boxx 8570 at TJU. CT images are shown in bone, with organs in gray, while PET images are emphasized in red.

Milestone 2.2.2. Common multilayer visualization of pancreatic cancer FDG PET/CT data in layers to a thickness of 5 mm. Once the data are properly conditioned, common multilayer visualization will be applied. Thus individual modalities are to be presented as overlays with user preferred transparency. Joint visual-haptic techniques will be developed to modulate individual modality displays with images, slabs, or surfaces of the CT data while simultaneously feeling the appropriately aligned FDG PET imagery.

- Visualizations of the Patient A thorax were carried out with Amira 5. Version 1.2 was based on one non-contrast CT at 1 mm resolution and one PET image at 5 mm resolution co-registered with the non-contrast CT. The surgeons were shown how to manipulate the image, especially how to strip off overlaying tissues and organs overlaying the pancreas. Snapshots from version 1.2 are shown in Figs. 27 and 28. The PET image of the malignant region of the pancreas appears in Fig. 29

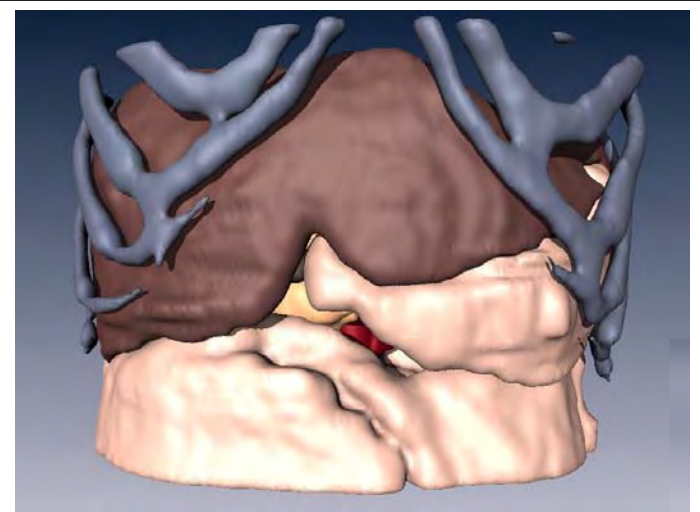


Fig. 27. Volumetric rendering of Patient A in version 1.2. Structures displayed in this rendering include the skeleton (gray), liver (brown), intestines (flesh), stomach (flesh), pancreas (gold), and aorta (red).

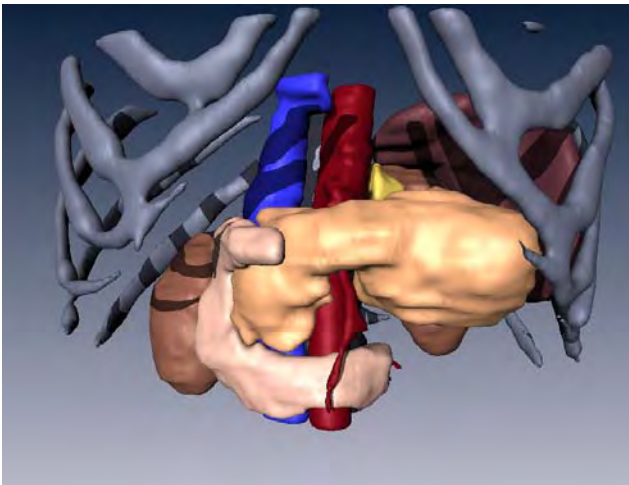


Fig. 28. Version 1.2 with some organs stripped away to more fully display the pancreatic tumor (black arrow). Organs displayed in this rendering include the skeleton (gray), kidneys (brown), duodenum (flesh), spleen (plum), adrenal gland (yellow), aorta (red), vena cava (blue), superior mesenteric artery (dark red), and pancreas (gold).

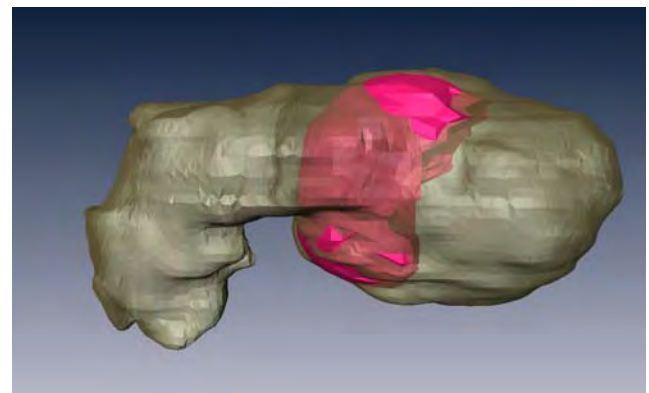


Fig. 29. 3D PET/CT rendering of pancreas (gold) and advanced pancreatic tumor (gold) of patient A. FDG-accumulating zone (pink) reveals aggressive, malignant cells.

- Version 1.3 included a more complete vascular network due to the inclusion of a contrast-enhanced CT at 1 mm resolution and one PET image at 5 mm resolution. Snapshots from version 1.3 appear in Figures 30, 31, and 32. Discussions with the evaluating surgeons (see Task 2.4 below) brought forth the idea of coloring the veins more in line with their perceived oxygenation levels. Tilting the image forward revealed the organs behind the pancreas (Fig. 32). To the right is the spleen (plum). Under the spleen is the left kidney (brown). At the top middle is the left adrenal gland (yellow). In this patient, the splenic vein was thrombosed, leading to the enlarging of accessory veins (purple) leaving the spleen.

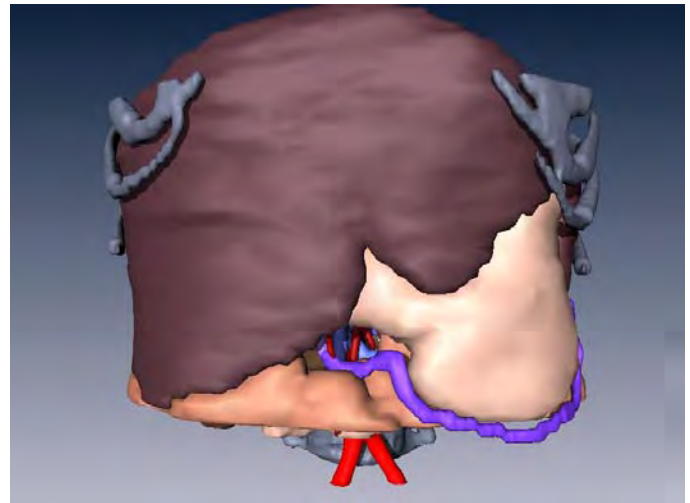


Fig. 30. Volumetric rendering of Patient A in version 1.3. Structures displayed in this rendering include the skeleton (gray), liver (brown), intestines (coral), stomach (flesh), right gastroepiploic vein (purple), and common iliac artery (red).

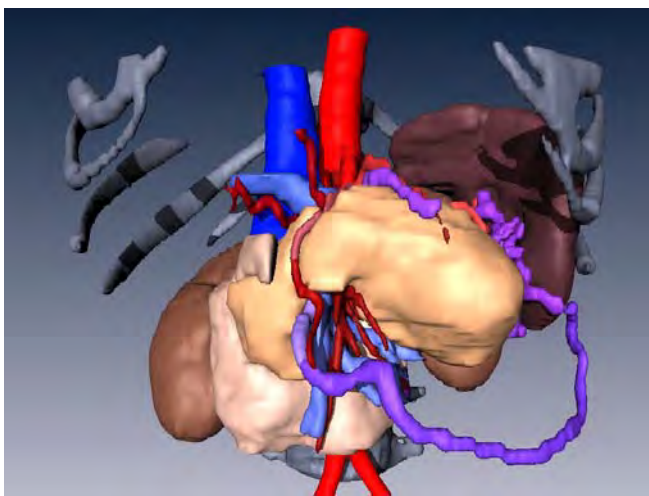


Fig. 31. Volumetric rendering of Patient A in version 1.3. Structures displayed in this rendering include the skeleton (gray), kidney (brown), pancreas (gold), aorta (red), accessory arteries (red-orange) vena cava (blue), right gastrepiploic and splenic veins (purple).

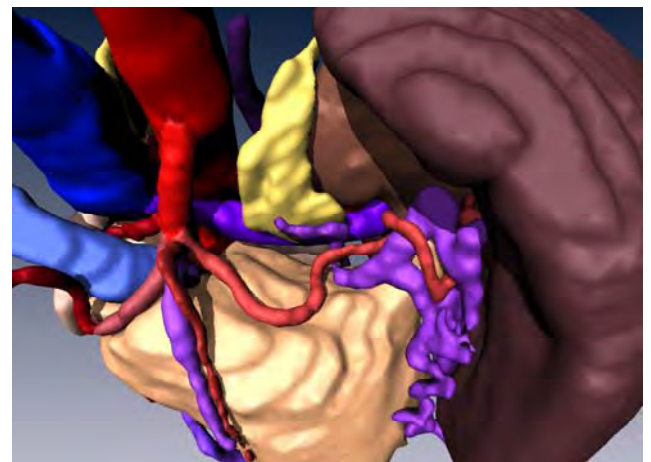


Fig. 32. Volumetric rendering of Patient A in version 1.3, tilted forward: pancreas (gold), adrenal gland (yellow), kidney (brown), spleen (plum), aorta (red), accessory arteries (red-orange) vena cava (blue), right gastrepiploic and splenic veins (purple).

Task 2.3. 3D viewing and haptic manipulation of pancreatic cancer PET/CT images (Leads: Barner/Steiner)

Milestone 2.3.1. Point-based 3D animations of merged pancreatic cancer FDG PET/CT data. Simulations of deformable objects will be carried out with theoretically justified physics-based approaches, including mesh and mesh-free methods. In particular, the mesh-based mass spring and finite element method (FEM) will be applied to create haptic responses to tissues seen in images. The combination of mesh-free physics with point-sampled surfaces, yielding the so-called point-based animations (PBA) technique, will be applied to animate merged imaging data. PBA is a mesh-free continuum mechanics-based framework for the animation of elastic, plastic and melting objects, utilizing point-based volume and surface representations derived from continuum mechanics, which allows the specification of common material properties such as Young's Modulus and Poisson's Ratio.

- UD colleagues Rui Hu, Karl Steiner, and Kenneth Barner developed and implemented a physical based deformation module using the point-based animation algorithm. On the issue of simulating deformable objects, the physical-based finite element method (FEM) and the mass-spring method have garnered great attention. However, these deformation algorithms share some common issues: 1) A fine mesh that connects nodes is required for both FEM and mass-spring model simulation. This leads to an issue that the mesh must be constantly updated and maintained when model topology changes. During simulation, arbitrary element decomposition such as cutting, may lead to ill-shaped elements, which will reduce the stability for deformation. 2) For the mass-spring model, one has to fine-tune the spring parameters so that the model can deform in a way that a specific soft tissue behaves; however, fine-tuning for arbitrarily shaped models is rather difficult. To avoid these issues, various meshless methods have emerged. They do not require subdividing the object domain into subelements. This bypasses the cumbersome meshing process. The deformation model is only comprised of mass nodes, which are generated by sampling the object volume before simulation. Also, as this approach follows the continuum mechanics approach, the user can easily choose the corresponding Poisson ratio and Young's Modulus to control the behavior of an object. Among meshless simulation approaches, the point based animation (PBA) has been widely adopted in the computer graphics community. The UD team successfully implemented the PBA simulation algorithm. The PBA algorithm can be broken into five steps: 1) Initialization; 2) Using moving least squares approximation to estimate the derivative of the

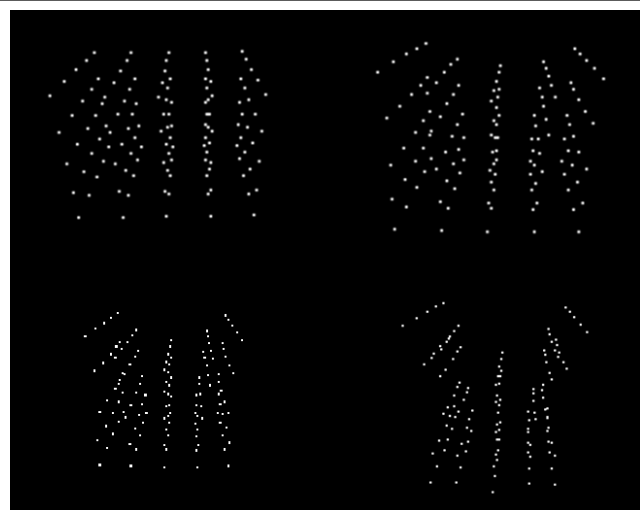


Fig. 33. The deformation of a cube sampled by points under gravity. Upper left and right rows are fixed.

displacement field; 3) Updating strains and stresses; 4) Computing forces; 5) Time integration. The PBA algorithm works on a group of points. The deformation of the model is controlled by the movement of these points. Fig. 33 shows the deformation screenshots when a cube is influenced by gravity. The cube is sampled as a number of points. Two rows of these points (top left and right) are fixed in space, while the other points are dragged down by gravity.

- The UD team used PBA to update surface mesh. The point movement in PBA simulation is used to model the physical behavior of a model when influenced by external forces. To map the point movement to the movement of surface vertices, such that the model can be visualized easily, we use another module to map the displacement field of points to the counterpart of the surface mesh vertices. Each vertex has a group of neighboring points specified during initialization. Different points have different weighting values on the vertex, based on their distance to the vertex. The displacement value on each point is weighted using this predefined weighting value and then sent to the vertex. This updated surface mesh is used for visual feedback. Fig. 34 exhibits the deformation of a tumor model falling on a hard surface. The UD team compared the behavior of tumor with two different Young's modulus parameters. The upper row is relatively stiff, while the lower row is very soft.

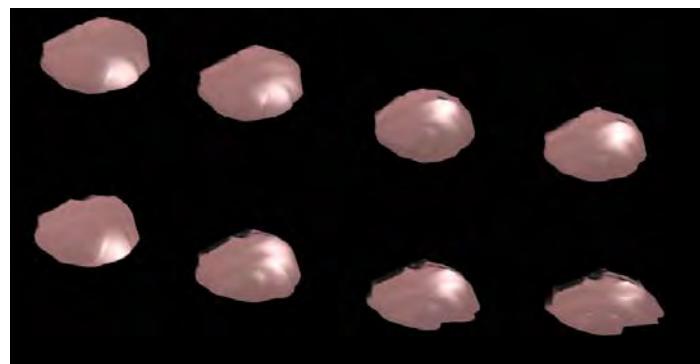


Fig. 34. The deformation of a soft tumor when falling onto a virtual hard surface. Top row – stiff material, bottom row – soft material.

- The UD team simulated deformable bodies. The image-based collision detection and contact force response algorithm follows five phases: 1) broad collision detection; 2) preparation of viewport setup; 3) layered depth image (LDI) generation; 4) calculation of the penetration volume and its gradient; and 5) transition of the computed penalty force to the deformation module. In the broad collision detection phase, the axis-aligned bounding box (AABB) of each object is

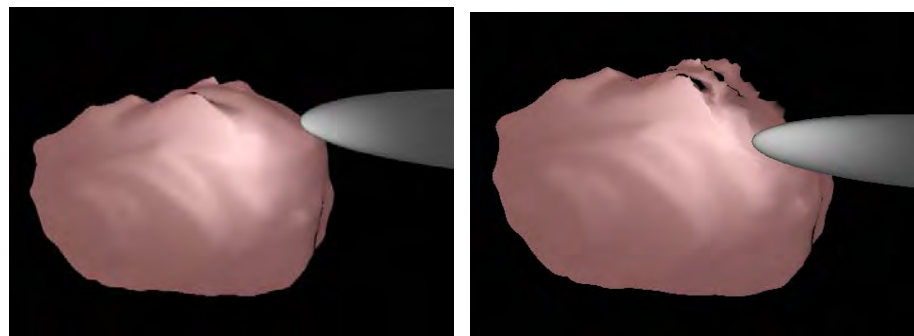


Fig. 35. Virtual palpation of a tumor model using a rod-shaped instrument.

updated. If there is an intersection of two AABBs, a fine collision detection and response scheme is conducted by analyzing the sampled LDI of the intersecting objects. Since LDI contains the volume overlapping information, the interaction force at surface vertices can be easily calculated. In Fig. 35, the simulation scene is illustrated with a tumor model. The development of this approach fulfills the animation section in Milestone 2.3.1 for CT data, but not for combined PET/CT data.

Milestone 2.3.2. SOFA-based imaging simulation of merged pancreatic cancer FDG PET/CT data with Phantom haptic feedback. End user visualization will be developed with the SOFA open-source real-time simulation framework as an environment for medical simulations. End user haptic feedback will be developed with the PHANTOM, which is accurate for fine detail work, widely used by many research groups, and runs on a variety of computing platforms.

- SOFA-based imaging simulation with haptic feedback manipulation of pancreatic cancer CT data from TJU patient A is underway. The visual models in Amira have been converted into surface meshes and imported in a SOFA simulation scene (Fig. 36). The images in SOFA are currently visual only as more work is being done to generate meshes for collision models and force field models. The image of patient A in SOFA with the skin and muscle removed also shows the liver partly transparent (Fig. 37). The models being transferred from Amira to SOFA have a high polygon count at the moment. Reducing the polygons is not difficult but more delicate structures in the object will be lost. Since the point based animation and finite element method are dependent on how many points are used to represent each object, due consideration will need to be made when deciding on an acceptable polygon count for the collision and forcefield models. Further work will need to be done to



Fig. 36. 3D projection in SOFA of thorax of patient A, showing surface skin and muscle beneath.

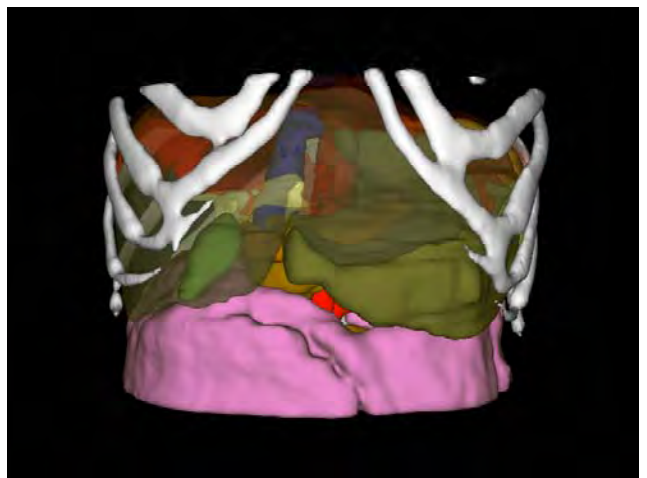


Fig. 37. 3D projection in SOFA of internal anatomy of patient A, showing ribs and organs. The liver is partially transparent: bones (white), liver (translucent gray), intestines (pink), pancreas (gold), duodenum (lavender), aorta (red), stomach (olive), diaphragm (rust).

decide on an acceptable number of polygons to improve performance accurately represents the organs.

- A new method for haptic interaction using the Linear Compliance Problem (LCP) is being tested. This new method has alleviated the tendency for the haptic object to become stuck to the model, in part by allowing the collision response to be separately calculated from the physical deformations. Also LCP allows different regions of the object to behave differently upon contact. Fig. 38A shows the pancreas (gold) before interacting with the haptic probe (grey). Fig. 38B shows the haptic probe interacting with a region of the pancreas designated to be soft and easily deformed, such as interacting with a necrotic region of a tumor. In Fig. 38C, the haptic object is interacting with a stiff area, simulating the stiff regions of a tumor mass. Finally, Fig. 38D shows the haptic object interacting with a firm yet pliable region that could be representative of the normal pancreatic tissue. The values used for contact must be tuned by hand, requiring surgeon feedback on how stiff or soft certain organs feel. Work is ongoing to incorporate other deformable objects in close proximity to each other. These steps achieve part of Milestone 2.3.2 for CT data, but not for combined PET/CT data.

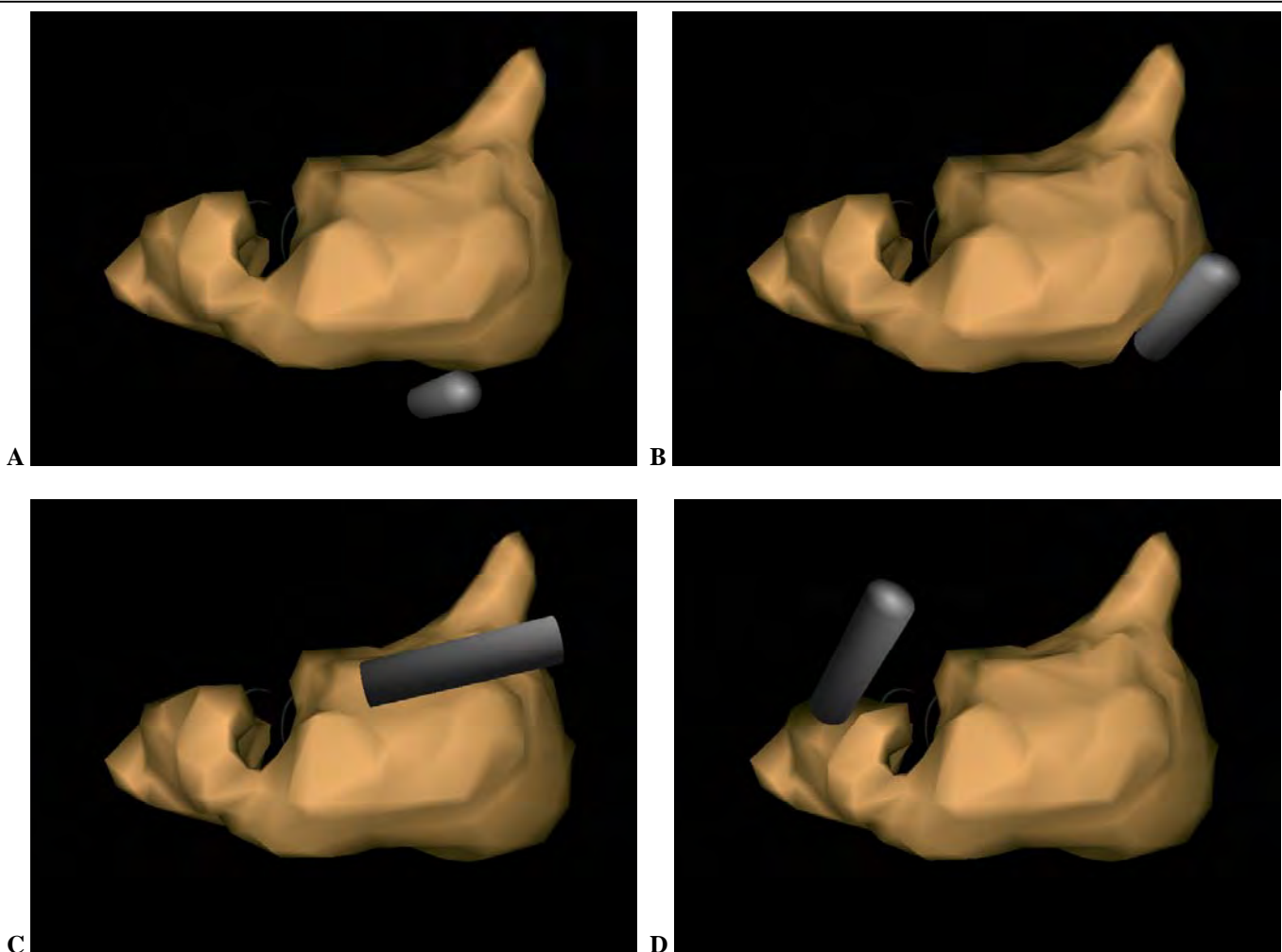


Fig. 38. 3D projection in SOFA of patient A pancreas (gold), with a haptic probe (grey). A: pancreas before interacting with the haptic probe. B: probe interacting with soft, necrotic region. C: probe interacting with stiff active tumor. D: probe interacting with normal remaining pancreas.

Task 2.4. Human perceptual evaluation by experienced surgeons (Lead: Kairys)

Milestone 2.4.1. Evaluation by 6 experienced surgeons of 3D animations of merged pancreatic cancer FDG PET/CT data: assessment \pm PET images (enhanced spatial understanding). Experienced TJU surgeons (n=6) will qualitatively evaluate the 3D interface for ease of use and ability to intuitively manipulate and adjust the image. Users will qualitatively assess whether the addition of the 3D CT reconstruction and merged FDG/PET data enhances their spatial understanding of tumor location, enhances their understanding of the extent of pathology, and whether this display enhances their ability to plan a surgical resection for lesions of different sizes and locations as compared to traditional CT images alone.

- TJU IRB and HRPO approved the evaluation questionnaire for 3D animations. The questionnaire follows.

3-D Volumetric Imaging - Evaluation by Surgeons

Case Identifier

Image Evaluated: (A,B,C,D...) _____

Version: (1,2,3...) _____

Legend

1 = strongly disagree
 2 = disagree
 3 = neither agree/disagree
 4 = agree
 5 = strongly agree

(circle one)

Visual Effects

- | | | | | | |
|---|---|---|---|---|---|
| 1. The display hardware is easy/comfortable to use. | 1 | 2 | 3 | 4 | 5 |
| 2. I found it easy to manipulate/re-position the image. | 1 | 2 | 3 | 4 | 5 |
| 3. The organs/structures are accurately represented (accuracy of segmentation). | 1 | 2 | 3 | 4 | 5 |
| 4. Colors/textures are appropriate (accuracy of rendering). | 1 | 2 | 3 | 4 | 5 |
| 5. I am satisfied with the level of detail that is presented. | 1 | 2 | 3 | 4 | 5 |
| 6. The model provides me with adequate reference to surrounding structures. | 1 | 2 | 3 | 4 | 5 |

- | | | | | | |
|--|---|---|---|---|---|
| 7. The overall 3-dimensional image appears realistic (matches what I expect to see in the OR). | 1 | 2 | 3 | 4 | 5 |
|--|---|---|---|---|---|

Usefulness

- | | | | | | |
|---|---|---|---|---|---|
| 8. By simply viewing the image(s) in the 3-D model, I get a better understanding of the tumor and its relationship to the surrounding organs. | 1 | 2 | 3 | 4 | 5 |
| 9. By simply viewing the image(s) in the 3-D model, my plan for how to approach this tumor changed. (as compared to traditional CT images). | 1 | 2 | 3 | 4 | 5 |
| 10. By overlaying the PET data in the 3-D model, I get a better understanding of the tumor and its relationship to the surrounding organs. | 1 | 2 | 3 | 4 | 5 |
| 11. By overlaying the PET data in the 3-D model, my plan for how to approach to this tumor changed (as compared to traditional CT images). | 1 | 2 | 3 | 4 | 5 |

How could the visual appearance of this model be improved?

Applicability

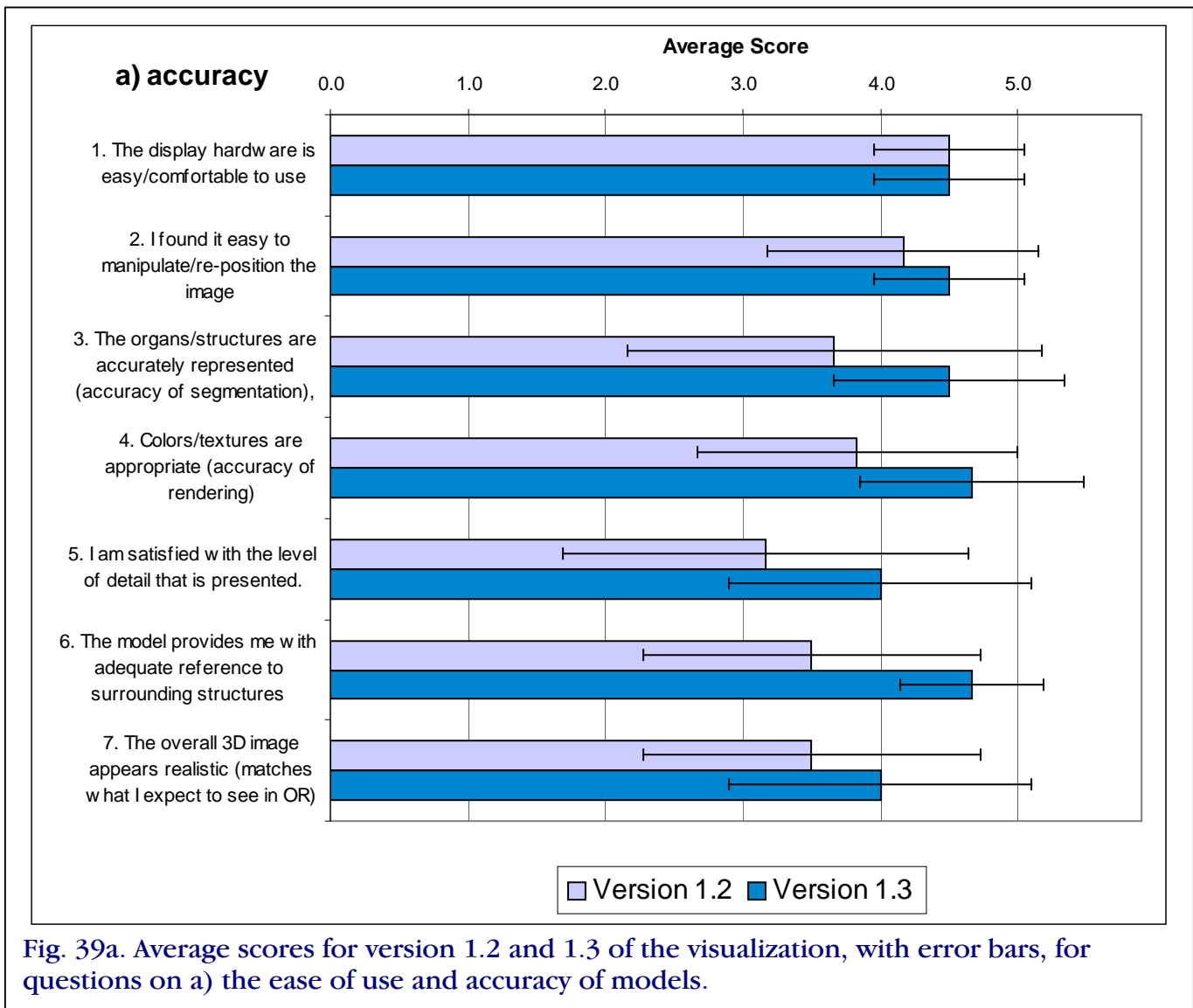
- | | | | | | |
|--|---|---|---|---|---|
| 12. I would want to use this 3-D image to plan an operation for a patient with this specific tumor. | 1 | 2 | 3 | 4 | 5 |
| 13. I would want to use this 3-D image with PET overlay to plan an operation for a patient with this specific tumor. | 1 | 2 | 3 | 4 | 5 |
| 14. I would like to have this system available to me in the OR, for reference during an actual operation. | 1 | 2 | 3 | 4 | 5 |
| 15. I believe that this system would help residents/assistants better prepare for the operation. | 1 | 2 | 3 | 4 | 5 |

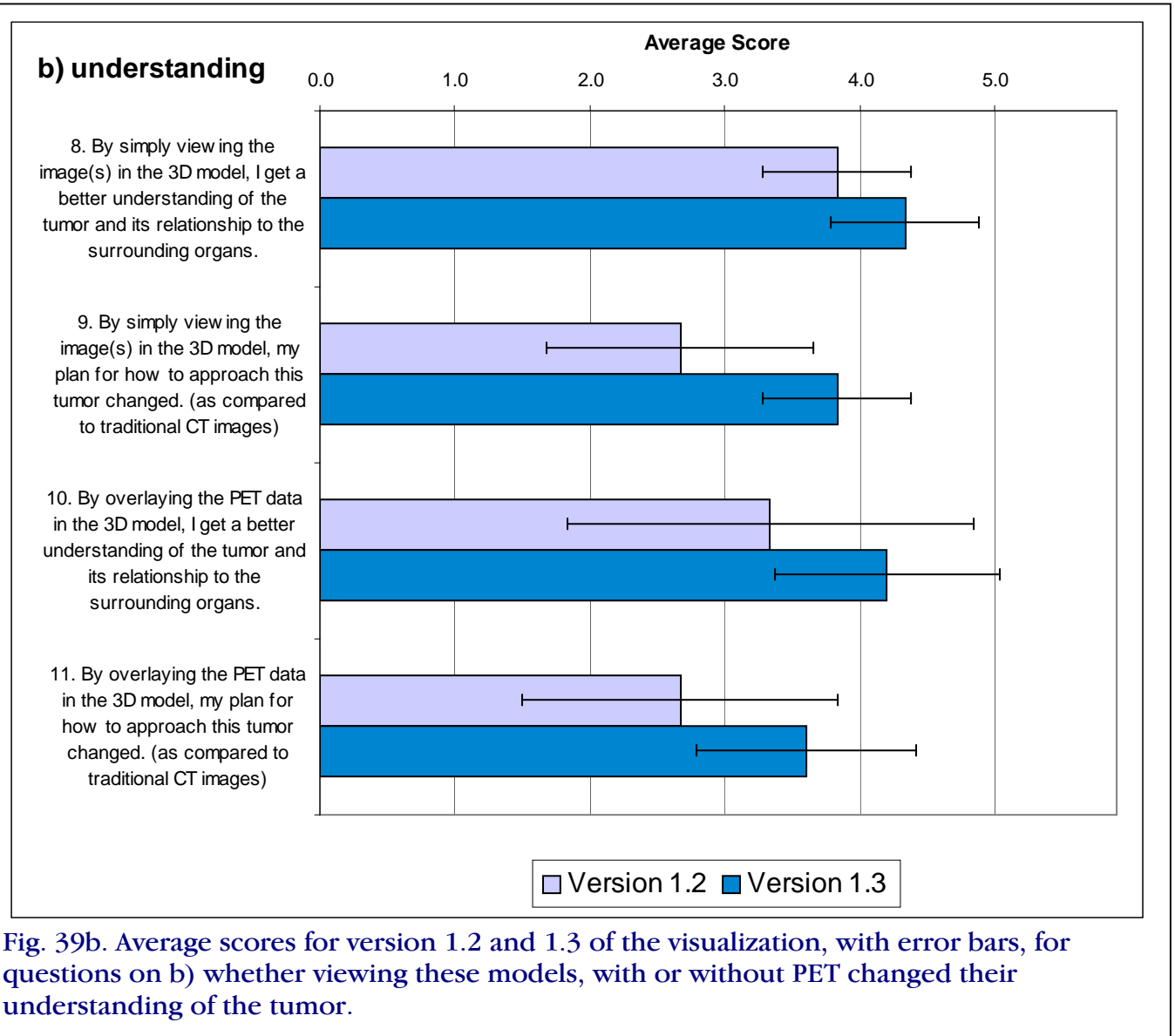
How could the usefulness of this model be improved?

☐ Other comments

Reviewer use only:

- Six surgeons from Thomas Jefferson University Hospital volunteered to evaluate version 1.2, with standard CT, and 1.3, with contrast-enhanced CT, of the Patient A thoracic visualization. These surgeons varied from general surgery to thoracic surgery. The surgeons were shown how to manipulate the image, especially how to strip off overlaying tissues and organs overlaying the pancreas. The average scores for each of the 15 questions asked for versions 1.2 and 1.3 are shown in Fig. 39abc. Averaging surgeon responses to each of the 15 questions, version 1.2 scored 3.6 ± 1.3 , while version 1.3 received a score of 4.4 ± 0.8 . The overall averages of the questionnaire illustrate greater appreciation of version 1.3, while the standard deviations reveal greater consensus in evaluating version 1.3. The set of scores for 1.3 were significantly higher than for 1.2, according to a paired t-test.





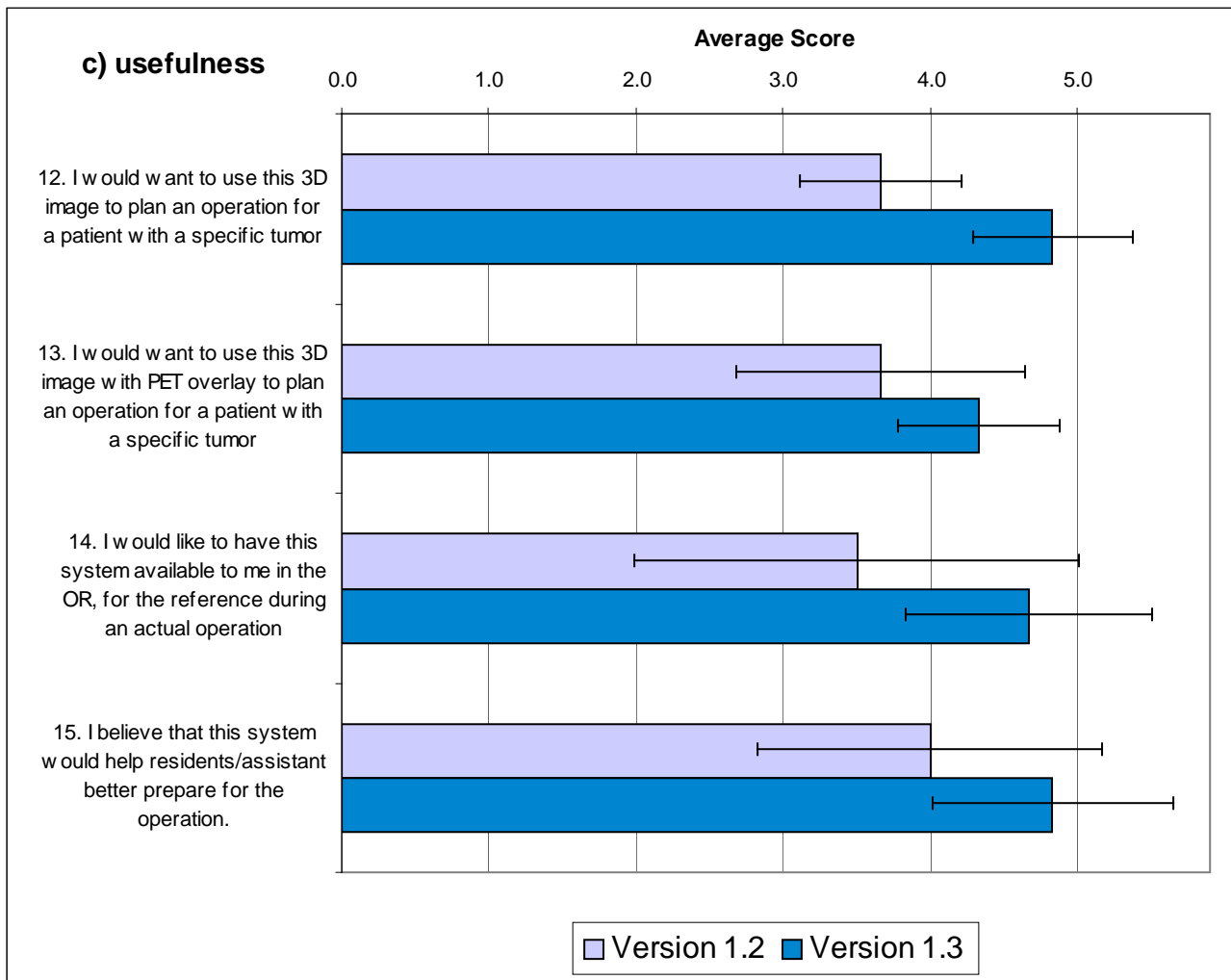


Fig. 39c. Average scores for version 1.2 and 1.3 of the visualization, with error bars, for questions on c) the usefulness of the 3D system.

Milestone 2.4.2. Evaluation by 6 experienced surgeons of haptic manipulation of merged pancreatic cancer FDG PET/CT data: assessment \pm PET images (enhanced spatial understanding). Experienced TJU surgeons (n=6) will utilize the haptic interface to “palpate” the pancreas and region of the tumor. A qualitative assessment will be performed to determine the realism of the experience, and to determine optimal assignment and adjustment of the reconstructed tissue’s Young’s Modulus and Poisson’s Ratio to best represent the conditions experienced during actual surgery. The benefit of overlaying the FDG PET data, allowing refinement of the haptic experience by further adjustment of the reconstructed tissues’ properties, will also be assessed. The addition of enhanced visual feedback (such as partial transparency) or enhanced haptic feedback (such as a vibratory sensation when palpating over areas of increased FDG PET activity) will be assessed to determine if these techniques subjectively improve the surgeons’

perception of the location and extent of disease. These techniques will be evaluated for lesions of different sizes and locations, including small lesions that may otherwise not be easily palpable in real life situations.

- TJU IRB and HRPO approved the evaluation questionnaire for 3D animations including haptic manipulation. The questionnaire follows.

3-D Haptic Imaging - Evaluation by Surgeons

Case Identifier

Image Evaluated: (A,B,C,D...) _____

Version: (1,2,3...) _____

Legend

1 = strongly disagree
2 = disagree
3 = neither
agree/disagree
4 = agree
5 = strongly agree

(circle one)

Haptic ("Touch and Feel") Effects

- | | | | | | |
|--|---|---|---|---|---|
| 1. The haptic interface devices are easy to use. | 1 | 2 | 3 | 4 | 5 |
| 2. The haptic interface devices provide an adequate range of movement. | 1 | 2 | 3 | 4 | 5 |
| 3. I am satisfied with how I interact with the model. | 1 | 2 | 3 | 4 | 5 |
| 4. When manipulating/touching the model, the displacement of the normal structures is realistic. | 1 | 2 | 3 | 4 | 5 |
| 5. When manipulating/touching the model, the displacement of the tumor is realistic. | 1 | 2 | 3 | 4 | 5 |
| 6. When manipulating/touching the model, the texture of the normal structures is realistic. | 1 | 2 | 3 | 4 | 5 |
| 7. When manipulating/touching the model, the texture of the tumor is realistic. | 1 | 2 | 3 | 4 | 5 |
| 8. When manipulating/touching the model, the relative movement of the organs is realistic. | 1 | 2 | 3 | 4 | 5 |

- | | | | | | |
|--|---|---|---|---|---|
| 9. When manipulating/touching the model, the vibration felt over the tumor gave me a better understanding of malignant tissue vs. clear margins. | 1 | 2 | 3 | 4 | 5 |
|--|---|---|---|---|---|

Usefulness

- | | | | | | |
|--|---|---|---|---|---|
| 10. By touching and feeling the model, I get a better understanding of the tumor and its relationship to the surrounding organs. | 1 | 2 | 3 | 4 | 5 |
| 11. By touching and feeling the model, I can do a better job planning my approach to this tumor. | 1 | 2 | 3 | 4 | 5 |
| 12. By overlaying the PET data and haptically interacting with the model, I get a better understanding of the tumor and its relationship to the surrounding organs. | 1 | 2 | 3 | 4 | 5 |
| 13. By overlaying the PET data and haptically interacting with the model, my plan for how to approach to this tumor changed. (as compared to traditional CT images). | 1 | 2 | 3 | 4 | 5 |

How could the touch and feel of this model be improved?

Applicability

- | | | | | | |
|---|---|---|---|---|---|
| 14. I would want to use this 3-D image to plan an operation for a patient with this specific tumor. | 1 | 2 | 3 | 4 | 5 |
| 15. I would want to use this 3-D image with PET overlay to plan an operation for a patient with this specific tumor. | 1 | 2 | 3 | 4 | 5 |
| 16. I would want to use this 3-D image with PET overlay and haptic interaction to plan an operation for a patient with this specific tumor. | 1 | 2 | 3 | 4 | 5 |
| 17. I would like to have this system available to me in the OR, for reference during an actual operation. | 1 | 2 | 3 | 4 | 5 |

18. I believe that this system would help residents/assistants better prepare for the operation. 1 2 3 4 5

☐ How could the usefulness of this model be improved?

☐ Other comments

Reviewer use only:

- The questionnaire will be administered after the haptic model satisfies the investigators as a realistic presentation.

C. KEY RESEARCH ACCOMPLISHMENTS

- Molecular dynamics calculations implied that EGF binding to the extracellular domain of EGFR (sEGFR) disrupts auto-inhibitory intramolecular interactions by increasing the distance between the so-called “dimerization arm” and domain IV.
- Molecular dynamics calculations implied that EGFR dimerization is more favorable for one EGF/EGFR complex plus one empty EGFR. Such asymmetrical dynamics in EGFR provide a structural rationale for the observed negative cooperative effects in EGFR activation.
- Molecular dynamics calculations implied that single loop EGF fragments would be insufficient to activate EGFR or initiate internalization.
- Direct measurements of cellular uptake of two different EGF fragments, EGF20-31 and EGF32-48, as well as *KRAS* PNA-EGF32-48, agreed with the computer predictions of nonspecific uptake.
- 3D visualization of the thorax of a patient with pancreatic cancer was evaluated as useful to surgeons and applicable in the clinic.

D. REPORTABLE OUTCOMES

1. Wickstrom, E., Chen, C.-P., Devadhas, D., Wampole, M., Jin, Y.-Y., Sanders, J. M., Kairys, J. C., Ankeny, M. L., Hu, R., Barner, K. E., Steiner, K. V., and Thakur, M. L. (2011) Three dimensional projection environment for molecular design and surgical simulation. *Studies in Health Technologies and Informatics* **163**:691-695.
2. Hu, R., Barner, K. E., and Steiner, K. V. (2011) A generalized haptic feedback approach for arbitrarily shaped objects. *Studies in Health Technologies and Informatics* **163**:224-30.
3. Chen, C.-P., Sethi, D., Jin, Y.-Y., and Wickstrom, E. (2011) EGFR-targeting peptide as ligand to direct peptide nucleic acid (PNA) for imaging oncogene mutations. 22nd American Peptide Symposium, San Diego, California, June 25-30.
4. Sanders, J. M., and Wickstrom, E. (2011) Ligand-dependent activation and the structural basis of negative cooperativity in EGFR: a molecular dynamics study. Protein Society 25th Anniversary Symposium, Boston, Massachusetts, July 23-27.
5. Sanders, J. M., Wampole, M.E., Thakur, M. L., and Wickstrom, E. (2011) Molecular dynamics study of EGFR ligand-dependent activation and asymmetric dimerization, submitted for publication.
6. Wampole, M.E., Kairys, J. C., Ankeny, M. L., Thakur, M. L., and Wickstrom, E. (2011) Surgeon evaluations of three-dimensional renderings of PET/CT scans of the thorax of a patient with a ductal pancreatic mass, manuscript in preparation.

E. CONCLUSIONS

The epidermal growth factor receptor (EGFR) is a member of the ErbB receptor tyrosine kinase (RTK) family that plays a pivotal role in cell proliferation, differentiation and migration. Aim 1 explored the possibility that EGFR might serve as a gateway into cells for mRNA imaging agents. While x-ray structures have provided insight into EGFR function, the conformational pathway(s) of ligand-dependent activation are not well understood. Using molecular dynamics (MD) techniques we found that EGF binding to the extracellular domain of EGFR (sEGFR) disrupts auto-inhibitory intramolecular interactions by increasing the distance between the so-called “dimerization arm” and domain IV. To investigate early ligand binding effects on sEGFR dimers, we constructed a singly ligated sEGFR dimer for simulation. MD simulations of the singly ligated sEGFR dimer exhibited asymmetrical motion in each monomer and a decrease in the size of the second EGF binding pocket by 10 Å. Free energy calculations indicated that asymmetrical dimerization with only one EGF-sEGFR monomer is more energetically favorable than dimerization of two ligated sEGFR monomers by 2.88 kcal•mol⁻¹. To see if asymmetrical motion can be extended to ErbB heterodimers, we simulated a model sEGFR-ErbB2 dimer. This heterodimer also exhibited asymmetrical motion. These results suggest that asymmetrical dynamics in sEGFR and other ErbB family members play an essential role in receptor activation and cooperativity. From this study, we inadvertently realized a new potential target for therapeutic inhibition of EGFR activation.

On the other hand, MD calculations implied that single loop EGF fragments would be insufficient to activate EGFR or initiate internalization. Direct measurements of cellular uptake of two different EGF fragments, EGF20-31 and EGF32-48, as well as *KRAS* PNA-EGF32-48, agreed with the computer predictions of nonspecific uptake. Hence, EGFR constitutes an unlikely candidate to serve as a gateway into cells for mRNA imaging agents, as intended in Aim 1. IGF1R continues to serve as a useful gateway, as we found previously for breast, pancreatic, and prostate cancer cells. Concurrent work supported by NIDA illustrated that the μ -opioid receptor also functions as a gateway for mRNA imaging agents.

Surgical determination of whether to proceed with a pancreatectomy requires 3D spatial awareness for many structures of interest (tumor, vasculature, pancreas, and spleen) and how the tumor impacts upon each. Typically the decision and planning steps are based upon two dimensional (2D) medical images of the patient from a variety of sources including computed tomography (CT), magnetic resonance imaging, ultrasound, photoacoustic imaging, or positron emission tomography (PET). Aim 2 sought to determine whether three-dimensional (3D) presentation of PET/CT data would benefit surgeons preparing for a procedure. 3D rendering and co-registration of PET and CT thoracic scans from a patient with a ductal pancreatic mass were created, then evaluated by 6 experienced surgeons by answering a questionnaire. Contrast-enhanced CT fused with PET provided a significantly more lifelike presentation than standard CT, increasing the usefulness of the presentation, according to the surgeons' evaluations. Hence, 3D simulation of a specific patient from fused PET/CT data, the goal of Aim 2, could be a useful preparatory tool for surgeons prior to making the first incision. A haptic model of the same patient is being developed, and will be evaluated by the same 6 surgeons once

the texture and responsiveness of the pancreas are satisfactory.

So what? External imaging of disease gene expression in live patients will be the next step in our research path, even though EGFR lacks the properties needed for a gateway. 3D touch-and-feel manipulation of patient images in real time just before surgery will enable shorter procedures with fewer complications.

F. REFERENCES

1. Ferguson, K.M., Berger, M.B., Mendrola, J.M., Cho, H.S., Leahy, D.J., and Lemmon, M.A. (2003) EGF activates its receptor by removing interactions that autoinhibit ectodomain dimerization. *Mol Cell* **11**(2):507-17. PMID: 12620237.
2. Lee, J.S. and Blick, M., *Bioactive EGF peptides for promotion of tissue regeneration and cancer therapy*, U.P. 5183805, Editor. 1993, Board of Regents, University of Texas: USA.
3. Li, Z., Zhao, R., Wu, X., Sun, Y., Yao, M., Li, J., Xu, Y., and Gu, J. (2005) Identification and characterization of a novel peptide ligand of epidermal growth factor receptor for targeted delivery of therapeutics. *FASEB J* **19**(14):1978-85. PMID: 16319141.
4. Case, D.A., Cheatham, T.E., 3rd, Darden, T., Gohlke, H., Luo, R., Merz, K.M., Jr., Onufriev, A., Simmerling, C., Wang, B., and Woods, R.J. (2005) The Amber biomolecular simulation programs. *J Comput Chem* **26**(16):1668-88. PMID: 16200636.
5. Walter, T., Shattuck, D.W., Baldock, R., Bastin, M.E., Carpenter, A.E., Duce, S., Ellenberg, J., Fraser, A., Hamilton, N., Pieper, S., Ragan, M.A., Schneider, J.E., Tomancak, P., and Heriche, J.K. Visualization of image data from cells to organisms. *Nat Methods* **7**(3 Suppl):S26-41. PMID: 20195255.
6. Sanders, J.M., Wampole, M.E., Thakur, M.L., and Wickstrom, E. (2011) Molecular dynamics study of EGFR ligand-dependent activation and asymmetric dimerization. submitted. PMID.

APPENDICES

Studies in Health Technologies and Informatics 163:691-695

Three Dimensional Projection Environment for Molecular Design and Surgical Simulation

Eric WICKSTROM^{a,d}, Chang-Po CHEN^a, Devakumar DEVADHAS^b, Matthew WAMPOLE^a, Yuan-Yuan JIN^a, Jeffrey M. SANDERS^a, John C. KAIRYS^c, Martha L. ANKENY^e, Rui HU^f, Kenneth E. BARNER^f, Karl V. STEINER^f and Mathew L. THAKUR^{b,d},

^aBiochemistry & Molecular Biology, ^bRadiology, ^cSurgery, ^dKimmel Cancer Center, ^eAcademic and Instructional Support and Resources, Thomas Jefferson University, Philadelphia PA 19107

^fElectrical and Computer Engineering, University of Delaware, Newark DE 19716

Abstract. We are developing agents for positron emission tomography (PET) imaging of cancer gene mRNA expression and software to fuse mRNA PET images with anatomical computerized tomography (CT) images to enable volumetric (3D) haptic (touch-and-feel) simulation of pancreatic cancer and surrounding organs prior to surgery in a particular patient. We have identified a novel ligand specific for epidermal growth factor receptor (EGFR) to direct PET agent uptake specifically into cancer cells, and created a volumetric haptic surgical simulation of human pancreatic cancer reconstructed from patient CT data. Young's modulus and the Poisson ratio for each tissue will be adjusted to fit the experience of participating surgeons.

Keywords. Cancer, haptic, pancreas, SOFA, surgery, tumor, volumetric

Introduction

Surgery involves palpating and manipulating tissues in the operating room environment. However, sophisticated radiographic systems present only visual images. The actual assembly of organs of a particular patient must now be imagined by the surgeon before the operation. Complications that were not anticipated, such as bleeding from unusually placed arteries or veins, or unusual lesion geometry, lengthen the procedure, placing extra stress on the patient and the surgeons.

One solution is the Simbionix Procedure Rehearsal StudioTM program for the AngioMentorTM simulator that allows surgeons to upload patients' actual CT angiogram images and then perform a virtual procedure, complete with visual and haptic feedback, on that patient's anatomy [7]. But the Simbionix system only uses anatomical data.

We hypothesize that our fusion of genetic, visual, and tactile information will improve surgeons' understanding of the extent of disease and will ultimately permit surgeons to better plan operations and to prepare for the actual pathology found.

1. Methods

1.1. PET Imaging Agents for mRNA

We design novel EGFR ligands by molecular dynamics using Amber 10 [4] force fields, followed by haptic sensing of the kinetic pathway of ligand binding to the receptor. The

energetically optimal peptide selected above is extended from a solid phase support by solid phase coupling of Fmoc-L-amino acid monomers. The terminal Cys residues are cyclized. A diethyleneglycol spacer is then coupled, followed by the mutant *KRAS2* G12D PNA sequence, a second diethyleneglycol spacer, then finally a fluorophore or a DOTA chelator [8]. PNA mismatch and peptide mismatch controls are also prepared. The finished reporter-PNA-peptides are cleaved from the solid support, deprotected, purified by reversed phase liquid chromatography, and analyzed by mass spectroscopy to determine whether the desired sequence was synthesized correctly.

1.2. Volumetric Images

We assembled a prototype system for haptic manipulation of volumetric images of pancreatic cancer gene expression and anatomy. Slicer3 [5], Amira 5 (Visage Imaging) SOFA [9] and Phantom Omni manipulators (SensAble) are installed on a 3DBoxx 8570 (Boxx Technologies) with 8 computing nodes and 48 GB of RAM to support an Nvidia 5800 video card with 4 GB GPU.

1.3. Haptic Manipulation

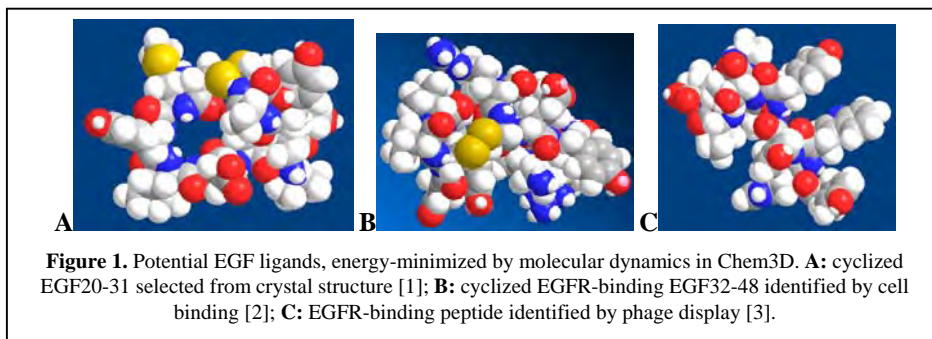
A pair of Phantom Omni manipulators is controlled by the end-user to provide translation and rotation input information for surgery instruments in the virtual reality environment. A collision detection algorithm is adopted to detect the penetration between surface meshes of virtual organs and instruments. If a mesh controlled by the haptic device is involved in a collision, the corresponding penetration volume is sampled. The haptic force is calculated using this volume and feedback is provided for the haptic device to give the end-user realistic feedback.

To render variations in haptic stiffness properties in different regions of the target tissue, we strategically place key vertices over the surface mesh. Each of these vertices contains an influence radius. As the virtual instrument enters any of these radii, the feedback force is appropriately scaled. The proximity of the surgery instrument to the vertex and a predefined base stiffness value control the scale factor, creating distinct regional haptic properties.

2. Results

2.1. Modeling and Testing of EGFR Ligands for mRNA PET Imaging Agents

The EGF central loop fragment, amino acids 20-31, CMYIEALDKYAC, with Cys-Cys disulfide bridge between Cys20 and Cys31 (Fig. 1A), was selected empirically from the crystal structure [1]. EGF amino acids 32-48,



NCVVG YIGERCQYRDLK, with Cys-Cys disulfide bridge between Cys33 and Cys42 (Fig. 1B), was selected as a second candidate ligand, based on binding to EGFR on cells [2]. GE11, YHWYGYTPQNVI, an EGFR-binding peptide identified by phage display [3] (Fig. 1C), was selected as a third candidate ligand.

The molecular dynamics docking pathway of EGF into the ligand binding pocket of EGFR was then calculated with ZDOCK, which performs rigid body docking calculations and determines their relative energies in implicit water with the appropriate dielectric constant, on Salk at the Pittsburgh Supercomputer Center (Fig. 2).

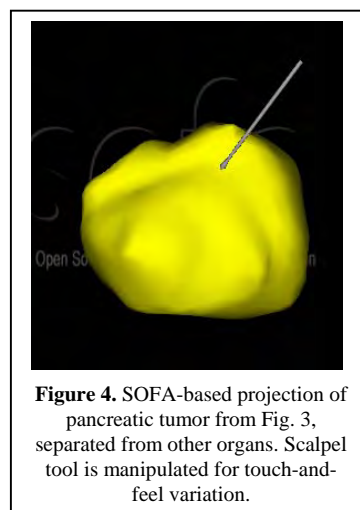
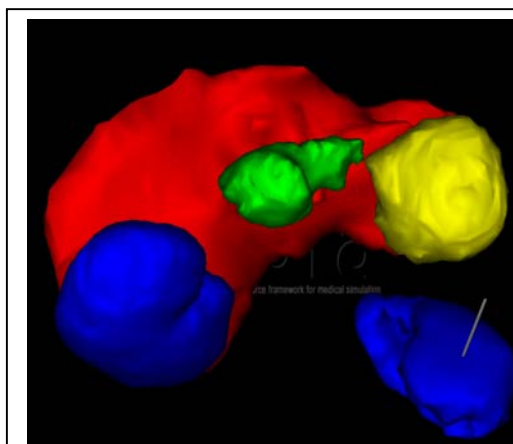
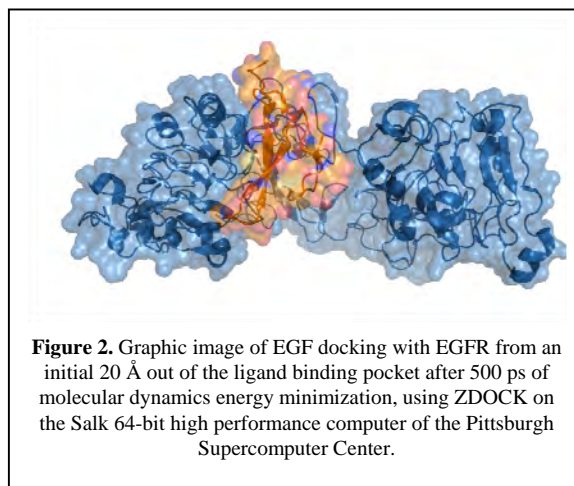
Fluorescence microscopy and flow cytometry revealed that AlexaFluor 532-EGF20-31 fails to enter cells that overexpress EGFR. On the other hand, AlexaFluor 532-GE11 enters cells whether or not they overexpress EGFR. Fullsize recombinant EGF failed to block uptake of Alexa Fluor 532-GE11. Chinese hamster ovary (CHO) cells, lacking EGFR, also took up AlexaFluor 532-GE11. This result implies that GE11 uptake is nonspecific. However, AlexaFluor 532-EGF32-48 was taken up by human AsPC1 pancreatic cancer cells that overexpress EGFR, examined by confocal fluorescence microscopy to evaluate binding.

2.2. Volumetric Simulation with Haptic Feedback

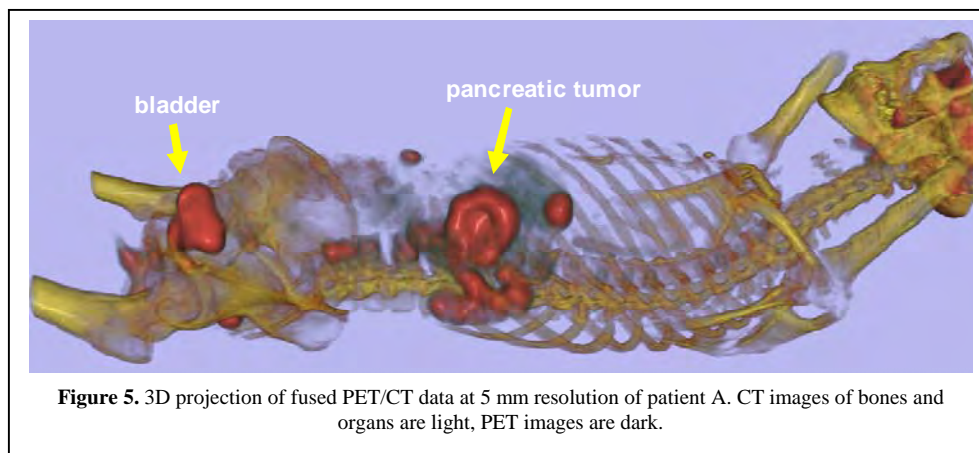
Volumetric simulation with haptic feedback manipulation of pancreatic cancer CT data from deidentified patient A (IRB approved) was carried out using SOFA (Fig. 3).

We observed that the tissue texture parameters do not yet reflect the actual feel of each organ and lesion. The pancreatic tumor was isolated (Fig. 4). Young's modulus and the Poisson ratio will be varied in a search for typical tumor texture and feel.

PET data from uptake of [^{18}F]fluorodeoxyglucose (FDG) were then overlaid on the CT data for patient A (Fig. 5). Intense FDG concentration was seen in the tumor, in agreement with the aggressive nature of the pancreatic malignancy.



Bladder uptake reflects normal excretion of FDG. The next phase of haptic development will utilize co-registered PET/CT data to highlight aggressive tumor tissue for excision.



3. Discussion

3.1 EGFR Ligands for mRNA PET Imaging Agents

EGF32-48 fragment calculations agreed with experimental cellular uptake, as well as non-binding by EGF20-31 fragment. We discovered that the energies of the entire kinetic docking pathway could be calculated in a single run, beginning with EGF translated 20 Å out of EGFR. The ZDOCK force fields were sufficient to draw EGF into the ligand binding pocket. This insight eliminates the need for separate calculations over a series of specific separations.

3.2. Volumetric Simulation with Haptic Feedback

We also observed that the haptic manipulators felt heavier than a real scalpel or retractor. This suggests a future need for wireless glove manipulators. The next phase of haptic development will utilize co-registered PET/CT data to highlight aggressive tumor tissue for excision.

Acknowledgments

This work is supported by USAMRMC/TATRC grant W81XWH-09-1-0577.

References

1. Ferguson, K.M., Berger, M.B., Mendrola, J.M., Cho, H.S., Leahy, D.J., and Lemmon, M.A. (2003) EGF activates its receptor by removing interactions that autoinhibit ectodomain dimerization. *Mol Cell* **11**(2):507-17. PMID: 12620237.
2. Lee, J.S. and Blick, M., *Bioactive EGF peptides for promotion of tissue regeneration and cancer therapy*, U.P. 5183805, Editor. 1993, Board of Regents, University of Texas: USA.
3. Li, Z., Zhao, R., Wu, X., Sun, Y., Yao, M., Li, J., Xu, Y., and Gu, J. (2005) Identification and characterization of a novel peptide ligand of epidermal growth factor receptor for targeted delivery of therapeutics. *FASEB J* **19**(14):1978-85. PMID: 16319141.
4. Case, D.A., Cheatham, T.E., 3rd, Darden, T., Gohlke, H., Luo, R., Merz, K.M., Jr., Onufriev, A., Simmerling, C., Wang, B., and Woods, R.J. (2005) The Amber biomolecular simulation programs. *J Comput Chem* **26**(16):1668-88. PMID: 16200636.

5. Walter, T., Shattuck, D.W., Baldock, R., Bastin, M.E., Carpenter, A.E., Duce, S., Ellenberg, J., Fraser, A., Hamilton, N., Pieper, S., Ragan, M.A., Schneider, J.E., Tomancak, P., and Heriche, J.K. Visualization of image data from cells to organisms. *Nat Methods* **7**(3 Suppl):S26-41. PMID: 20195255.
6. Sanders, J.M., Wampole, M.E., Thakur, M.L., and Wickstrom, E. (2011) Molecular dynamics study of EGFR ligand-dependent activation and asymmetric dimerization. submitted. PMID.
7. Duncan, J.R. and Glaiberman, C.B. (2006) Analysis of simulated angiographic procedures: part 1--capture and presentation of audio and video recordings. *J Vasc Interv Radiol* **17**(12):1979-89. PMID: 17185697.
8. Tian, X., Aruva, M.R., Zhang, K., Cardi, C.A., Thakur, M.L., and Wickstrom, E. (2007) PET imaging of *CCND1* mRNA in human MCF7 estrogen receptor-positive breast cancer xenografts with an oncogene-specific [⁶⁴Cu]DO3A-PNA-peptide radiohybridization probe. *Journal of Nuclear Medicine* **48**(10):1699-1707. PMID: 17909257.
9. Soler, L. and Marescaux, J. (2008) Patient-specific surgical simulation. *World J Surg* **32**(2):208-12. PMID: 18066615.

A Generalized Haptic Feedback Approach for Arbitrarily Shaped Objects

Rui HU, Kenneth E. BARNER, and Karl V. STEINER

Electrical and Computer Engineering, University of Delaware, Newark DE 19716

Abstract. In surgery procedures, haptic interaction provides surgeons with indispensable information to accurately locate the surgery target. This is especially critical when visual information cannot provide sufficient information and tactile interrogation, such as palpating some region of tissue, is required to locate a specific underlying tumor. However, in most current surgery simulators, the haptic interaction model is usually simplified into a contact sphere or rod model, leaving arbitrarily shaped intersection haptic feedback between target tissue and surgery instrument less unreliable. In this paper, a novel haptic feedback algorithm is introduced for generating the feedback forces in surgery simulations. The proposed algorithm initially employs three Layered Depth Images (LDI) to sample the 3D objects in X, Y and Z directions. A secondary analysis scans through two sampled meshes and detects their penetration volume. Based on the principle that interaction force should minimize the penetration volume, the haptic feedback force is derived directly. Additionally, a post-processing technique is developed to render distinct physical tissue properties across different interaction areas. The proposed approach does not require any pre-processing and is applicable for both rigid and deformable objects.

Keywords. Haptic Feedback, Surgery Simulation, Penetration Volume, Layered Depth Images.

Introduction

For many years, haptic rendering has garnered great attention in multiple fields, including surgery simulation, virtual reality and computer games. Haptic feedback in virtual reality is coupled with visual information to improve the simulation environment realism. In surgery simulation applications, haptic rendering can serve to provide surgeons with useful properties, such as tissue stiffness information, so that the user will gain a better understanding of the surgery situation through touching and palpation. For example: recently in [1], Laura *et al.* explored the possibility of adding an artificial haptic response to Phacoemulsification cataract surgery simulation to enhance training effectiveness. However, the complex geometry shape of 3D objects, especially deformable surgery objects, makes haptic rendering a computation-intensive task. In early research, to alleviate computational complexity, researchers simplified the surgery instrument into a point. Zilles *et al.* [2] successfully achieved realtime point-based haptic feedback with polygon models. In [3], Daniel *et al.* simplify multiple surgery instruments by using them as one-point haptic models. In [4], Matthias *et al.* apply the haptic feedback algorithm by Ruspini *et al.* [5] to a hysteroscopy simulator system, realizing both the single-point and multiple-point interaction in the simulator. In their organ exclusion simulation, Yoshihiro *et al.* [8] track each fingertip as points and generate the haptic force for each point using a precomputed stiffness matrix based on the finite element method (FEM). This algorithm is accurate, but relatively slow and cannot cope with topology changes. As a comparison, the Rensselaer Polytechnic Institute group members, such as Suvranu De and YiJe Lim focus on

using meshfree methods in many applications [6, 16]. Beyond the point-based haptic model, a sphere-based model is also employed in surgery simulation due to its simplicity. In [7], Peter *et al.* model the tip of a drilling instrument as a sphere. For researchers addressing the arbitrarily shaped haptic model interaction case, they typically employ methods based on the penetration depth between two triangle meshes [9, 10]. In [11], Redon *et al.* apply a real-time penetration depth calculation method for complex and non-convex meshes. However, this algorithm suffers from some penetration distance and direction approximation issue. In [12], Fisher *et al.* consider calculating the penetration volume as “The most complicated yet accurate method” to describe the extent of intersection. Following this idea, Weller *et al.* [13] proposes a new data structure, the “Inner Sphere Tree” to estimate the penetration volume. However, this algorithm relies heavily on the bounding volume hierarchy (BVH); therefore, it is not applicable for deformable objects. In [14], Faure *et al.* apply Layered Depth Image (LDI) to calculate the penetration volume for the purpose of deformation simulation, but the LDI generation method employed was too slow for real-time haptic response.

To achieve accurate haptic feedback for deformable objects, we advance the LDI method to accurately and efficiently compute the penetration volume. Three new LDIs are generated for each new haptic frame; accordingly, the proposed algorithm is well suited for soft, deformable objects. We resort to a post-processing technique to render tissue stiffness for organs with different materials at different locations, such as a relatively stiffer tumor tissue surrounded by healthy, soft body tissue.

1. Methods

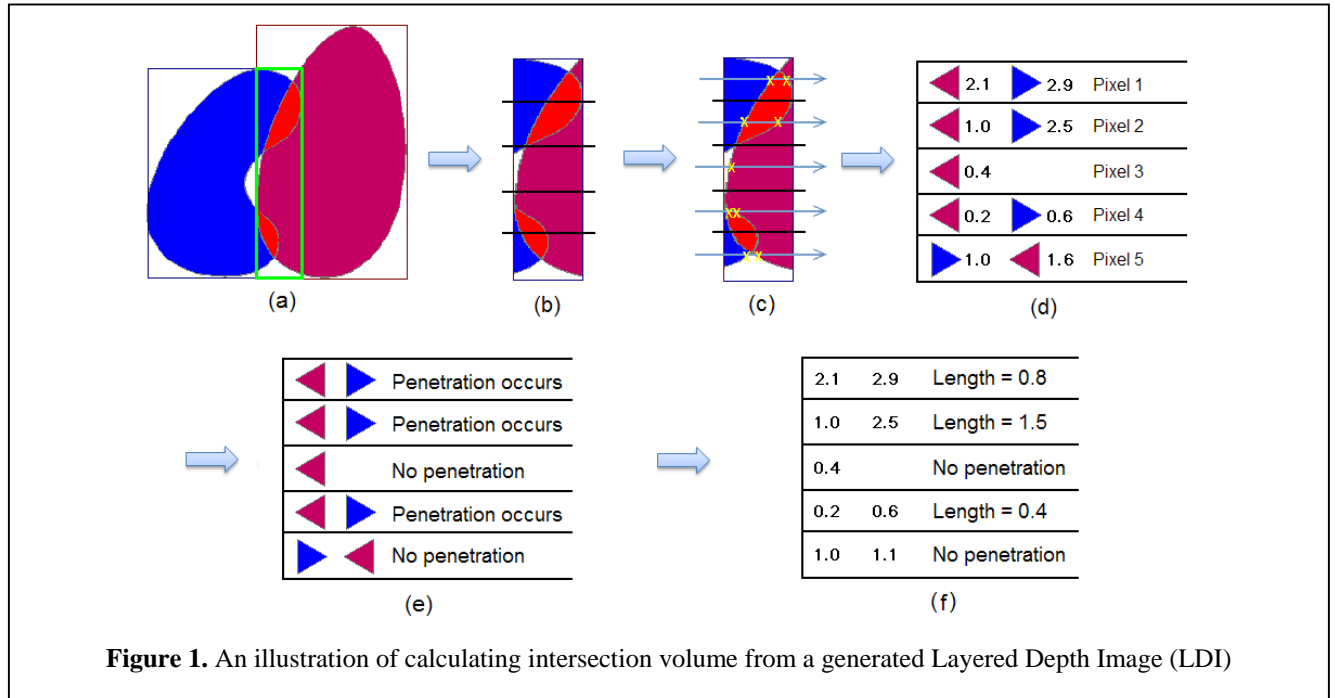
1.1. Haptic force generation

1.1.1. Layered depth image and penetration volume generation

Layered Depth Image (LDI) was first introduced as a rendering technique [17]. The LDI generation procedure is essentially a sampling process operating on the triangle mesh volume through a user-defined viewport and resolution. Suppose we shoot a ray at the center of each pixel in the viewport and the ray direction is orthogonal to the view plane. Each time the ray intersects with the target triangle mesh, a sequence of intersected fragment information is stored in the LDI. A generated LDI contains three types of information at all sampled fragments, namely: (1) the depth values through the viewing direction, (2) which object this fragment belongs to, and (3) the object normal at this fragment in the view direction.

LDI greatly facilitates determination of the penetration volume because, by sequentially scanning the normal directions and object numbers of all fragments at a pixel, we can easily find the fragment pair where two objects penetrate. This is a result of the fact that if we follow a ray, every fragment the ray encounters with a normal opposing the ray direction means that the ray is entering a mesh, while a fragment with a normal aligned with the ray direction indicates the ray is leaving a mesh. By multiplying a specific penetration length with a pixel area dependent on resolution, we approximate the penetration volume at this pixel. Figure 1 illustrates this process of penetration volume generation. In Fig. 1-(a), the bounding volume intersections of two objects are detected. The left column of the green box represents the view plane. The volume is rasterized and sampled as shown in Fig. 1-(b) and 1-(c). The generated LDI is shown in Fig. 1-

(d), where the arrow direction indicates the normal direction; the color represents the object that is sampled. We store the fragments and then pick up collision pairs in each pixel, as shown in Fig. 1-(e). Finally, in Fig. 1-(f), the length of the penetration section is calculated at each pixel.



1.1.2. Efficient LDI calculation

In the computer graphics area, researchers such as Everitt, Bavoil and Myers have been investigating ways to improve the LDI generation efficiency for years [18-20]. Recently, Liu *et al.* [15] show that the Compute Unified Device Architecture (CUDA)-based LDI generation method yields the best performance. In our implementation, we have adopted a similar algorithm for LDI generation. This is due to its excellent performance, and the fact that CUDA made parallel penetration length query and operations on penetration volume available on GPUs.

1.1.3. Volume based haptic force

Similar to [14], we define the potential energy as: $E = \frac{1}{2} kV^2$, where k is a user-defined parameter to scale this energy, and V is the penetration volume. Suppose the calculated LDI is along the Z direction. Now, we derive the final haptic force along a certain viewing direction. Given the assumption that the haptic force serves to minimize the intersection volume of two objects, the interaction force in the viewing direction (Z direction) at a given coordinate (x_a, y_a, z_a) is:

$$f_{x_a, y_a} = - \left. \frac{dE}{dz} \right|_{(x_a, y_a)} = - kV \left. \frac{dV}{dz} \right|_{(x_a, y_a)} \quad (1)$$

If we take the haptic force direction into consideration, i.e. if the haptic-related mesh is pushed from right to left, the haptic force should follow the negative X-axis direction. Also, if no haptic model is involved, no haptic force should be generated. The direction factor should be:

$$D = O_L - O_R, \quad (2)$$

where O_L and O_R stand for the force direction influence from the left and the right fragment. We now have:

$$O_i = \begin{cases} 1, & \text{fragment } i \text{ belongs to haptic object} \\ 0, & \text{fragment } i \text{ belongs to non-haptic object} \end{cases} \quad (3)$$

By combining the factors together, the haptic force in the Z direction is the integration of forces at all penetration volume boundaries:

$$f_Z = \int_x \int_y -kV \frac{dV}{dz} D \, dy \, dx \quad (4)$$

If we write Equation (4) into a discrete form for computer-based calculation, with every unique X and Y standing for a pixel on the viewport, the term dV/dz automatically becomes 1. Therefore we have:

$$F_Z = \sum_x \sum_y -kVD = -k \sum_x \sum_y VD \quad (5)$$

Equation (5) indicates that the final haptic feedback force in one direction is simply the sum of all penetration volume weighed by force direction. This greatly facilitates the algorithm programming. By repeating this process two more times for the X and Y directions, we generate the haptic force, which can be sent to the haptic device directly or used for post-processing. We have also developed an algorithm to infer the LDI in the Y and Z viewing direction from the LDI in X direction. This technique further reduces the overall computation time by about one half to two thirds.

1.2. Haptic force post-processing

In order to render the distinct feedback forces at different locations, we apply the following post-processing method called local stiffness vertex method to the calculated haptic force:

1. At simulation initiation, load a series of vertex information into memory. The information of each vertex i consists of three pieces of information: (1) the vertex number, N_i ; (2) the influence radius of this vertex, R_i ; and (3) the stiffness parameter of this vertex, S_i .
2. During simulation, keep monitoring the position of the instrument center P_c .
3. The distance between the instrument center and any stored vertex i , D_{ci} is compared with the vertex radius R_i .
4. If any D_{ci} is smaller than R_i , we use the following equation to scale the haptic force:

$$F_{post} = F \sum_V \left(\frac{a_i^2 \left(\frac{D_{ci}}{R_i} \right)}{\sum_V a_i \left(\frac{D_{ci}}{R_i} \right)} S_i \right) \quad (6)$$

where $a_i(x)$ is a monotonic continuous function, with $a_i(0) = 1$, $a_i(1) = 1/S_i$. It is essentially an influence kernel describing how the stiffness parameter decreases from the center of the vertex to its surrounding area.

We have to note that the aforementioned post-processing algorithm may not be effective on large instruments since a center cannot describe the real shape of a large instrument sufficiently. We are finalizing improvements to the algorithm that dynamically add stiff-ness properties to penetration volumes. This algorithm will support large, arbitrary instruments.

2. Results

The proposed algorithm has been implemented on a PC with an i7-930 CPU and a GeForce GTX 295 video card. Here we present the results of evaluating algorithm under various scenarios. In [13], it is stated that the LDI-based volume calculation “is restricted to image space precision.” Consequently, it is important to evaluate how the algorithm is influenced by insufficient volume sampling, which is caused by low resolution. The generated haptic feedback forces, based on different resolutions, are compared with previously recorded high-resolution (512×512) results. The normalized absolute error is calculated as:

$$E = |F_m - F_{512}| / F_{512} \quad (7)$$

where F_m is the m-resolution output force and F_{512} is the high-resolution force used as a benchmark.

Three scenarios are adopted to test the algorithm. In each scenario, two objects are colliding. The objects used in each test environment are: (1) a tumor and a cylindrically-shaped object; (2) a tumor-shaped object and a duo-denum-shaped object; and (3) a tumor-shaped object and a bunny-shaped object. The numbers of triangles of the aforementioned meshes are: tumor: 10,000; cylinder: 1,340; duodenum: 2,000; bunny: 70,000. The simulation scenarios and the feedback force error are shown as below:

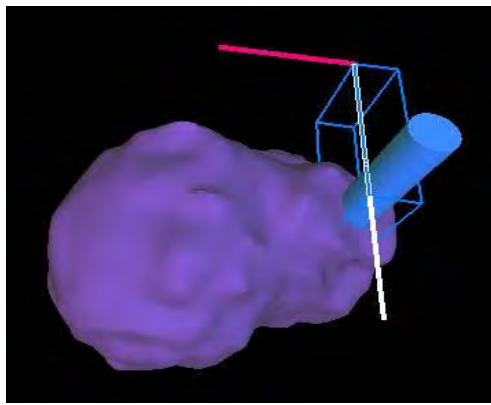


Figure 2. Tumor-cylinder test scenario

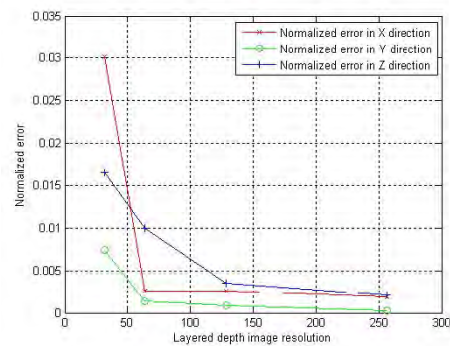


Figure 3. Error comparison for tumor-cylinder scenario

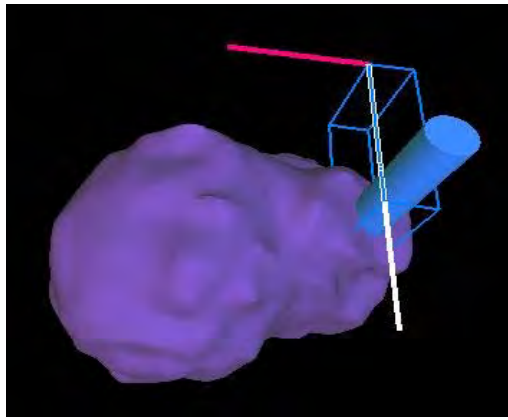


Figure 4. Tumor-duodenum test scenario

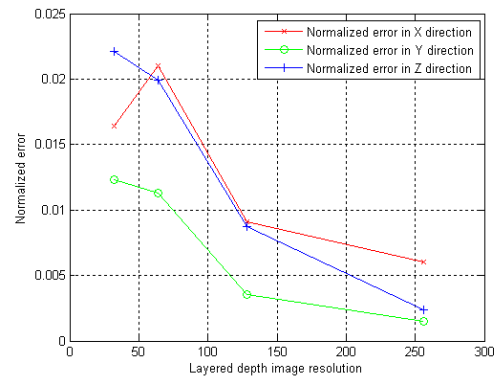


Figure 5. Error comparison for tumor-duodenum scenario

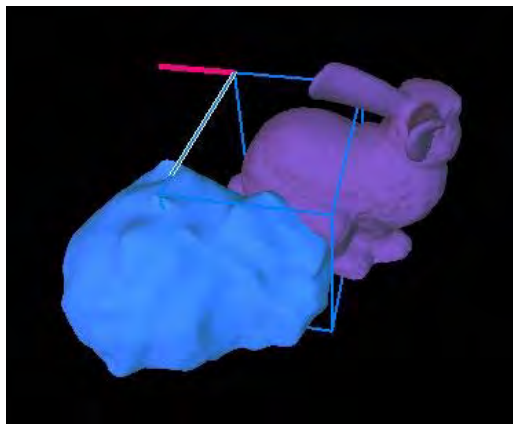


Figure 6. Tumor-bunny test scenario

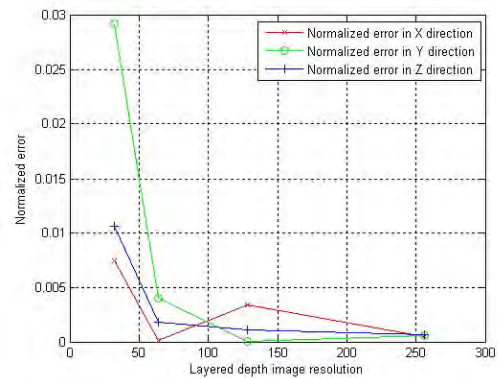


Figure 7. Error comparison for tumor-bunny scenario

From Figures 3, 5 and 7, we can easily see that volume errors do have a negative impact on the haptic force. However, in most cases, the influence is less than 3%. Therefore, the lower resolution setting can also be used for real-time simulations.

Another aspect critical in haptic simulation is haptic refreshment rate. To evaluate the computation time cost of proposed algorithm, we tested the haptic frame rate for the three intersection scenarios. Fig. 8 shows the frame rate comparison.

Judging from the error and frame rate, we can conclude that, although adopting a resolution of 32 can yield a higher haptic response rate, the error may be relatively large. Using a resolution of 64 is more reliable and yields an acceptable refreshment rate of approximately 200 FPS. Since the proposed

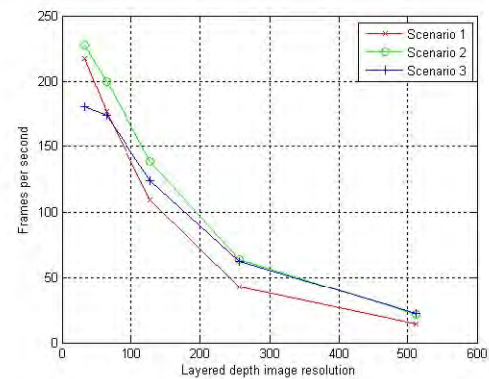


Figure 8. Refreshment rate comparison for five different image resolutions (32, 64, 128, 256, 512).

algorithm implementation GPU-based, the CPU can process its own tasks in parallel, while the LDI is being generated on the video card.

We use a scene describing a “cylinder sweeps across a cube” to demonstrate that by introducing different local stiffness vertices, the local stiffness vertex method can lead to a varying feedback force effect. The scene is shown in Fig. 9. In this scenario, when no local stiffness vertices are considered, the only haptic feedback force calculated is a constant force always facing the positive Y-axis in this scenario.

To artificially introduce different stiffness properties at individual regions of this scene, i.e. making the cube feel stiffer or softer at different locations, we consider three stiffness vertex placement scenarios: (1) Conventional setting, no local stiffness vertex is included. (2) One local stiffness vertex with a large influence range is located at position “a” in Fig. 9. In this scenario, the middle part of cube will generate additional force, making it feel stiffer. (3) Two local stiffness vertices with different influence ranges and stiffness values at locations “b” and “c” in Fig. 9. In this scenario, the cube will feel stiffer at location “b” and “c” while softer in the center. In Fig. 10, the feedback forces in all three scenarios are monitored and compared. Feedback forces are normalized to scenario (1), the non-vertex case calculated force. The kernel function adopted is a raised cosine function:

$$a(x) = \frac{1}{2}(1 + \cos(x)) \quad (8)$$

In Fig. 10, the feedback force is measured as the cylinder travels from point “b” to “c”. Monitored forces show the proposed algorithm successfully renders the desired stiffness properties. By introducing the local stiffness vertex method, the output force is drastically converted from its original flat pattern into a curve. If one can carefully spread local stiffness vertices over the target tissue, realistic heterogeneous stiffness properties can be easily perceived, thus further enhancing the realism of surgery simulators.

We have integrated the haptic feedback algorithm into our simulator with constantly deforming objects. Vertices with higher stiffness values are scattered around the deformable tissue representing the tumor area in an organ. Surgical residents can use multiple tools to touch and feel the location of these tumors for training exercises.

3. Conclusions

The main contribution of this paper is an LDI-based haptic feedback algorithm for deformable objects with large volume intersections. Unlike past

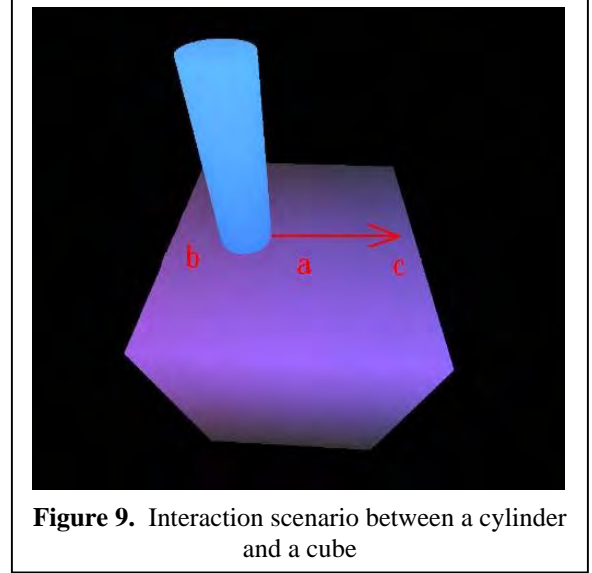


Figure 9. Interaction scenario between a cylinder and a cube

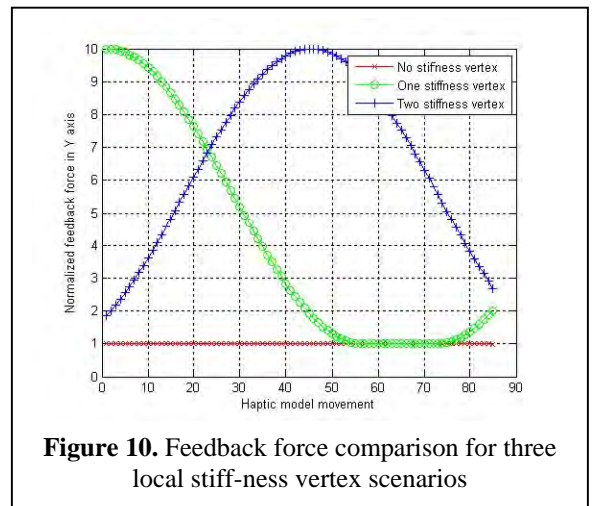


Figure 10. Feedback force comparison for three local stiffness vertex scenarios

algorithms based on simplifying the haptic model, our method operates on the original volume so that the irregular objects interactions are accurately presented and rendered. Thus, the algorithm can be widely applied in open surgery simulations for different instruments and arbitrary anatomy.

Future work in this algorithm will include reinforcing the post-processing method for rendering different physical properties and refining the parameters such as stiffness factor, radius and kernel function in post processing. We will work closely with our surgical collaborators to address these issues.

Acknowledgements

This work is supported by USAMRMC/TATRC grant W81XWH-09-1-0577.

References

- [1] Doyle, L., Gauthier, N., Ramanathan, S., Okamura, A. "A Simulator to Explore the Role of Haptic Feedback in Cataract Surgery Train-ing", Medicine Meets Virtual Reality (MMVR) 15, 2008.
- [2] Salisbury, Z., Zilles, B., Salisbury, K.: "A constraint based god-object method for haptic display". In Proc. of the IEEE Conference on Intelligent Robots and Systems, 1995.
- [3] Bielser, D., Gross, H., Open surgery simulation, Medicine Meets Virtual Reality (MMVR) 2002,
- [4] Harders, M., Spaelter, U., Leskovsky, P., Szekely, G., Bleuler, H., "Haptic interface module for hysteroscopy simulator system"., Medicine Meets Virtual Reality (MMVR) 15, 2008.
- [5] Ruspini, D., Kolarov, K., and Khatib, O.. "The Haptic Display of Complex Graphical Environments". SIGGRAPH 97 Conference Proceedings, 1997.
- [6] Lim, Y-J., Wei, J., De, S. "On some recent advances in multimodal surgery simulation: a hybrid approach to surgical cutting and the use of video images for enhanced realism". Presence 2007.
- [7] Trier, P., Noe, K., Sørensen, M., and Mosegaard, J.. "The Visible Ear Surgery Simulator". Medicine Meets Virtual Reality (MMVR 16), 2009,
- [8] Kuroda, Y., Hirai, M., Nakao, M., Sato, T., Kuroda, T., Nagase, K., Yoshihara, H., "Organ exclusion simulation with multi-finger haptic interaction for open surgery simulator". Medicine Meets Virtual Reality (MMVR) 15, 2008.
- [9] Kim, Y., Otaduy, M., Lin, M. and Manocha, D. "Six Degree-of Freedom Haptic Display Using Localized Contact Computations", in the Tenth Symposium on Haptic Interfaces For Virtual Envi-ronment and Teleoperator Systems, 2002.
- [10] Kim, Y., Lin, M., Manocha, D., "Fast penetration depth estimation using rasterization hardware and hierarchical refinement". Work-shop on Algorithmic Foundations of Robotics (WAFR). 2002.
- [11] Redon, S., and Lin, M., "A fast method for local penetration depth computation". Journal of Graphical Tools. 2005.
- [12] Fisher, M., and Lin, C., "Fast penetration depth estimation for elastic bodies using deformed distance fields", Proceedings of In-ternational Conf. on Intelligent Robots and Systems, 2001.
- [13] Weller, R., Zachmann, G., "A Unified Approach for Physically-Based Simulations and

Haptic Rendering”, ACM Siggraph Video Game Symposium, Proceedings of the 2009 ACM SIGGRAPH Symposium on Video Games, 2009.

[14] Faure, F., Barbier, S., Allard, J., and Falipou, F. 2008. “Image-based collision detection and response between arbitrary volume-tric objects”. In ACM Siggraph/Eurographics Symposium on Computer Animation, SCA 2008, 2008.

[15] Liu, F., Huang, M., Liu, X., and Wu, E. “Single pass depth peeling via CUDA rasterizer”. International Conference on Computer Graphics and Interactive Techniques archive, SIGGRAPH 2009: talks, 2009.

[16] De, S., Lim, Y-J., Manivannan M, Srinivasan MA. “Physically realistic virtual surgery using the point-associated finite field (PAFF) approach”. Presence: Teleoperators & Virtual Environments. 15(3), 2006.

[17] Shade, J., Gortler, S., He, L., and Szeliski, R., Layered Depth Images. Computer Graphics, SIGGRAPH '98 Proceedings, 1998.

[18] Everitt C.: Interactive order-independent transparency. Tech. rep., NVIDIA Corporation, 2001.

[19] Louis Bavoil, Myers K.: Order independent transparency with dual depth peeling. NVIDIA OpenGL SDK, 2008.

[20] Myers, K., Bavoil, L., Stencil routed A-buffer. SIGGRAPH '07: ACM SIGGRAPH 2007 Sketches. ACM, 2007.

Sanders, J. M., and Wickstrom, E. (2011) Ligand-dependent activation and the structural basis of negative cooperativity in EGFR: a molecular dynamics study. Protein Society 25th Anniversary Symposium, Boston, Massachusetts, July 23-27.

The Erythroblastic Leukaemia Viral Oncogene Homolog (ErbB) receptor family consists of four structurally related receptor tyrosine kinase (RTKs) involved in numerous cellular processes. Each member of the ErbB family contains an extracellular domain, a single pass transmembrane domain and an intracellular kinase domain regulated by a juxtamembrane domain. Twelve known ligands have been identified that control ErbB receptor activation. In the absence of an activating ligand, each ErbB receptor adopts an auto-inhibited conformation, with the exception of ErbB2, controlled by several loose intramolecular interactions. Ligand binding to the extracellular domain of an ErbB receptor promotes large scale conformational changes that allow for receptor dimerization. ErbB1, or Epidermal Growth Factor Receptor (EGFR), was the first to be identified and is the most well studied as aberrant EGFR signaling has been identified in multiple cancer types. While biochemical and biophysical studies of the extracellular domain of EGFR (sEGFR) have enhanced our knowledge of ligand-dependent activation, little is known about the intrinsic dynamics of the receptor on the cell surface. Molecular Dynamics (MD) simulations allow us to explore dynamics that are otherwise inaccessible with bench experiments. Here we demonstrate that EGF binding to sEGFR alters the conformational sampling by disrupting coupling of key auto-inhibitory interactions. To address the allosteric effects of EGF binding, we simulated a singly ligated sEGFR dimer. Our results suggest that asymmetric in the binding interface caused by EGF binding distorts the second binding site. The occlusion of the second binding site most likely explains the negative cooperativity observed in cell binding assays and argues against the existence of distinct EGFR receptor populations. Our results are confirmed by experimental x-ray structures of *Drosophila* EGFR, a homolog to human EGFR. These observations, previously not observed experimentally, greatly enhance our understanding of the molecular mechanism of human EGFR activation and may be applicable in other ErbB systems.

Molecular Dynamics Study of EGFR Ligand-Dependent Activation and Asymmetric Dimerization

Jeffrey M. Sanders¹, Matthew E. Wampole¹, Mathew L. Thakur^{2,3}, and Eric Wickstrom^{1,3*}

Departments of ¹Biochemistry & Molecular Biology, ²Radiology, and ³Kimmel Cancer Center
Thomas Jefferson University, Philadelphia, PA 19107

*Department of Biochemistry and Molecular Biology, Thomas Jefferson University,
Philadelphia PA 19107. Phone: 215.955.4578, Fax: 215.955.4580. Email: eric@tesla.jci.tju.edu

ABSTRACT

The epidermal growth factor receptor (EGFR) is a member of the ErbB receptor tyrosine kinase (RTK) family that plays a pivotal role in cell proliferation, differentiation and migration. While x-ray structures have provided insight into EGFR function, the conformational pathway(s) of ligand-dependent activation are not well understood. Using molecular dynamics (MD) techniques we demonstrate that EGF binding to the extracellular domain of EGFR (sEGFR) disrupts auto-inhibitory intramolecular interactions by increasing the distance between the so-called “dimerization arm” and domain IV. To investigate early ligand binding effects on sEGFR dimers, we constructed a singly ligated sEGFR dimer for simulation. MD simulations of the singly ligated sEGFR dimer exhibited asymmetrical motion in each monomer and a decrease in the size of the second EGF binding pocket by 10 Å. Free energy calculations indicated that asymmetrical dimerization with only one EGF-sEGFR monomer is more energetically favorable than dimerization of two ligated sEGFR monomers by 2.88 kcal·mol⁻¹. To see if asymmetrical motion can be extended to ErbB heterodimers, we simulated a model sEGFR-ErbB2 dimer. This heterodimer also exhibited asymmetrical motion. These results suggest asymmetrical dynamics in sEGFR may play an essential role in receptor activation and cooperativity.

KEYWORDS: Epidermal growth factor, EGFR, cooperativity, ErbB2, molecular dynamics, protein dynamics

INTRODUCTION

The ErbB receptor family consists of four structurally related receptor tyrosine kinases (RTK) that play pivotal roles in cell differentiation, proliferation and migration [10]. Early studies of ErbB receptors were the first to highlight the importance of ligand-induced dimerization in intracellular signalling [11]. EGFR is one of the most well studied RTKs as aberrant signalling and mutations in EGFR have been implicated in several cancer types. Several crystallographic and biophysical studies have shed light on the mechanism of ligand-dependent dimerization leading to receptor activation [1, 12, 13]. These studies demonstrated that large scale conformational changes occur in EGFR upon EGF binding, shifting the conformational equilibrium from an auto-inhibited (tethered) state to an un-inhibited (untethered) dimer-competent state (Figure 1). While the process of EGF-induced dimerization of EGFR is well characterized, several gaps in the molecular mechanism of EGFR activation still remain, particularly the negative cooperative effects EGFR exerts on EGF binding [14-16].

The first x-ray structure of the monomeric extracellular domain of EGFR (sEGFR) showed 4 domains spanning 620 amino acids in an auto-inhibited conformation, based on several intramolecular interactions between domains II and IV [1]. Domains I and III adopt a β -solenoid fold and are homologous ligand binding domains, while II and IV are cysteine-rich domains with extended rod-like structures. Structures of the other ErbB receptors [17-19] showed several common features, with the exception of ErbB2, including a dimerization arm in domain II interacting with domain IV and additional intramolecular interactions that prevent dimerization in the absence of an activating ligand (Figure 2). Results of single molecule optical imaging studies of EGFR indicated that dimerization can occur without an activating ligand [20]. However, ligand-independent EGFR dimer complexes were transient; kinase activity was not detectable [20]. Small angle x-ray scattering studies of sEGFR concluded that receptor dimerization is ligand-dependent as sEGFR adopts a compact auto-inhibited conformation in the absence of EGF and upon addition of EGF forms a dimer *in vitro* [13].

While these studies have shown that EGFR adopts two distinct conformational states in the presence or absence of ligand binding, the dynamics of sEGFR are still poorly understood. Previous molecular dynamics (MD) simulations of EGFR dimers have explored dynamics under different solvent conditions, higher order oligomer states, and interactions with the cell membrane surface [21, 22]. What have not been investigated are the initial events that occur upon ligand binding that drive the conformational transitions necessary to form EGFR dimers.

EGF binding to EGFR is thought to be a negatively cooperative process. Scatchard plots of EGF binding yield a concave up curve, indicative of either multiple independent sites or negative cooperativity [14-16]. The existence of multiple independent sites has been shown to be unlikely, as independent equivalent two-site modeling of EGF binding curves does not agree with previous experiments [23]. In contrast, asymmetrical binding events on an EGFR dimer led to a model for negative cooperativity [14]. That view was reinforced by a recently solved crystal structure of a singly ligated EGFR dimer from *Drosophila* [24]. In the case of *Drosophila*, EGFR binding of one Spitz (EGF homolog) molecule causes structural rearrangements that partially occlude the second binding site. Based on the asymmetric dimer structure, it was concluded that partial occlusion of the second site may be a common feature of all EGFRs, and may have functional relevance in development and in the formation of ErbB heterodimers [25].

In order to explore ligand-dependent activation of sEGFR and conformational effects that might contribute to asymmetric and possibly anti-cooperative sEGFR complexes, we carried out MD simulations. We examined models of (a) auto-inhibited sEGFR structures with and without EGF, (b) a singly ligated sEGFR dimer, and (c) a sEGFR-ErbB2 heterodimer. Our results suggest that the extracellular domain of EGFR might play a role, not previously observed, in regulation of negative cooperativity, independent of transmembrane and extracellular domains. We also conclude that the failure of previous *in vitro* experiments to observe anti-cooperative bind in the extracellular domain of EGFR may be due to the time scales (seconds to minutes) of each technique. The asymmetric dimer conformations observed for a singly ligated EGFR dimer and EGFR-ErbB dimer are mostly like formed in the microsecond to millisecond time domains and stabilized by the transmembrane and intracellular domains.

MATERIALS AND METHODS

Simulation Models

Four systems were simulated in this study. The first two systems were based on the monomeric holo-sEGFR structure including bound EGF (PDB code 1NQL). All oligosaccharides were removed from each polypeptide. In the apo-EGFR system, the EGF molecule was also removed. The third model was based on the crystal structure of the activated sEGFR dimer (PDB code 1IVO) with re-refinement to incorporate domain IV (PDB code 3NJP). To generate a singly ligated dimer, one of the EGF molecules was removed. The fourth system was constructed by modeling an EGFR-ErbB2 heterodimer based on the EGFR dimer structure. First the structure of ErbB2 (PDB code 1N8Z) was edited by removing the trastuzumab Fab fragment. Several loops were not resolved in the ErbB2 crystal structure, so each loop was modelled with SWISS-MODEL (<http://swissmodel.expasy.org/>). The heterodimer was constructed by aligning the dimerization arm of ErbB2 to the dimerization arm of one EGFR molecule in the EGFR dimer structure. All alignments were performed in PyMOL and all images were produced in VMD and PyMOL [26, 27].

Molecular Dynamics (MD) Simulations

The tleap module of AMBER10 was used to create parameter and topology files for the MD simulations using the AMBER ff03 force field [28]. Hydrogen atoms were added and ionizable residues (histidines) were set to predicted protonation states at pH 7.0. Na⁺ counterions were added to each system to achieve neutrality. Solvent molecules were added using a TIP3PBOX water box with a minimum spacing of 10.0 Å from the box edges to the protein molecule. Each system contained >200K atoms.

Energy minimization on each system was performed in a two-step process. First the protein atoms were restrained and the water molecules were allowed to relax over 1000 steps. The entire system was then subjected to energy minimization using the steepest descent method for the first 1000 steps, followed by the full conjugate gradient method for an additional 2400 steps. Each system was then heated to 300K for 100 ps followed by a 50 ps constant pressure simulation to adjust the water density to 1 g/mL. An additional 500 ps simulation was run prior to production simulations to allow for further temperature and pressure equilibration. Production runs were performed using a canonical ensemble (NVT) scheme. Langevin dynamics with a collision frequency of 2.0 were used for temperature regulation, ii) the SHAKE algorithm was used to constrain all covalent bonds involving hydrogen atoms, and iii) the particle mesh Ewald (PME) method was employed to treat long range electrostatics and van der Waals forces with an integration step of 2.0 fs. Production simulations for both EGFR systems were run for 70 ns. The singly ligated EGFR dimer was run for 25 ns and the EGFR-ErbB2 heterodimer simulations were performed for 16 ns.

Principal Component Analysis (PCA) of Trajectories

MD trajectories were analyzed and compressed using the AMBER module ptraj for analysis. PCA analysis was done using ProDy 0.6.1 and MDanalysis [29, 30]. PCA was performed by decomposing the covariance matrix for each snapshot of the trajectory ensemble. The covariance matrix is a 3N x 3N matrix for a protein of N residues given by their C- α atom coordinates (x) in phase space ($i, j = 1, \dots, 3N$) and is computed as

$$\sigma = \langle (x_i - \langle x \rangle_i)(x_j - \langle x \rangle_j) \rangle.$$

The eigenvectors, also called the principal components (PCs), correspond to a linear basis set of the distribution of MD snapshots. Projections of the first three PCs were used to construct correlated fluctuation maps for all residues. All PCA graphs were made using ProDy and matplotlib in python (<http://matplotlib.sourceforge.net/>). All structural renderings of PCs were made using the Nmviz plugin feature of ProDy in VMD.

RMSD of trajectory analysis

The RMSD over the time course of each trajectory was calculated by using the RMSD Trajectory tool in VMD. To quantify domain fluctuations, the RMSD values for each domain in EGFR were calculated for each snapshot in the simulation.

Calculation of pairwise distances and RMSF of residues

The RMSF of each residue were calculated using ptraj by processing each compressed MD trajectory for a given system. Pairwise distances between residues were measured by calculating the distance between C- α of each residue for each snapshot along the simulation trajectory. Pairwise distances were also calculated between the center of mass for the dimerization arm (residues 246-250) and the center of mass for the second disulfide loop of domain IV (residues 558-567).

Free Energy Calculations

Free energy calculations of each simulation were performed using SEQMOL (provided by BiochemLabSolution.com) by using coordinate files constructed at the last time step of each trajectory. For comparison, crystal structures of singly ligated *Drosophila* EGFR (PDB code 3LTG), fully ligated *Drosophila* EGFR (PDB code 3LTF) and fully ligated human EGFR dimer (PDB code 3NJP) were also submitted to obtain theoretical free energy changes.

RESULTS

Simulations of auto-inhibited sEGFR

To gain insight into the molecular mechanism of ligand-dependent activation of EGFR, we simulated four systems of the extracellular domain of EGFR (sEGFR) in both auto-inhibited and un-inhibited conformational states. EGFR is known to exist in conformational equilibrium between these two states (12). The addition of EGF, or other activating ligand, shifts the equilibrium toward the active state. To model the early conformational changes induced by EGF binding we performed simulations of the monomeric sEGFR in the presence and absence of EGF. After 70 ns of simulation we analyzed each trajectory. Since sEGFR is a large multi-domain protein, we did not expect to capture the conformational pathway that leads to a dimer-competent conformational state within the time scales of conventional MD simulations. Instead we focused on conformational changes that occur immediately after EGF binds to domain I. We noticed that the binding of EGF to sEGFR slightly altered domain motion (Figure 3A & 3B). EGF binding reduced the RMSD fluctuations in domain II from 5 Å to 4 Å. After 70 ns the sEGFR without EGF (Figure 3D) adopted a similar conformation to the auto-inhibited structures of ErbB3 and ErbB4, while the sEGFR with EGF adopts a different, possibly an intermediate, conformational state.

Previous studies have shown that intramolecular interactions between the “dimerization arm” of domain II and the “tethering arm” of domain IV are important for preventing ligand-independent activation and negative cooperativity by dimerization (Figure 2A) [31]. To explore this role of the dimerization arm, we monitored the trajectories of the dimerization arm and domain IV. Our prediction was that EGF binding should force the dimerization arm to disengage from domain IV. To quantify our results we measured the distance between the center of mass of the tip of the dimerization arm (residues 246-250) and the center of mass of the second disulfide loop (residues 558-567) on domain IV (Figure 5A). In the absence of EGF, the change in distance between the two loops was less than 1 Å. EGF binding, however, caused a stepwise increase in separation distance during the 70 ns course of the simulation (Figure 5B).

To determine the “essential dynamics” of the dimerization arm and we performed PCA on the MD trajectories for sEGFR and EGF bound to sEGFR. PCA is frequently used to determine the direction and greatest variance in atomic motion in MD simulations and has also been used to predict conformational changes from multiple crystal structures [32-34]. PCA of each simulation showed altered conformational sampling of the dimerization arm (Figure 4). In the absence of EGF, both the dimerization arm and tethering arm fluctuated about an equilibrium position with no net correlated motion. Binding of EGF to domain I resulted in increased fluctuations of the dimerization arm and an increase in correlated motion between the dimerization arm and the tethering arm.

Simulations of singly ligated sEGFR dimer

To investigate the negative cooperative effects observed in binding assays (23), we performed a simulation with a singly ligated sEGFR dimer. Recently the structures of *Drosophila* EGFR (dEGFR) in different ligation states were solved [24]. *Drosophila* EGFR is highly homologous (35%) to human EGFR and retains negative cooperativity *in vitro*, unlike human sEGFR. *Drosophila* EGFR forms an asymmetric dimer that is loosely associated when one Spitz ligand and exhibits half-site reactivity. These effects have not been seen previously in biophysical studies for human sEGFR. We therefore chose to simulate a singly ligated human sEGFR with the prediction that it would adopt an asymmetrical conformation similar to that seen in *Drosophila* EGFR. Results from the 25 ns simulation confirmed that dimerization was retained in the presence of only one EGF molecule, but imposed structural restraints on the unligated portion of the sEGFR dimer, resulting in an asymmetrical conformation.

We used PCA to analyze the asymmetrical motion observed in the singly ligated dimer simulation. Motion along the first PC in the unligated half was greatly affected by the lack of EGF bound to domains I and III. The motion in domain II along the dimer interface was asymmetrical but did break contacts made by each dimerization arm. These motions were propagated to domains I and III on the unligated half. The positions of these domains were held fixed in the EGF-ligated half. Without EGF in the unligated portion, domains I and III moved toward each other, distorting the binding pocket and decreasing the accessible surface area for a ligand to bind.

To quantify the motions of domains I and III, we measured the distances between three pairs of residues on different sections of the EGF binding surface: *d1* (Tyr45 to Phe357), *d2* (Asn12 to His346) and *d3* (Arg29 to Phe412). By the end of a 25 ns simulation, all three distances decreased on the unligated half relative to the ligated half (Figure 6). The greatest

change, 10 Å, occurred in the distance between Tyr45 and Phe357 by for the unoccupied binding site, while the EGF-bound half remained constant.

In addition to monitoring structural changes, we sought to determine the energetics of binding for a second EGF to a singly ligated dimer. If sEGFR retains negative cooperativity, there should be a difference in binding affinities between each binding site on the dimer. Using SEQMOL's free energy solver, we calculated the binding energy for EGF binding after 25 ns of simulation (Table 1). We obtained a free energy change of $\Delta G = -23.16 \text{ kcal}\cdot\text{mol}^{-1}$ for EGF binding at 298 K (25°C). The free energy of dimerization was also calculated and found to be $\Delta G = -20.66 \text{ kcal}\cdot\text{mol}^{-1}$.

To compare our results to a fully ligated sEGFR dimer we performed the same analysis on the sEGFR dimer structure with domain IV modelled. Unexpectedly, the binding energies for each EGF molecule were not equal prior to relaxing the structure using MD. The difference between binding events was $1.96 \text{ kcal}\cdot\text{mol}^{-1}$, which might reflect asymmetry within the crystal structure. Differences in dimerization energy are another possible factor that might lead to negative cooperativity. A single sEGFR with bound EGF, dimerizing with a second unligated sEGFR, might be more energetically favorable than dimerization of two EGF+sEGFR molecules. The $\Delta\Delta G$ for the difference was $-2.78 \text{ kcal}\cdot\text{mol}^{-1}$, suggesting that asymmetrical dimerization is more energetically favorable than symmetrical dimerization with both sEGFR bound to EGF.

We compared these results with free energy calculations on the two asymmetrical *Drosophila* EGFR crystal structures that exist in singly ligated and fully ligated states. A fully ligated *Drosophila* EGFR, unlike sEGFR, appears as an asymmetrical dimer in the crystal structure. As in the sEGFR dimer crystal structure, the binding energies of each Spitz molecule, a *Drosophila* EGF homolog, were not equal ($\Delta\Delta G = 1.90 \text{ kcal}\cdot\text{mol}^{-1}$). The free energy change of dimerization, however, was more negative than the value for sEGFR+EGF dimerization ($\Delta\Delta G = -2.53 \text{ kcal}\cdot\text{mol}^{-1}$). This agrees with our results from the singly ligated sEGFR dimer MD simulation. For the case of singly ligated *Drosophila* EGFR bound to a low affinity mutant Spitz, the dimerization energy is less favorable ($\Delta\Delta G = -13.96 \text{ kcal}\cdot\text{mol}^{-1}$). This effect might be a result from structural restraints imposed by the Spitz mutant, although the binding energy for ligand in this case was $-29.06 \text{ kcal}\cdot\text{mol}^{-1}$, the lowest energy ligand-binding event in this study. It is worth noting that there is less buried surface by the mutant ($\Delta\text{ASA} = -3146.6 \text{ \AA}^2$) than both wild-type Spitz molecules ($\Delta\text{ASA} = -3796.1 \text{ \AA}^2$ & -4116.2 \AA^2).

Simulation of heterodimerization in EGFR and ErbB2

To date no structure exists of an ErbB heterodimer and little is known about the molecular mechanism of heterodimerization of ErbB receptors. We constructed a model of an EGF bound sEGFR-ErbB heterodimer for MD simulation. This was done by aligning the structure of ErbB2 to one half of the symmetric human sEGFR dimer using the dimerization arm as a reference. This heterodimer was then subjected to a 16ns simulation. After 16 ns the sEGFR-ErbB2 dimer adopted an asymmetrical dimer (Figure 7). Unlike the singly ligated sEGFR dimer, the heterodimer buried less surface at the dimer interface ($\Delta\text{ASA} = -3581.7 \text{ \AA}^2$). The energy of dimerization for a sEGFR+EGF-ErbB2 heterodimer was lower than the dimerization of a doubly- ligated sEGFR ($\Delta\Delta G = -2.02 \text{ kcal}\cdot\text{mol}^{-1}$). EGF binding to a heterodimer was only slightly more favorable, less than $1 \text{ kcal}\cdot\text{mol}^{-1}$, according to predicted

binding energies. This suggests that binding of EGF to sEGFR is not dependent on the other subunit, provided the other subunit not already occupied by a ligand.

DISCUSSION

EGFR is a member of the four structurally related receptors that are necessary for cellular development and homeostasis. The extracellular domain of EGFR (sEGFR), in the absence of an activating ligand, adopts an auto-inhibited “tethered” state. Upon binding of an active ligand sEGFR undergoes conformational rearrangements that allow it to dimerize with itself or another ErbB receptor. sEGFR is a highly dynamic protein that is thought to sample both the inhibited state and less frequently the uninhibited state without ligand binding. To explore the structural changes that occur upon EGF binding we performed 70ns MD simulations on monomeric sEGFR in the presence and absence of EGF.

The dimerization arm in domain II is thought to be involved in restraining the auto-inhibited state. Hence, EGF binding might alter the conformational sampling of the arm to break the intramolecular interactions observed in the crystal structure. Using pairwise distance measurements between the dimerization arm and the tethering arm of domain IV, we observed an EGF-dependent increase in separation over the course of a 70 ns simulation. While we noticed fluctuations in the absence of EGF, the distance at the end of the simulation had not changed relative to the starting structure. This suggests that EGF may be interacting with domain II while being bound to domain I, effectively pulling the dimerization arm away from the tether arm of domain IV. Our PCA results revealed that the correlated motion between the two arms increased when EGF is bound. While we did not observe a complete disengagement of the dimerization arm in our simulations, the increased distance of the dimerization arm relative to domain IV agrees with the model that EGF disrupts the auto-inhibited conformation, exposing the arm for dimerization. The lack of correlated motion and no net increase in distance in the absence of EGF also agree with previous results of small angle x-ray scattering studies of sEGFR [13].

Several reports have suggested that existence of high affinity and low affinity EGFR populations on a cell surface are a result of negative cooperativity. From these studies it was proposed that structural rearrangements in an EGFR dimer might give rise to nonequivalent binding sites. The structure of a homologous EGFR from *Drosophila* revealed an asymmetrical dimer where the binding one of ligand distorted the unoccupied binding pocket. This may be the case for human sEGFR, despite the apparent symmetry observed in the 2:2 EGF/sEGFR crystal structure. Using MD we simulated a 1:2 sEGFR dimer with the prediction that it would adopt an asymmetrical conformation similar to the *Drosophila* EGFR. The results of a 25 ns simulation showed that a singly ligated sEGFR adopted a different structure from the crystal structure, in agreement with the prediction.

Using PCA, we found asymmetrical motion along the dimer interface in domain II. The allosteric effect might be transferred by interactions at the interface and transmitted to the EGF binding domains I and III. This allosteric signal transmission in protein dimers along a dimer interface has also been observed in MD studies of NikR and the N-terminal domain of the AMPA receptor [35, 36]. In the case of a singly ligated sEGFR MD simulation, asymmetrical motion appeared to force domains I and III to close in a clamshell manner. This behavior has also been observed in ligated/unligated structures of the Spitz binding protein Argos [37]. In the

absence of ligand, the ligand binding domains of Argos collapse into each other. This effect was seen with domains I and III in the unligated binding pocket at 25 ns. Using distance measurements of residues between the two domains, we observed a decrease in all 3 measurements. The most dramatic decrease occurred between Y45 and F357. In the crystal structure this vector goes through the core of the EGF molecule in between the anti-parallel beta sheets. This suggests that in order for the second EGF to bind, it must pry apart domains I and III.

If there is a structural effect that decreases binding affinity, then the binding energy should also be lowered. Using our 25 ns simulation data, we calculated binding energies for the singly ligated sEGFR dimer and compared them to predicted binding energies for the crystal structures of the 2:2 EGF:sEGFR dimer and the two *Drosophila* EGFR dimers. We found that it was more energetically favorable for one EGF, or Spitz, to bind to an asymmetrical sEGFR, or *Drosophila* EGFR dimer, respectively, than to a symmetrical dimer. For the case of a 2:2 Spitz:sEGFR dimer, the binding energy of the first Spitz was lower than that of the second Spitz. This reflects a difference of binding affinity, albeit small, that may be correlated with asymmetrical conformations. A recent fluorescence resonance energy transfer study agrees with this interpretation [38].

In addition to ligand binding, we were also interested in determining the energies of symmetric and asymmetric dimerization. If dimerization of a ligated sEGFR and an unligated untethered sEGFR is more favorable than two ligated monomers, this should be reflected in differences in binding energy. sEGFR dimerization, according to our MD calculations, was more favorable when one of the sEGFR monomers was bound to EGF. A similar conclusion was reached independently, based on mutational analysis that altered the cooperativity of sEGFR (23). Artificial sEGFR heterodimer experiments may be necessary to experimentally determine the structural rearrangements associated with singly ligated sEGFR formation.

While several structures exist for EGFR homodimers, no crystal structure of an EGF heterodimer has been solved at this time. Since heterodimerization is a common feature of ErbB receptor function, understanding the molecular details would not only provide us with a better picture of how ErbB receptor activation occurs, but also a possible role of the extracellular domain in combinatorial complexity in downstream biological signals. Our MD simulation provides the first picture of a possible sEGFR-ErbB2 heterodimer structure. Using theoretical free energy calculations, we observed little energy difference between homodimerization and sEGFR-ErbB2 heterodimerization. A smaller surface area was buried between the two proteins, which might alter the intracellular kinase domains ability to recruit scaffolding proteins. Since ErbB overexpression is associated with several carcinomas, this model of sEGFR-ErbB2 heterodimerization could lead to the development of peptide or antibody inhibitors that specifically target heterodimers or block dimerization.

CONCLUSIONS

In this study we sought to map the conformational pathway of ligand dependent activation in the extracellular domain of EGFR. Using molecular dynamics simulations we observe changes in domain fluctuations upon binding of EGF to EGFR in the auto-inhibited state, particularly between the dimerization arm and domain IV. Since exposure of the dimerization arm is necessary for EGFR dimerization, the trajectory of the sEGFR with EGF may represent an intermediate state before the active conformer.

Several studies have suggested the possibility that asymmetrical dimerization may be a common feature of RTKs. To explore this hypothesis we generated two asymmetric dimers, one for a singly ligated sEGFR and EGFR-ErbB2, and performed explicit solvent calculations. PCA and binding energy calculation results suggest sEGFR dimerization is more favorable for one EGF occupied monomer and one unoccupied. These asymmetrical dynamics in sEGFR might play a role in the negative cooperative effects, in agreement with previous in-vitro binding experiments (23). Such structural transitions might have a functional role in promoting cell signalling with ErbB heterodimerization as seen in our EGFR-ErbB2 heterodimer.

Using molecular dynamics simulations to generate stable conformational states otherwise inaccessible could be used to rationally design conformation-specific antibodies for ErbB-targeted therapeutics. These results provide a glimpse at the conformational landscape of EGFR and can serve as a template for enhanced conformational sampling techniques and full length receptor models.

ACKNOWLEDGMENTS

This work was supported by USAMRMC grant W81XWH-09-1-0577. Computations were performed on the HPC Blacklight of the Pittsburgh Supercomputer Center, supported by NIH grant 5P41RR006009.

REFERENCES

1. Ferguson, K.M., Berger, M.B., Mendrola, J.M., Cho, H.S., Leahy, D.J., and Lemmon, M.A. (2003) EGF activates its receptor by removing interactions that autoinhibit ectodomain dimerization. *Mol Cell* **11**(2):507-17. PMID: 12620237.
2. Lee, J.S. and Blick, M., *Bioactive EGF peptides for promotion of tissue regeneration and cancer therapy*, U.P. 5183805, Editor. 1993, Board of Regents, University of Texas: USA.
3. Li, Z., Zhao, R., Wu, X., Sun, Y., Yao, M., Li, J., Xu, Y., and Gu, J. (2005) Identification and characterization of a novel peptide ligand of epidermal growth factor receptor for targeted delivery of therapeutics. *FASEB J* **19**(14):1978-85. PMID: 16319141.
4. Case, D.A., Cheatham, T.E., 3rd, Darden, T., Gohlke, H., Luo, R., Merz, K.M., Jr., Onufriev, A., Simmerling, C., Wang, B., and Woods, R.J. (2005) The Amber biomolecular simulation programs. *J Comput Chem* **26**(16):1668-88. PMID: 16200636.
5. Walter, T., Shattuck, D.W., Baldock, R., Bastin, M.E., Carpenter, A.E., Duce, S., Ellenberg, J., Fraser, A., Hamilton, N., Pieper, S., Ragan, M.A., Schneider, J.E., Tomancak, P., and Heriche, J.K. Visualization of image data from cells to organisms. *Nat Methods* **7**(3 Suppl):S26-41. PMID: 20195255.
6. Sanders, J.M., Wampole, M.E., Thakur, M.L., and Wickstrom, E. (2011) Molecular dynamics study of EGFR ligand-dependent activation and asymmetric dimerization. submitted. PMID.
7. Duncan, J.R. and Glaiberman, C.B. (2006) Analysis of simulated angiographic procedures: part 1--capture and presentation of audio and video recordings. *J Vasc Interv Radiol* **17**(12):1979-89. PMID: 17185697.
8. Tian, X., Aruva, M.R., Zhang, K., Cardi, C.A., Thakur, M.L., and Wickstrom, E. (2007) PET imaging of *CCND1* mRNA in human MCF7 estrogen receptor-positive breast

- cancer xenografts with an oncogene-specific [^{64}Cu]DO3A-PNA-peptide radiohybridization probe. *Journal of Nuclear Medicine* **48**(10):1699-1707. PMID: 17909257.
9. Soler, L. and Marescaux, J. (2008) Patient-specific surgical simulation. *World J Surg* **32**(2):208-12. PMID: 18066615.
 10. Citri, A. and Yarden, Y. (2006) EGF-ERBB signalling: towards the systems level. *Nat Rev Mol Cell Biol* **7**(7):505-16. PMID: 16829981.
 11. Lemmon, M.A., Bu, Z., Ladbury, J.E., Zhou, M., Pinchasi, D., Lax, I., Engelman, D.M., and Schlessinger, J. (1997) Two EGF molecules contribute additively to stabilization of the EGFR dimer. *EMBO J* **16**(2):281-94. PMID: 9029149.
 12. Ogiso, H., Ishitani, R., Nureki, O., Fukai, S., Yamanaka, M., Kim, J.H., Saito, K., Sakamoto, A., Inoue, M., Shirouzu, M., and Yokoyama, S. (2002) Crystal structure of the complex of human epidermal growth factor and receptor extracellular domains. *Cell* **110**(6):775-87. PMID: 12297050.
 13. Dawson, J.P., Bu, Z., and Lemmon, M.A. (2007) Ligand-induced structural transitions in ErbB receptor extracellular domains. *Structure* **15**(8):942-54. PMID: 17697999.
 14. Ozcan, F., Klein, P., Lemmon, M.A., Lax, I., and Schlessinger, J. (2006) On the nature of low- and high-affinity EGF receptors on living cells. *Proc Natl Acad Sci U S A* **103**(15):5735-40. PMID: 16571657.
 15. Schechter, Y., Hernaez, L., Schlessinger, J., and Cuatrecasas, P. (1979) Local aggregation of hormone-receptor complexes is required for activation by epidermal growth factor. *Nature* **278**(5707):835-8. PMID: 220539.
 16. Magun, B.E., Matrisian, L.M., and Bowden, G.T. (1980) Epidermal growth factor. Ability of tumor promoter to alter its degradation, receptor affinity and receptor number. *J Biol Chem* **255**(13):6373-81. PMID: 6967066.
 17. Cho, H.S. and Leahy, D.J. (2002) Structure of the extracellular region of HER3 reveals an interdomain tether. *Science* **297**(5585):1330-3. PMID: 12154198.
 18. Cho, H.S., Mason, K., Ramyar, K.S., Stanley, A.M., Gabelli, S.B., Denney, D.W., and Leahy, D.J. (2003) Structure of the extracellular region of HER2 alone and in complex with the Herceptin Fab. *Nature* **421**(13 Feb.):756 - 760. PMID.
 19. Bouyain, S., Longo, P.A., Li, S., Ferguson, K.M., and Leahy, D.J. (2005) The extracellular region of ErbB4 adopts a tethered conformation in the absence of ligand. *Proc Natl Acad Sci U S A* **102**(42):15024-9. PMID: 16203964.
 20. Chung, I., Akita, R., Vandlen, R., Toomre, D., Schlessinger, J., and Mellman, I. (2010) Spatial control of EGF receptor activation by reversible dimerization on living cells. *Nature* **464**(7289):783-7. PMID: 20208517.
 21. Zhang, Z. and Wriggers, W. (2011) Polymorphism of the epidermal growth factor receptor extracellular ligand binding domain: the dimer interface depends on domain stabilization. *Biochemistry* **50**(12):2144-56. PMID: 21275429.
 22. Kastner, J., Loeffler, H.H., Roberts, S.K., Martin-Fernandez, M.L., and Winn, M.D. (2009) Ectodomain orientation, conformational plasticity and oligomerization of ErbB1 receptors investigated by molecular dynamics. *J Struct Biol* **167**(2):117-28. PMID: 19406245.

23. Macdonald, J.L. and Pike, L.J. (2008) Heterogeneity in EGF-binding affinities arises from negative cooperativity in an aggregating system. *Proc Natl Acad Sci U S A* **105**(1):112-7. PMID: 18165319.
24. Alvarado, D., Klein, D.E., and Lemmon, M.A. (2010) Structural basis for negative cooperativity in growth factor binding to an EGF receptor. *Cell* **142**(4):568-79. PMID: 20723758.
25. Burgess, A.W., Cho, H.S., Eigenbrot, C., Ferguson, K.M., Garrett, T.P., Leahy, D.J., Lemmon, M.A., Sliwkowski, M.X., Ward, C.W., and Yokoyama, S. (2003) An open-and-shut case? Recent insights into the activation of EGF/ErbB receptors. *Mol Cell* **12**(3):541-52. PMID: 14527402.
26. Lill, M.A. and Danielson, M.L. (2011) Computer-aided drug design platform using PyMOL. *J Comput Aided Mol Des* **25**(1):13-9. PMID: 21053052.
27. Humphrey, W., Dalke, A., Schulten, K. (1996) VMD - Visual Molecular Dynamics. *J. Molec. Graphics* **14**:33-38. PMID.
28. D.A. Case, T.A.D., T.E. Cheatham, III, C.L. Simmerling, J. Wang, R.E. Duke, R. Luo, R.C. Walker, W. Zhang, K.M. Merz, B. Roberts, B. Wang, S. Hayik, A. Roitberg, G. Seabra, I. Kolossvai, K.F. Wong, F. Paesani, J. Vanicek, J. Liu, X. Wu, S.R. Brozell, T. Steinbrecher, H. Gohlke, Q. Cai, X. Ye, J. Wang, M.-J. Hsieh, G. Cui, D.R. Roe, D.H. Mathews, M.G. Seetin, C. Sagui, V. Babin, T. Luchko, S. Gusarov, A. Kovalenko, and P.A. Kollman (2010) Amber 11. 2010; Available from: <http://ambermd.org/>.
29. Bakan, A., Meireles, L.M., and Bahar, I. (2011) ProDy: Protein Dynamics Inferred from Theory and Experiments. *Bioinformatics* **27**(11):1575-7. PMID: 21471012.
30. Michaud-Agrawal, N., Denning, E.J., Woolf, T.B., and Beckstein, O. (2011) MDAAnalysis: A toolkit for the analysis of molecular dynamics simulations. *J Comput Chem*:Epub ahead of print. PMID: 21500218.
31. Adak, S., DeAndrade, D., and Pike, L.J. (2011) The tethering arm of the EGF receptor is required for negative cooperativity and signal transduction. *J Biol Chem* **286**(2):1545-55. PMID: 21047778.
32. Raimondi, F., Orozco, M., and Fanelli, F. (2010) Deciphering the deformation modes associated with function retention and specialization in members of the Ras superfamily. *Structure* **18**(3):402-14. PMID: 20223222.
33. Yang, L., Song, G., Carriquiry, A., and Jernigan, R.L. (2008) Close correspondence between the motions from principal component analysis of multiple HIV-1 protease structures and elastic network modes. *Structure* **16**(2):321-30. PMID: 18275822.
34. Bakan, A. and Bahar, I. (2009) The intrinsic dynamics of enzymes plays a dominant role in determining the structural changes induced upon inhibitor binding. *Proc Natl Acad Sci U S A* **106**(34):14349-54. PMID: 19706521.
35. Sukumaran, M., Rossmann, M., Shrivastava, I., Dutta, A., Bahar, I., and Greger, I.H. (2011) Dynamics and allosteric potential of the AMPA receptor N-terminal domain. *EMBO J* **30**(5):972-82. PMID: 21317871.
36. Bradley, M.J., Chivers, P.T., and Baker, N.A. (2008) Molecular dynamics simulation of the Escherichia coli NikR protein: equilibrium conformational fluctuations reveal interdomain allosteric communication pathways. *J Mol Biol* **378**(5):1155-73. PMID: 18433769.

37. Klein, D.E., Staybrook, S.E., Shi, F., Narayan, K., and Lemmon, M.A. (2008) Structural basis for EGFR ligand sequestration by Argos. *Nature* **453**(7199):1271-5. PMID: 18500331.
38. Tynan, C.J., Roberts, S.K., Rolfe, D.J., Clarke, D.T., Loeffler, H.H., Kastner, J., Winn, M.D., Parker, P.J., and Martin-Fernandez, M.L. Human epidermal growth factor receptor (EGFR) aligned on the plasma membrane adopts key features of Drosophila EGFR asymmetry. *Mol Cell Biol* **31**(11):2241-52. PMID: 21444717.
39. Roach, M., 3rd, Alberini, J.L., Pecking, A.P., Testori, A., Verrecchia, F., Soteldo, J., Ganswindt, U., Joyal, J.L., Babich, J.W., Witte, R.S., Unger, E., and Gottlieb, R. (2011) Diagnostic and therapeutic imaging for cancer: therapeutic considerations and future directions. *J Surg Oncol* **103**(6):587-601. PMID: 21480253.
40. Jadvar, H. and Fischman, A.J. (2001) Evaluation of pancreatic carcinoma with FDG PET. *Abdominal Imaging* **26**:254-259. PMID.
41. Strasberg, S.M. and Dehdashti, F. (2010) Role of FDG-PET staging in selecting the optimum patient for hepatic resection of metastatic colorectal cancer. *J Surg Oncol* **102**(8):955-9. PMID: 21165998.
42. Nguyen, N.Q. and Bartholomeusz, D.F. (2011) 18F-FDG-PET/CT in the assessment of pancreatic cancer: is the contrast or a better-designed trial needed? *J Gastroenterol Hepatol* **26**(4):613-5. PMID: 21418296.
43. Murakami, K. (2011) FDG-PET for hepatobiliary and pancreatic cancer: Advances and current limitations. *World J Clin Oncol* **2**(5):229-36. PMID: 21611100.
44. Linguraru, M.G., Sandberg, J.K., Li, Z., Shah, F., and Summers, R.M. (2010) Automated segmentation and quantification of liver and spleen from CT images using normalized probabilistic atlases and enhancement estimation. *Med Phys* **37**(2):771-83. PMID: 20229887.
45. Schwier, M., Moltz, J.H., and Peitgen, H.O. (2011) Object-based analysis of CT images for automatic detection and segmentation of hypodense liver lesions. *Int J Comput Assist Radiol Surg*. PMID: 21516506.
46. Zhang, J.Q., Sullivan, J.M.J., Yu, H., and Wu, Z., *Image Guided Multi-Modality Registration and Visualization for Breast Cancer Detection*, in *SPIE International Symposium, Medical Imaging*. 2005. p. 123-133.
47. Bueno, G., Deniz, O., Salido, J., Carrascosa, C., and Delgado, J.M. (2011) A geodesic deformable model for automatic segmentation of image sequences applied to radiation therapy. *Int J Comput Assist Radiol Surg* **6**(3):341-50. PMID: 20645131.
48. Lundström, C., Ljung, P., and Ynnerman, A. (2005) Extending and Simplifying Transfer Function Design in Medical Volume Rendering Using Local Histograms. in *IEEE/EuroGraphics Symposium Visualization*.
49. Zhou, Z.M., Fang, C.H., Huang, L.W., Zhong, S.Z., Wang, B.L., and Zhou, W.Y. (2006) Three dimensional reconstruction of the pancreas based on the virtual Chinese human--female number 1. *Postgrad Med J* **82**(968):392-6. PMID: 16754708.
50. Shimizu, A., Ohno, R., Ikegami, T., Kobatake, H., Nawano, S., and Smutek, D. (2007) Segmentation of multiple organs in non-contrast 3D abdominal CT images. *Int J Comput Assist Radiol Surg* **2**:135-142. PMID.
51. Shimizu, A., Kimoto, T., Kobatake, H., Nawano, S., and Shinozaki, K. (2009) Automated pancreas segmentation from three-dimensional contrast-enhanced computed tomography. *Int J Comput Assist Radiol Surg* **5**(1):85-98. PMID: 20033509.

52. Camara, O., Colliot, O., Delso, G., and Bloch, I. (2003) 3D nonlinear PET-CT image registration algorithm with constrained Free-Form Deformations. in *3rd IASTED International conference of Visualization, Imaging, and Image Processing*.
53. Satava, R.M. (2008) Historical review of surgical simulation--a personal perspective. *World J Surg* **32**(2):141-8. PMID: 18097716.
54. Gao, H.-J., Wu, S.-C., Bai, Y.-P., and Yang, C.-L. (2008) Three-Dimensional Visualization of Liver CT Slices by Amira. in *The 2nd International conference of Bioinformatics and Biomedical Engineering*.
55. Zhang, J.Q., Sullivan, J.M.J., Ghadyani, H., and Meyer, D.M. (2005) MRI Guided 3D Mesh Generation and registration for Biological Modeling. *Journal of Computing and Information Science in Engineering* **5**:283-290. PMID.
56. Allard, J., Cotin, S., Faure, F., Bensoussan, P.-J., Poyer, F., Duriez, C., and Delingette, H. (2007) SOFA - an Open Source Framework for Medical Simulation. in *Medicine Meets Virtual Reality (MMVR'15)*. USA.

Table 1. Predicted Binding Energies at 298 K (25°C).

Reaction	ΔE_{solv}	ΔE_{elec}	ΔH (kcal/mol)	ΔS (kcal/mol·K)	ΔASA (Å ²)	ΔG (kcal/mol)
EGF-sEGFR + EGF-sEGFR \leftrightarrow EGF ₂ -sEGFR ₂ (crystal structure)	-29949.6	117.71	21	276	-3463.8	-17.88
EGF ¹ + EGF ² -sEGFR ₂ \leftrightarrow EGF ₂ -sEGFR ₂ (crystal structure)	-23367.4	-258	23	257	-3104.1	-19.59
EGF ² + EGF ¹ -sEGFR ₂ \leftrightarrow EGF ₂ -sEGFR ₂ (crystal structure)	-25060	-229.45	22	273	-3154.2	-17.63
dEGFR-Spitz _{mutant} + dEGFR \leftrightarrow dEGFR ₂ - Spitz _{mutant} (crystal structure)	-21754.3	121.64	28	357	-3494.4	-13.96
dEGFR ₂ + Spitz _{mutant} \leftrightarrow dEGFR ₂ -Spitz _{mutant} (crystal structure)	-30125.3	-447.84	23	174	-3146.6	-29.06
Spitz ¹ + Spitz ² -dEGFR ₂ \leftrightarrow Spitz ₂ -dEGFR ₂ (crystal structure)	-38231.5	-288.12	28	280	-3796.1	-24.17
Spitz ² + Spitz ¹ -dEGFR ₂ \leftrightarrow Spitz ₂ -dEGFR ₂ (crystal structure)	-28612.5	-429.86	33	312	-4116.2	-22.37
Spitz ¹ -dEGFR ₂ + Spitz ² -dEGFR ₂ \leftrightarrow Spitz ₂ - dEGFR ₂ (crystal structure)	-23415	97.2	29	290	-3536.1	-20.41
EGF-sEGFR + sEGFR \leftrightarrow EGF-sEGFR ₂ (25 ns MD simulation)	-35491.4	-80.1	33	349	-4684.3	-20.6
EGF + sEGFR ₂ \leftrightarrow EGF-sEGFR ₂ (25 ns MD simulation)	-12029.4	-233.85	26	228	-2979.5	-23.16
EGF-sEGFR + ErbB2 \leftrightarrow EGF-sEGFR-ErbB2 (16 ns MD simulation)	-42388.2	-56.36	22	293	-3581.7	-19.9
EGF + sEGFR-ErbB2 \leftrightarrow EGF-sEGFR-ErbB2 (16 ns MD simulation)	-17163	-189.7	29	242	-3041.5	-24.37

Figure Legends

Figure 1. Structural representation of the mechanism of ligand-dependent activation and dimerization of EGFR. The extracellular domain consists of two beta-solenoid domains (red) that are responsible for EGF binding and two cysteine-rich domains. The first cysteine-rich domain (green) contains the dimerization arm necessary for dimerization and the second cysteine-rich domain (gray) is involved in coordinating the dimerization arm in the absence of ligand.

Figure 2. sEGFR intramolecular and intermolecular interactions that are involved in receptor autoinhibition and EGF binding. The dimerization arm of domain II (A) is capable of forming several noncovalent interactions with domain IV to prevent formation of stable dimers and restrict conformational sampling of sEGFR. The binding pocket of sEGFR (B) coordinates EGF (blue) with both domains I and III. Several residues are responsible for ligand coordination. Their distances are symmetric in the sEGFR dimer crystal structure.

Figure 3. Domain motions in sEGFR in the presence and absence of EGF. RMSD plots over the course of 70 ns of simulation for sEGFR+EGF (A) and sEGFR (B). Structural representation at the end of 70 ns for sEGFR+EGF (C) and sEGFR (D).

Figure 4. Binding of EGF alters the dynamics of the dimerization arm and increases coupling of motion between the dimerization and tethering arms. Correlated fluctuations of the C- α carbons of sEGFR+EGF (A) and sEGFR (B) show an increase of coupled motion between domains II and IV (black box) when EGF is bound to domain I. The color bars in A and B indicate the degree of coupling, determined by the normalized correlation coefficient. The dimerization arm became more dynamic after ligand binding (C) relative to unbound sEGFR (D). Colors in C and D represent the positions of the two arms during the course of a 70 ns simulation. Blue traces represent early positions in the simulation while red traces indicate positions at the end of the simulation.

Figure 5. A) Separation distance between the dimerization arm and the S558-S567 loop of the tethering arm of domain IV. B) Distance measurements of sEGFR (blue) and sEGFR+EGF (red) over a 70 ns simulation.

Figure 6. Asymmetrical motion in a singly ligated sEGFR dimer leads to distortion in the unoccupied binding site. Distance measurements were made for three residue pairs between domains I and III in the EGF binding pocket: Y101 to F357 (A), N12 to H346 (B) and R29 to F412 (C).

Figure 7. sEGFR can form asymmetrical homodimers and heterodimers. Structural representation of singly ligated sEGFR dimer after 25 ns of simulation (A) and an sEGFR-ErbB2 heterodimer (B) after 16 ns of simulation. Asymmetrical motion from the results of PCA for singly ligated sEGFR dimer (C) and EGFR-ErbB2 heterodimer (D). Black arrows indicate the direction of motion for the C α carbons along the first principal component.

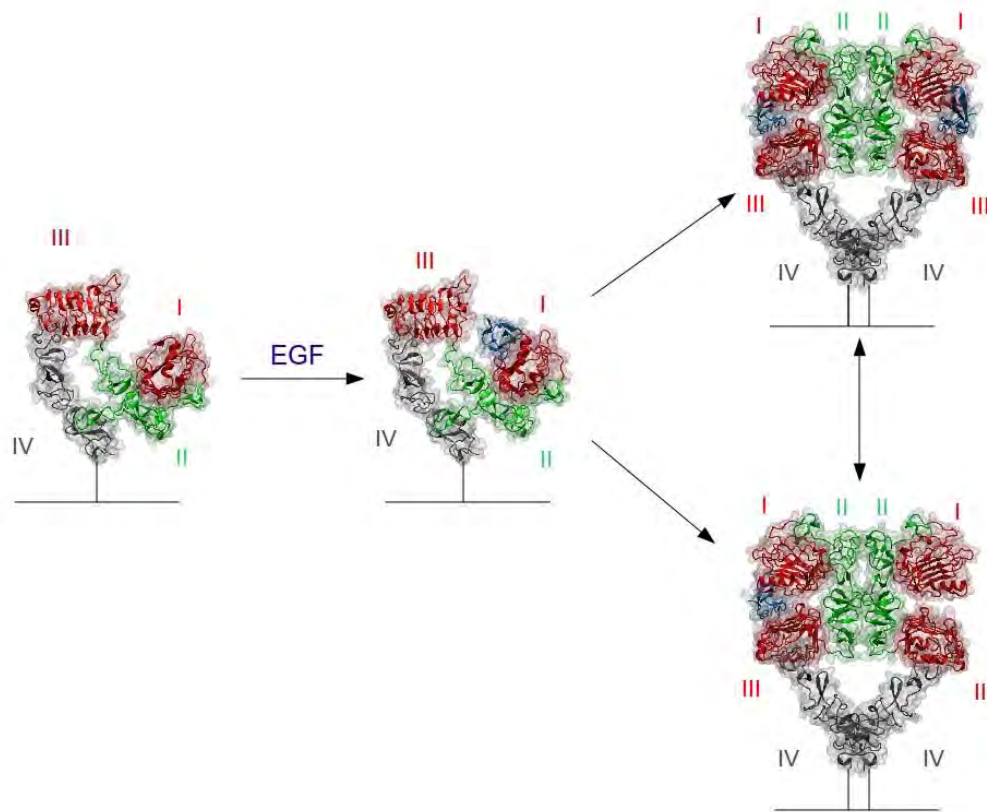


Figure 1.

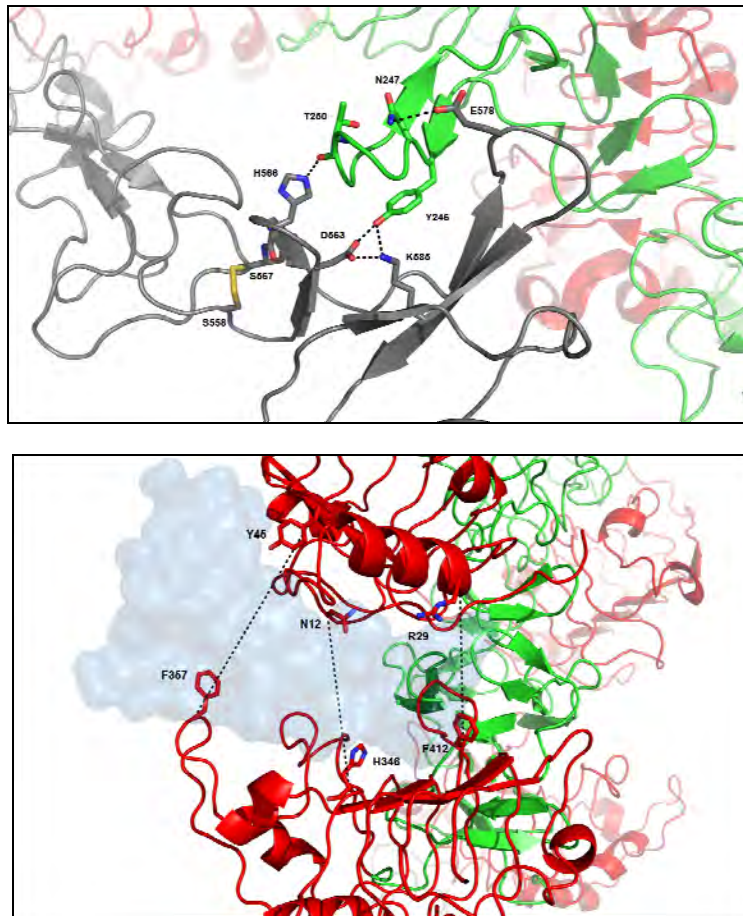


Figure 2.

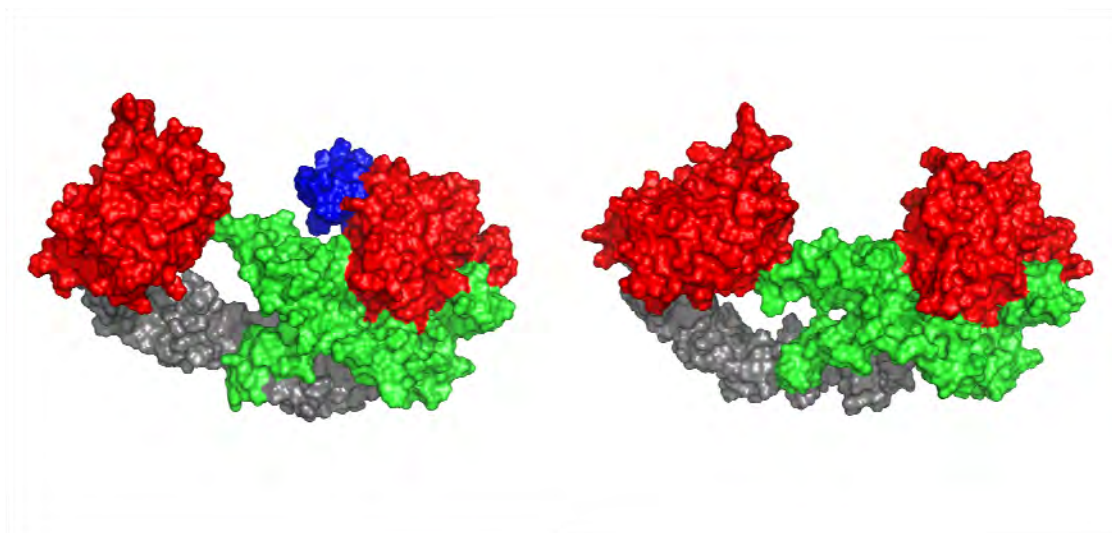
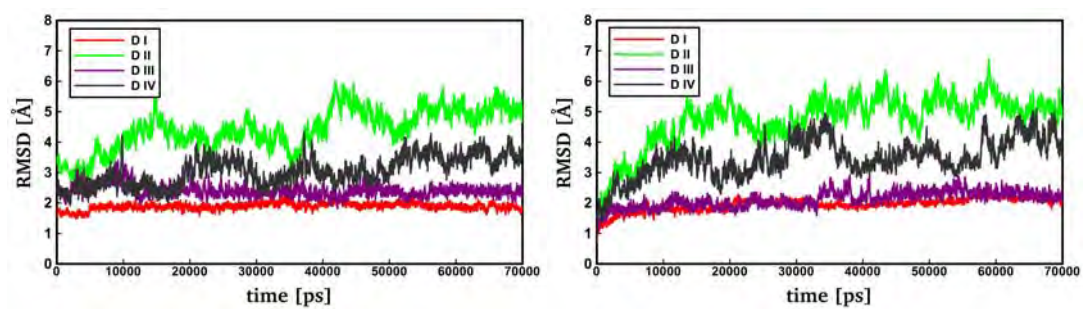


Figure 3.

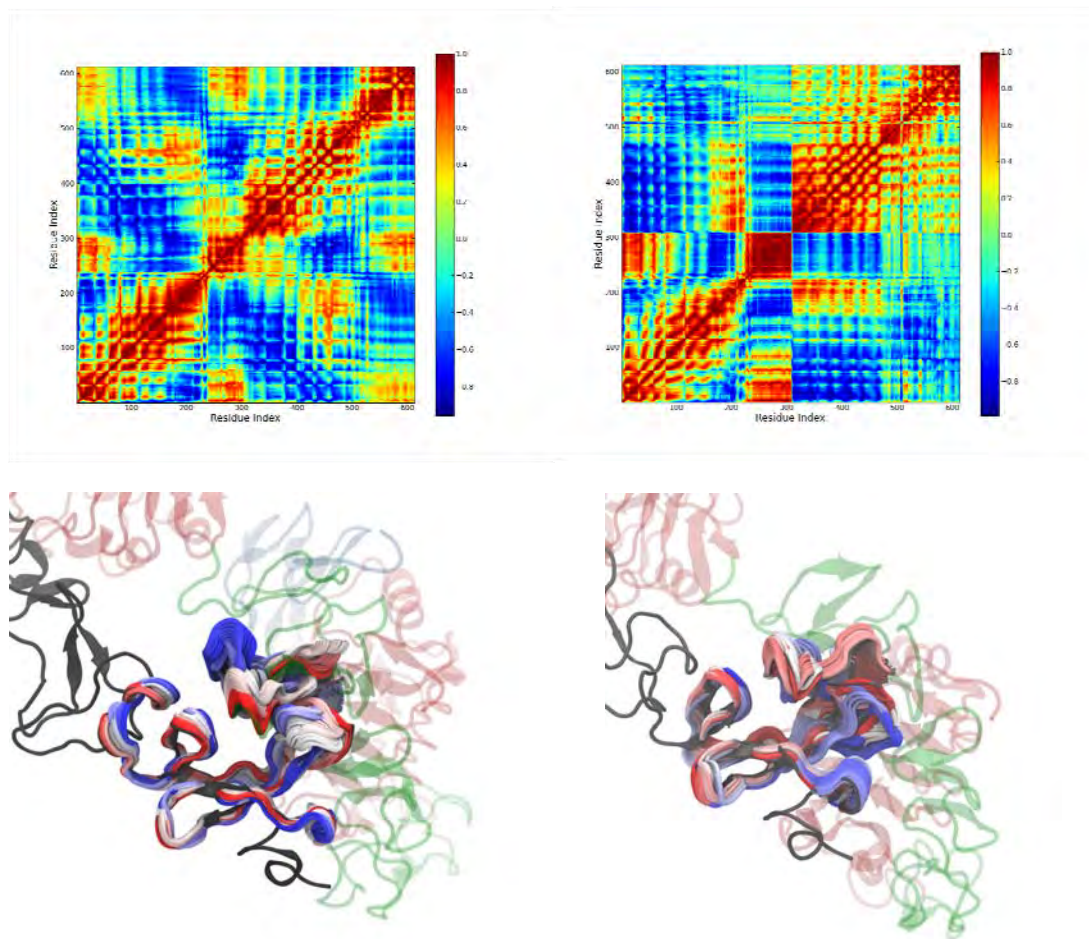


Figure 4.

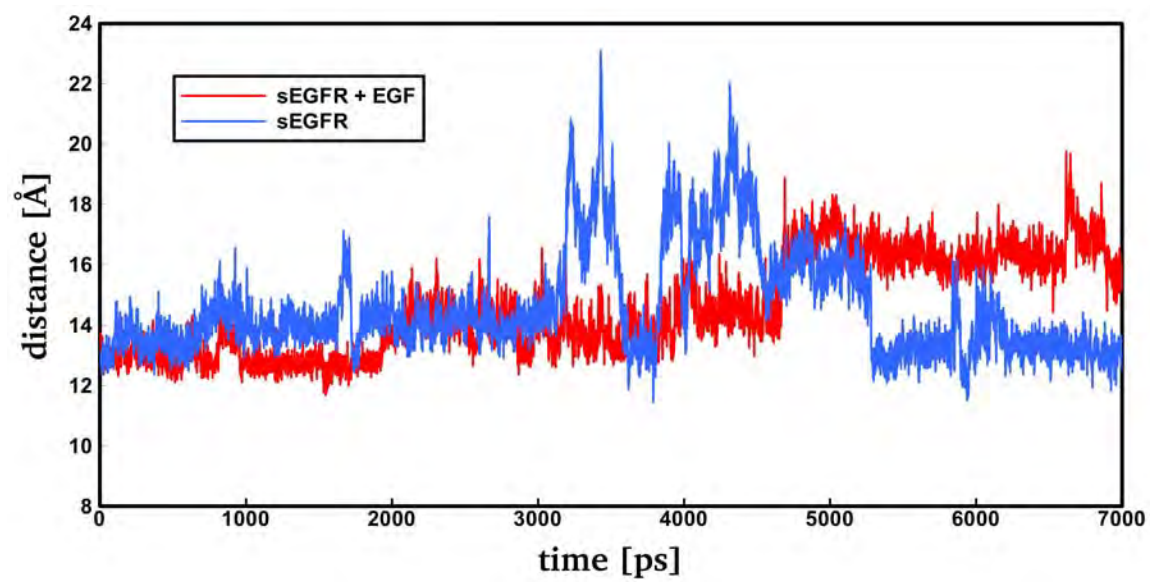
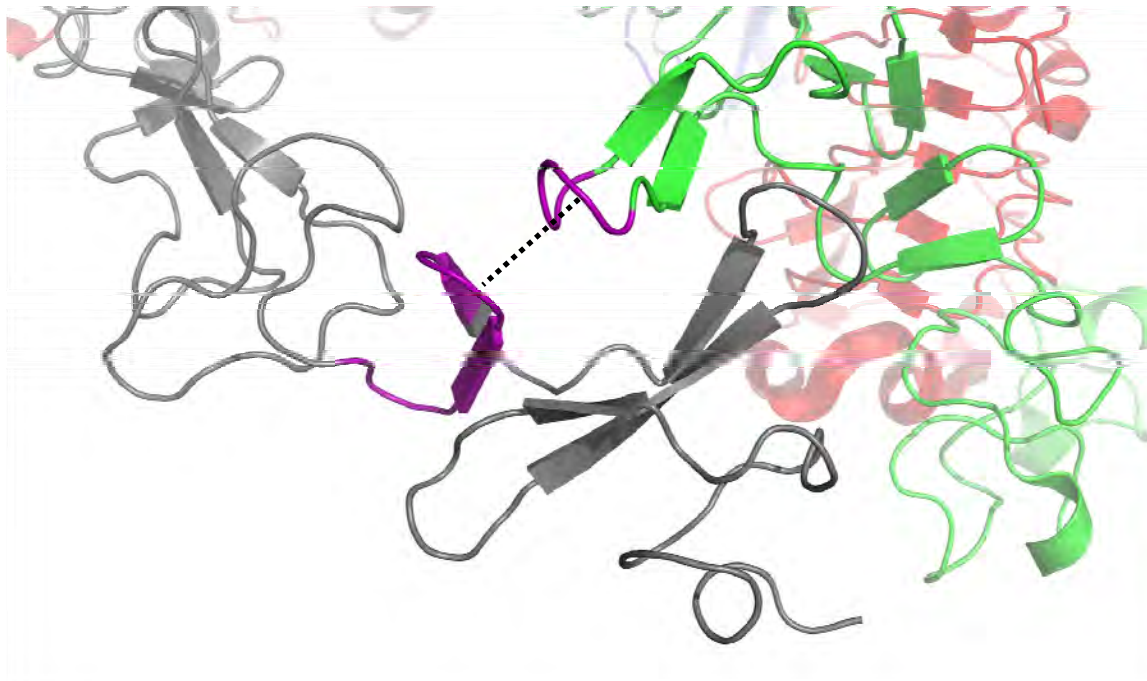


Figure 5.

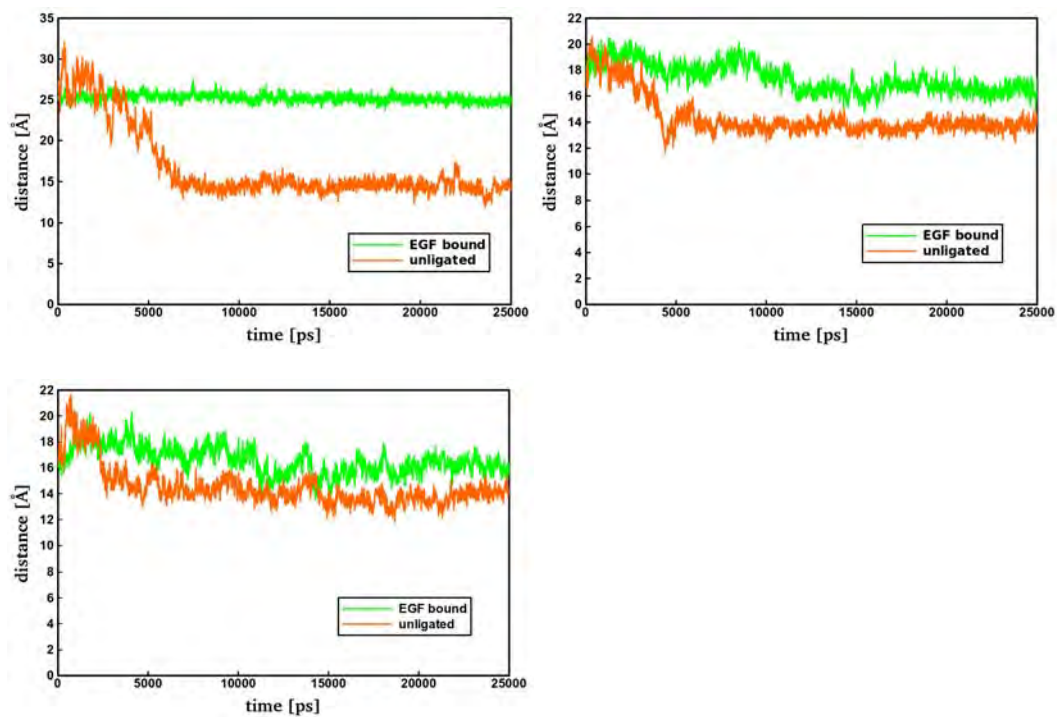


Figure 6.

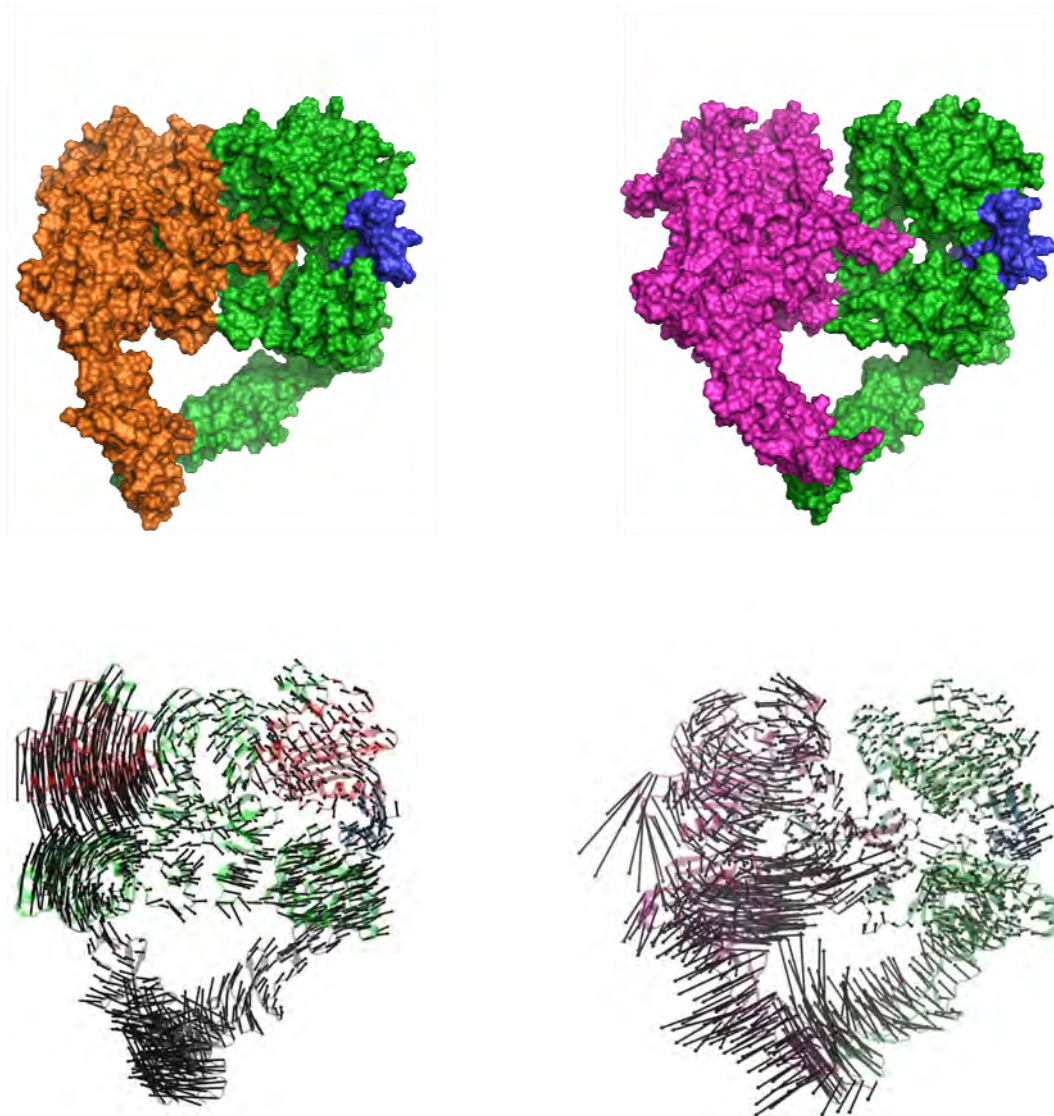


Figure 7.

Surgeon Evaluations of Three-Dimensional Renderings of PET/CT Scans of the Thorax of a Patient with a Ductal Pancreatic Mass

Matthew E. Wampole¹, John C. Kairys^{2,5}, Martha L. Ankeny³, Mathew L. Thakur^{4,5}, and Eric Wickstrom^{1,5*}

Departments of ¹Biochemistry & Molecular Biology, ²Surgery, ³Academic and Instructional Support and Resources, ⁴Radiology, and ⁵Kimmel Cancer Center
Thomas Jefferson University, Philadelphia, PA 19107

*Corresponding author. Phone: 215.955.4578, Fax: 215.955.4580. Email: eric@tesla.jci.tju.edu

Keywords: Amira, pancreas segmentation, computer-aided diagnosis, volumetric

Running Title: 3D Pancreatic Rendering

Abstract (150-250 words)

Purpose: Determine whether three-dimensional (3D) presentation of PET/CT data would benefit surgeons preparing for a procedure.

Methods: 3D rendering and co-registration of PET and CT thorax scans using Amira 5 from a patient with a ductal pancreatic mass. A group of 6 surgeons voluntarily evaluated the usefulness of each version of the presentation by answering a questionnaire.

Results: Contrast-enhanced CT fused with PET provided a more lifelike presentation than standard CT, increasing the usefulness of the presentation, according to the surgeon evaluations.

Conclusions: Volumetric simulation of a specific patient, including both CT and PET data, could be a useful practice tool for surgeons prior to making the first incision.

Introduction

Surgical evaluation of a potential pancreatectomy is a complicated task requiring 3D spatial awareness for many structures of interest (tumor, vasculature, pancreas, and spleen) and how the tumor impacts upon each. This assessment will determine whether or not a resection should be attempted. If the lesion is operable, the orientation of the pancreas and its surrounding structures will guide planning a detailed strategy for the surgical intervention. Typically the decision and planning steps are based upon two dimensional (2D) medical images of the patient from a variety of sources including computed tomography (CT), magnetic resonance imaging, ultrasound, photoacoustic imaging, positron emission tomography (PET), and other optical imaging using fluorescence[39]. Planning for this delicate operation requires surgeons to translate the 2D image slices into a 3D mental picture of the patient's anatomy, which can be a difficult task.

CT images are a widely used, non-invasive method to study internal patient structures. The 2D images produced are displayed in slices along the sagittal, axial, and coronal planes of the subject. Multiple image slices are taken of the patient and put together in their corresponding directions to form a completed image stack. The flat CT images are studied by surgeons to locate diseased structures and study their impact on surrounding tissues. This can be a difficult feat, as internal anatomy is a 3D problem. The surgeon must pan through numerous 2D images to

generate a mental 3D image of important features, such as the direction of blood vessels or how organs are positioned around each other.

With the inclusion of a positron-emitting radiolabel, specific features of interest can be observed by PET imaging. The specificity of the radiolabel is important for accurately marking a target tissue for imaging. In particular, PET imaging with 2'-[^{18}F]fluorodeoxyglucose (^{18}FDG PET) has become a useful tool in the evaluation of tumor lesions, particularly for pancreatic cancer, and the discovery of distant metastases [40-43]. ^{18}FDG is a glucose analog that is taken up aggressively by rapidly growing malignant masses, but not all hot spots are cancerous. Inflamed or infected tissues also accumulate ^{18}FDG . The kidneys filter out excess sugar from the blood, which results in strong ^{18}FDG images. Likewise the bladder also shows a strong PET image due to accumulation of ^{18}FDG waiting to be eliminated.

CT and PET are two examples of imaging methods used to diagnose and monitor cancer patients. Each has its own individual advantages and drawbacks. Most imaging techniques produce a series of image slices. Combining these 2D images into a 3D volume has the potential to aid surgeons as they evaluate patients and prepare for surgery. Transitioning from the 2D image slices to 3D volumetric surfaces requires that the images be segmented to delineate regions of interest. Segmentation is an essential part of visualizing the patient in 3D, which is typically done manually. Automating this time intensive method has been attempted for specific organs such as the liver [44, 45], breast [46], bladder, lungs[47], or blood vessels[48]. Not all targets are easily segmented through automation. The pancreas, in particular, requires some manual effort to accurately define them [49-51]. When combining multiple modalities, the images must also be registered with each other to form a simple frame of reference [52].

Taking these 2D image slices and presenting them in a 3D visualization is the first step into new methods of anatomical analysis. Simulations of biological structures are of growing interest for surgical planning, computer-aided surgery, and teaching aids [53, 54]. These simulations require accurate representation of the patient physiology and incorporation of other image sets to improve diagnostic accuracy [55]. Here we describe methods to develop a patient-specific 3D visualization from CT image slices overlaid with ^{18}FDG -PET, and independent evaluations of the usefulness of the presentation by a group of six surgeons.

Methods

Protecting patient health information

Anonymous use of CT and PET data from deceased Patient A, and questionnaires evaluating usefulness, were approved by the TJU IRB (09E.407) and the USAMRMC HRPO (A-15712.2). Files with patient data were anonymized before data manipulation began.

3D Visualizations

Visualizations of the Patient A thorax were carried out with Amira 5 (Visage Imaging, San Diego CA), a 3D visualization, analysis and modeling program that takes a modular and object-oriented approach to data visualization and analysis. The visualizations were based upon a total of three sets of data for Patient A: one non-contrast CT at 1 mm resolution, one PET image at 5 mm resolution co-registered with the non-contrast CT, and one intravenous contrast CT at 1 mm resolution.

A series of steps must be taken to transfer the image information in the 2D CT image slices into 3D volumes. Figure 1 presents a flow diagram of the steps required for translating the initial 2D images into the 3D visualization.

Two versions of the visualization were developed for subsequent evaluation by surgeons. The first version (1.2) was based solely upon the PET/CT images and had no surface refinement. The segmentation of this data set did not include a complete vascular network, but required no registration of the PET image, since they were already pre-aligned. After evaluation of the first version, the second version (1.3) was developed using the contrast CT images, which included a more complete vascular network. This version required that the PET image be aligned with the contrast CT image.

Image segmentation

Segmentation of the stack of 2D CT image slices was accomplished semi-automatically using a mixture of the Amira 5 'magic wand' tool, the 'blow tool', and manual segmentation. Segmentation of each image slice in the stack yields a matrix of points, or label field, that defines which pixels are associated with each other. The 'magic wand' tool uses a region growing function. When the user selects a voxel, an area containing that voxel and any number of other voxels whose intensities lie within the users defined ranges are selected. Lines can be drawn to limit the extent of the growth. Similarly, the 'blow tool' was another region growing method that increases as the mouse moves away from the initially clicked point. The region grows in area of similar intensities, stopping where the values change abruptly, i.e., edges.

The segmented images were then refined using the 'smooth label' and 'remove islands' options. The 'smooth label' tool uses a modified Gaussian filter to smooth the regional boundaries, removing any cusps that appear in the surface. The 'remove islands' tool finds isolated regions not connected to the larger region and removes them from the segmented label. The 'remove islands' tool can also find holes within the region and add them to the label.

Segmenting of the PET images was done with the 'magic wand' tool. The high contrast between the ^{18}F FDG uptake region of the tumor vs. the surrounding normal tissue it made it possible to choose a threshold that would pick only regions of high intensity.

Surface reconstruction

Each stack of fully segmented Patient A thoracic image slices were reconstructed into a 3D surface with an Amira 5 SurfaceGen module attached to each 2D label field. The SurfaceGen module computes a triangular approximation of the surface from the 2D label fields and the interfaces between differing regions. These base 3D visuals have a large number of triangles and can appear rather rough. One example would be the liver consisting of 129,325 points and 258,622 triangles. The entire rendering of the patient had 1,216,386 triangles over 12 models: skeleton, liver, intestines, duodenum, right kidney, left kidney, stomach, spleen, pancreas, adrenal glands, veins, and arteries. As an initial step in smoothing the visuals, the 'smoothing' option of the SurfaceGen module was set to unconstrained smoothing and the SmoothKernelSize variable was set to 3.

Surface quality and refinement

The Amira 5 Simplification editor was applied to the thoracic base 3D visuals to improve the quality and reduce the number of triangles forming the visuals. The Simplification editor uses an edge collapsing algorithm to reduce edges of the surface to points, while preserving the original shape of the surface by minimizing the error criterion. The 3D surfaces were then re-meshed to improve their appearance using the RemeshSurface module. For remeshing, an isotropic vertex placement and a 50% reduction in the number of triangles was used to achieve a higher triangle quality and modest reduction in the number of triangles. At this point the liver was simplified to 9002 points and 18000 triangles before being remeshed to 4501 points and

8998 triangles. In version 1.3, the entire rendering contained 225,221 triangles with the same number of organs being represented.

Registration

Registration of multiple images is necessary for studies of a subject over time, when comparing different modalities, matching an image volume with its model, and aligning a template with the patient's image. Aligning multiple images correctly is a difficult task due to organ motion during respiration, patient re-positioning, organ changes over time due to disease, deformation of target organs, and many more. Automated registration exists for certain applications, such as the lung or arteries, but is not amenable for use with the pancreas, due to similar intensities in the voxels between the pancreas and neighboring organs.

A hybrid of automated and interactive registration was used with the PET/CT, CT-only, and contrast CT data sets. The focus of the registration was to align the PET images of the pancreas so that they could be overlaid with the contrast CT model. The CT without contrast, which was initially aligned with the PET images, was aligned to the contrast CT before applying the transformation to the PET images. Both the CT data and the 3D renderings were used for the registration.

Initially, automated registration with the AffineRegistration module aligned the images roughly. The AffineRegistration module uses the mean squared differences between gray values of the model and reference as the metric for alignment and scaling, prior to further refinement. Interactive registration was then carried out to refine the alignment and scale of the images. Amira 5 provides 9-parameters with which to adjust the image transformation; translation, rotation axis, and scale factor.

The final stage of registration of the 3D surfaces of the pancreas utilized the AlignSurface module. This module has three strategies for aligning the surface, using the surface points, the center of mass, or the principal axes of the inertia tensor. Three types of transformation can be specified: rigid alignment, rigid alignment with uniform scaling, or a flexible affine transformation. We used the surface points with a rigid alignment to align the pancreas of the non-contrast CT with that of the contrast CT.

Once the two renderings were aligned with each other, the transformation could be applied to the PET images. Since the PET images were initially aligned with those of the non-contrast CT, the transformations applied to the CT images were repeated with the PET images.

Evaluations

Six surgeons from Thomas Jefferson University Hospital volunteered to evaluate both versions of the Patient A thoracic visualization. These surgeons varied from general surgery to thoracic surgery. The surgeons were shown how to manipulate the image, especially how to strip off overlaying tissues and organs overlaying the pancreas.

The evaluation consisted of multiple questions using a scale from 1 to 5: 1 = strongly disagree, 2 = disagree, 3 = neither agree/disagree, 4 = agree, and 5 = strongly agree. Blank space was also provided for each surgeon to leave comments on the visual appearance and usefulness of the presentation, plus any overall comments.

The evaluation and questionnaire were done in the presence of the interviewer to help answer any questions about the visuals, manipulating Amira 5, or the questionnaire. This mode facilitated the surgeons' usage of Amira 5, independent of any prior knowledge of the program, and yielded a more reliable evaluation of the system.

Results

Evaluation was carried out to gather information on what aspects and features of the thoracic visualizations the surgeons found useful. Snapshots from version 1.2 are shown in Figures 2 and 3, while snapshots from version 1.3 appear in Figures 4 and 5. There was an overall improvement in the ratings of the visualizations going from version 1.2 to 1.3.

An example of the ^{18}F FDG -PET overlay is given in Figure 6. Because of the lower resolution in the PET images (5 mm), parts of the surface representation of the tumor formed from the PET data do not exactly replicate the contours of the pancreas.

Figures 7 presents the average scores from the surgeon evaluations for each of the 15 questions asked for versions 1.2 and 1.3. Averaging surgeon responses to the 15 questions, version 1.2 scored 3.6 ± 0.5 , while version 1.3 received a score of 4.4 ± 0.4 . The overall averages of the questionnaire illustrate greater appreciation of version 1.3, while the standard deviations reveal greater consensus in evaluating version 1.3. A paired-samples t-test was done to compare the average of the scores given to each question in version 1.2 and version 1.3. There was a statistically significant difference in these scores for version 1.2 ($M = 3.6$, $SD = 0.5$) and version 1.3 ($M = 4.4$, $SD = 0.4$); $t(14) = -7.056$, $p < 0.001$. Our results show that the improvements of version 1.3 had a positive impact on the scoring of the visualizations.

In both versions, the surgeons found the hardware and image manipulation/re-positioning easy to use. Hardware was assigned an average score of 4.5 ± 0.6 for both versions. Image manipulation scores increased from 4.2 ± 1.0 for version 1.2 to 4.5 ± 0.6 for version 1.3.

The accuracy of the segmentations, their rendering, and the surgeons' satisfaction with the level of detail all improved going from version 1.2 to 1.3. For version 1.2, 4 out of 6 surgeons agreed with the accuracy of the segmented images, with one neither agreeing nor disagreeing, and one strongly disagreeing, for an average score of 3.7 ± 1.5 . The colors and textures used were quite similar with 4 of 6 agreeing, one neither agreeing nor disagreeing, and one disagreeing, for an average score of 3.8 ± 1.2 . The average score for the level of detail was 3.2 ± 1.5 with only half the surgeons being satisfied with it, one neither agreeing nor disagreeing, one disagreeing, and the last strongly disagreeing.

Version 1.3, on the other hand, received scores of 4.5 ± 0.8 , 4.7 ± 0.8 and 4.0 ± 1.1 for the segmentation, rendering, and level of detail. Only one surgeon couldn't agree or disagree with the segmentations and rendering, but disagreed with the level of detail.

Overall the surgeons assigned version 1.2 a score of 3.5 ± 1.2 for the model providing adequate reference to surrounding structures, and a score of 3.5 ± 1.2 For how well it matches expectations in the OR while version 1.3 faired much better with a score of 4.7 ± 0.5 and 4.0 ± 1.1 respectively.

While viewing only the 3D CT renderings of the Patient A thorax, the surgeons were asked to rate their understanding of the tumor with its surrounding organs and if this view would change how they might plan to approach this tumor. Version 1.2 scored an average of 3.8 ± 1.2 on understanding of the tumor and its surroundings, but a 2.7 ± 1.0 on changing how they might plan to approach it. For version 1.3, however, average scores of 4.3 ± 0.8 and 3.8 ± 0.8 were given for understanding of the tumor with its surrounding organs, and if this view would change how they might plan to approach this tumor, respectively.

Viewing the 3D CT renderings with the PET overlay was rated similarly to those without the overlay for understanding of the tumor with its surrounding organs, and if this view would change how they might plan to approach this tumor. Version 1.2 received scores of 3.3 ± 1.0 and 2.7 ± 1.2 for understanding and approach, while version 1.3 was scored at 4.2 ± 0.8 and 3.6 ± 0.9 .

Four questions were asked on the usefulness of the visualizations. The first question asked if the surgeon would want to use this 3D image to plan an operation for a patient with this specific tumor. The surgeons scored version 1.2 at 3.7 ± 1.8 , and version 1.3 at 4.8 ± 0.4 . In the second question, the surgeons were asked if they would want to use these images with the PET overlay to plan an operation for a patient with this specific tumor. They scored version 1.2 at 3.7 ± 1.8 , and version 1.3 at 4.3 ± 1.2 . Next, the surgeons were asked if they would like a system such as this available in the OR for reference during an actual operation. Few agreed with version 1.2, giving it a score of 3.5 ± 1.6 , but for version 1.3 most strongly agreed, yielding an average of 4.7 ± 0.5 . The final question asked if this system would help residents/assistants better prepare for the operation. In both versions the surgeons agreed, giving version 1.2 a score of 4.0 ± 1.6 and version 1.3 a score of 4.8 ± 0.4 .

Each surgeon was given space on each questionnaire to leave comments on how the visual models could be improved and what would make the models more useful. In version 1.2 every surgeon who commented asked for a more detailed inclusion of the vascular system. A few left suggestions for more textures and detail in the models. With version 1.3, an appreciation for the inclusion of the vascular system was seen in many of the comments. Some asked for improvements in the fine details of the tumor and blood vessels. In this version the blood vessels were given slightly different hues to help differentiate the branches. One surgeon proposed making all the vessels one color, while another wanted to be able to remove specific vessels as desired. One other comment mentioned that determining tumor invasion of adjacent structures was difficult to determine.

Discussion

The evaluations of the two visualization versions were positive overall, but the improvements in version 1.3 yielded much better scores from the surgeons. Changes from version 1.2 to 1.3 included a more detailed vascular system using the contrast enhanced CT images and reduction of the triangle counts in the models to accelerate computer performance. Color-coded distributions of the scores assigned by the surgeons to each question for version 1.2 and 1.3 are shown in Figures 8 and 9.

In version 1.2, a broad spread of opinions was displayed in the surgeon responses. Over all the questions, 60% of the surgeons agreed or strongly agreed while 26% disagreed or strongly disagreed. 14% of the questions received neither agreement nor disagreement.

Of all the questions, only the ease and comfort of use for the display hardware received unanimous agreement with three agreeing and three agreeing strongly. Most found the images easy to manipulate or reposition, scored at 4.2 ± 1.0 , with three strongly agreeing, one agreeing, and two having neither agreeing or disagreeing. Four surgeons felt strongly that this version would be helpful for residents and assistants to better prepare for the operation with two disagreeing, with an overall score of 4.0 ± 1.6 .

The two questions on viewing the 3D models with and without the PET data generated broad disagreement, with an average score of 2.7 ± 1.21 and 2.7 ± 1.03 respectively. Looking over the comments, a clear desire from the surgeons was to have more detail included in the models. In particular they wanted to see the vascular structures around the tumor.

The majority of scores for version 1.2 ranged from 3.8 to 3.2, with usually four of the six surgeons agreeing with the question. The highest scored questions in version 1.2 concerned the color and textures used for the models as well as whether viewing the 3D model produced better understanding of the tumor and its surroundings. On the other hand, getting a better

understanding of the tumor and its surroundings by overlapping the 3D models with the PET image received only a score of 3.3 ± 1.0 . The surgeons were also not satisfied with the level of detail that was presented in version 1.2, giving it a score of 3.2 ± 1.5 .

Scores for version 1.3 showed a vast improvement in the surgeons' opinions of the visualization. Over all the questions, the surgeons agreed or strongly agreed with 85%, neither agreed nor disagreed with 10%, disagreed with 3%, and left no comment with 2%.

Many of the questions received unanimous agreement from the surgeons. Two received a high agreement score of 4.8. Five out of six surgeons strongly agreed that they would want to use this 3D image to plan an operation for a patient with this specific tumor. Similarly, they felt strongly that this system would help residents and assistants better prepare for the operation.

Only two questions in version 1.3 received an average score below 4.0. Whether viewing the 3D CT models alone changed how they would plan to approach the tumor received a score of 3.8 ± 0.8 , while including the PET data received a score of 3.6 ± 0.9 . This is an improvement over the scores from version 1.2, demonstrating that inclusion of the vascular systems is important for planning, but also indicating that further improvements are needed for the 3D models to be most useful. For the whole of version 1.3, only three times did a question receive a disagreeing score and none strongly disagreed. These three included being satisfied with the level of detail, the overall 3D image appearing realistic, and if the surgeon would want to use this system with PET overlay to plan an operation for a patient with this specific tumor. This is a marked improvement over the total of 22 disagrees and strongly disagrees from version 1.2.

The rest of the questions in version 1.3 received an average score ranging from 4.7 to 4.0. Three received scores of 4.7, including the color and textures of the models, models providing adequate reference to surrounding structures, and the surgeons desire to have this system available in the OR for reference during an actual operation.

Three questions displayed large improvement, increasing by 1.2, with the upgrades in the model from version 1.2 to 1.3. Inclusion of the vascular system provided the needed references to structures surrounding the tumor. That upgrade also markedly improved how just by viewing the 3D model their plan of approaching this tumor would change. The improvements also made this model attractive for planning an operation on a patient with this specific tumor.

The changes made between the two versions raised the surgeons' opinions of the models, but further improvements are needed. In particular, even with the vascular system included in the visualization, the surgeons saw only modest benefit for planning how to approach the pancreatic tumor. One idea, suggested by a surgeon, would be to include visual warnings for adjacent structures that are close to the tumor. This could draw the surgeon's attention to structures, such as blood vessels, near the tumor that could be of concern for unintended cutting. Another suggestion was to have the color of the vascular system be dependent on the theoretical oxygenation level in the blood.

Conclusions

This work describes a method for rendering individual patient data as 3D surfaces and for surgeon evaluation of the usefulness of the resulting visualization. Regular CT and contrast CT images were both used to generate the surface meshes. Inclusion of PET images clearly defined what regions of the model contained aggressive tumor cells. The evaluating surgeons found these

visualizations to be useful tools for planning an operation, as a reference in the operating room during surgery, and as a reference for residents and assistants.

The next step in the development of this visualization system is to transfer the 3D models to the Simulation Open Framework Architecture (SOFA)[56]. By integrating a physical response model with the visualization, the surgeons will be able to interact directly with the models. A haptic interface will also be introduced to provide tactile feedback to the surgeons so that they can practice palpation of the tumor region before ever having to make an incision. A touch-and-feel simulation of a specific patient could be a useful practice tool for surgeons prior to making the first incision, and could be a useful tool for teaching medical students and residents important skills.

Acknowledgments

This work was supported by USAMRMC/TATRC grant W81XWH-09-1-0577 to E.W.

References

1. Roach M, 3rd, Alberini JL, Pecking AP, Testori A, Verrecchia F, Soteldo J, Ganswindt U, Joyal JL, Babich JW, Witte RS, Unger E, Gottlieb R (2011) Diagnostic and therapeutic imaging for cancer: therapeutic considerations and future directions. *J Surg Oncol* 103 (6):587-601. doi:10.1002/jso.21805
2. Jadvar H, Fischman AJ (2001) Evaluation of pancreatic carcinoma with FDG PET. *Abdominal Imaging* 26:254-259
3. Strasberg SM, Dehdashti F (2010) Role of FDG-PET staging in selecting the optimum patient for hepatic resection of metastatic colorectal cancer. *J Surg Oncol* 102 (8):955-959. doi:10.1002/jso.21729
4. Nguyen NQ, Bartholomeusz DF (2011) 18F-FDG-PET/CT in the assessment of pancreatic cancer: is the contrast or a better-designed trial needed? *J Gastroenterol Hepatol* 26 (4):613-615. doi:10.1111/j.1440-1746.2011.06625.x
5. Murakami K (2011) FDG-PET for hepatobiliary and pancreatic cancer: Advances and current limitations. *World J Clin Oncol* 2 (5):229-236. doi:10.5306/wjco.v2.i5.229
6. Linguraru MG, Sandberg JK, Li Z, Shah F, Summers RM (2010) Automated segmentation and quantification of liver and spleen from CT images using normalized probabilistic atlases and enhancement estimation. *Med Phys* 37 (2):771-783
7. Schwier M, Moltz JH, Peitgen HO (2011) Object-based analysis of CT images for automatic detection and segmentation of hypodense liver lesions. *Int J Comput Assist Radiol Surg*. doi:10.1007/s11548-011-0562-8
8. Zhang JQ, Sullivan MJ, Yu H, Wu Z (2005) Image Guided Multi-Modality Registration and Visualization for Breast Cancer Detection. Paper presented at the SPIE International Symposium, Medical Imaging,
9. Bueno G, Deniz O, Salido J, Carrascosa C, Delgado JM (2011) A geodesic deformable model for automatic segmentation of image sequences applied to radiation therapy. *Int J Comput Assist Radiol Surg* 6 (3):341-350. doi:10.1007/s11548-010-0513-9
10. Lundström C, Ljung P, Ynnerman A Extending and Simplifying Transfer Function Design in Medical Volume Rendering Using Local Histograms. In: *IEEE/EuroGraphics Symposium Visualization*, 2005. pp 263-270

11. Zhou ZM, Fang CH, Huang LW, Zhong SZ, Wang BL, Zhou WY (2006) Three dimensional reconstruction of the pancreas based on the virtual Chinese human--female number 1. *Postgrad Med J* 82 (968):392-396. doi:82/968/392 [pii] 10.1136/pgmj.2005.039230
12. Shimizu A, Ohno R, Ikegami T, Kobatake H, Nawano S, Smutek D (2007) Segmentation of multiple organs in non-contrast 3D abdominal CT images. *Int J Comput Assist Radiol Surg* 2:135-142
13. Shimizu A, Kimoto T, Kobatake H, Nawano S, Shinozaki K (2009) Automated pancreas segmentation from three-dimensional contrast-enhanced computed tomography. *Int J Comput Assist Radiol Surg* 5 (1):85-98. doi:10.1007/s11548-009-0384-0
14. Camara O, Colliot O, Delso G, Bloch I 3D nonlinear PET-CT image registration algorithm with constrained Free-Form Deformations. In: 3rd IASTED International conference of Visualization, Imaging, and Image Processing, 2003. pp 516-521
15. Satava RM (2008) Historical review of surgical simulation--a personal perspective. *World J Surg* 32 (2):141-148. doi:10.1007/s00268-007-9374-y
16. Gao H-J, Wu S-C, Bai Y-P, Yang C-L Three-Dimensional Visualization of Liver CT Slices by Amira. In: The 2nd International conference of Bioinformatics and Biomedical Engineering, 2008. pp 16-18
17. Zhang JQ, Sullivan JMJ, Ghadyani H, Meyer DM (2005) MRI Guided 3D Mesh Generation and registration for Biological Modeling. *Journal of Computing and Information Science in Engineering* 5:283-290
18. Allard J, Cotin S, Faure F, Bensoussan P-J, Poyer F, Duriez C, Delingette H SOFA - an Open Source Framework for Medical Simulation. In: Medicine Meets Virtual Reality (MMVR'15), USA, 2007. pp 13-18

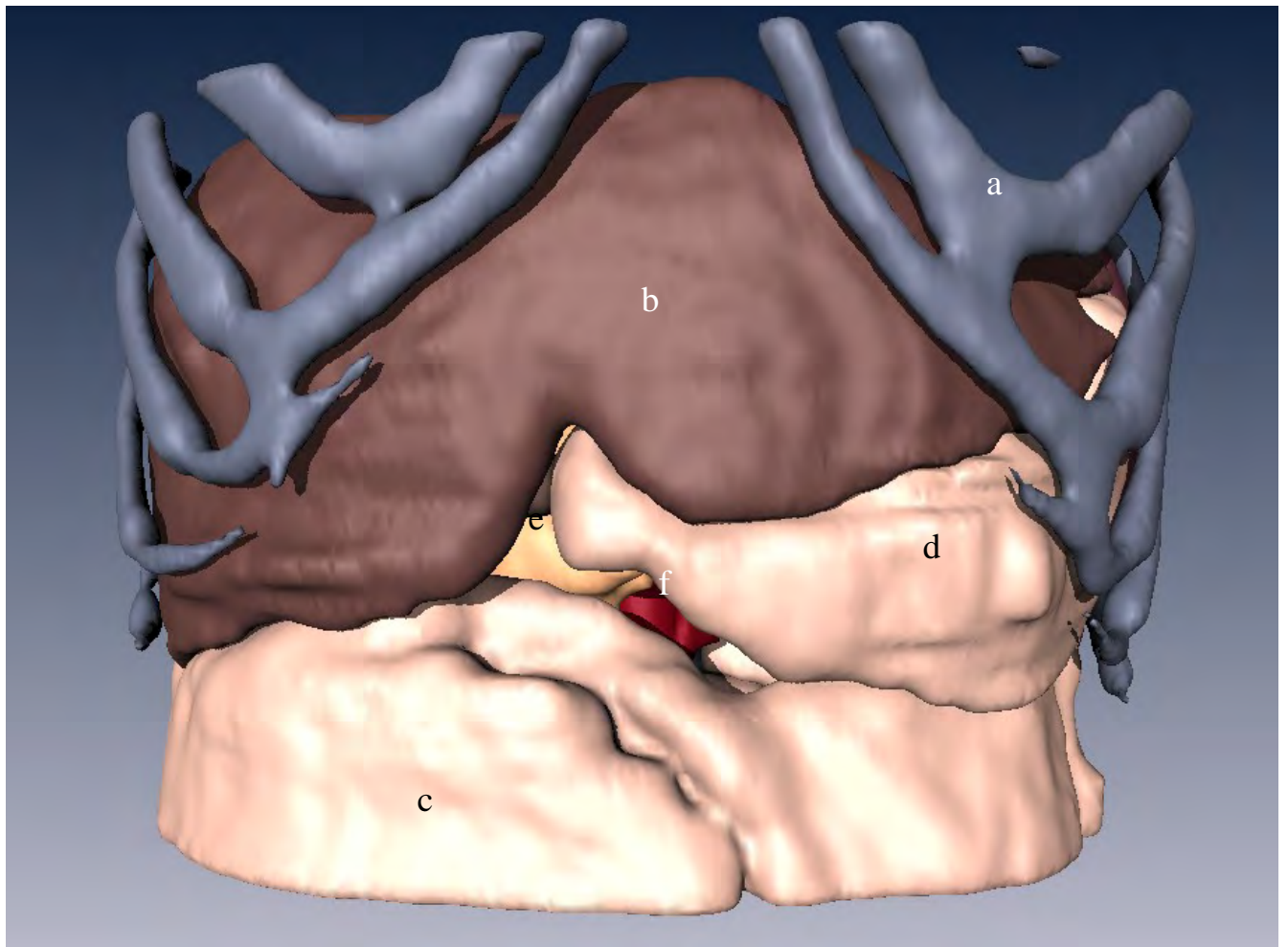
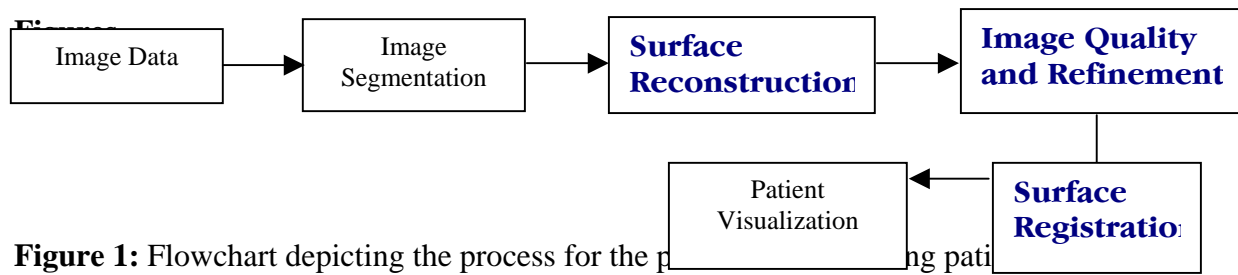


Figure 2: Volumetric rendering of Patient A in version 1.2. Anatomy displayed in this rendering are a) skeleton, b) liver, c) intestines, d) stomach, e) pancreas, and f) aorta.

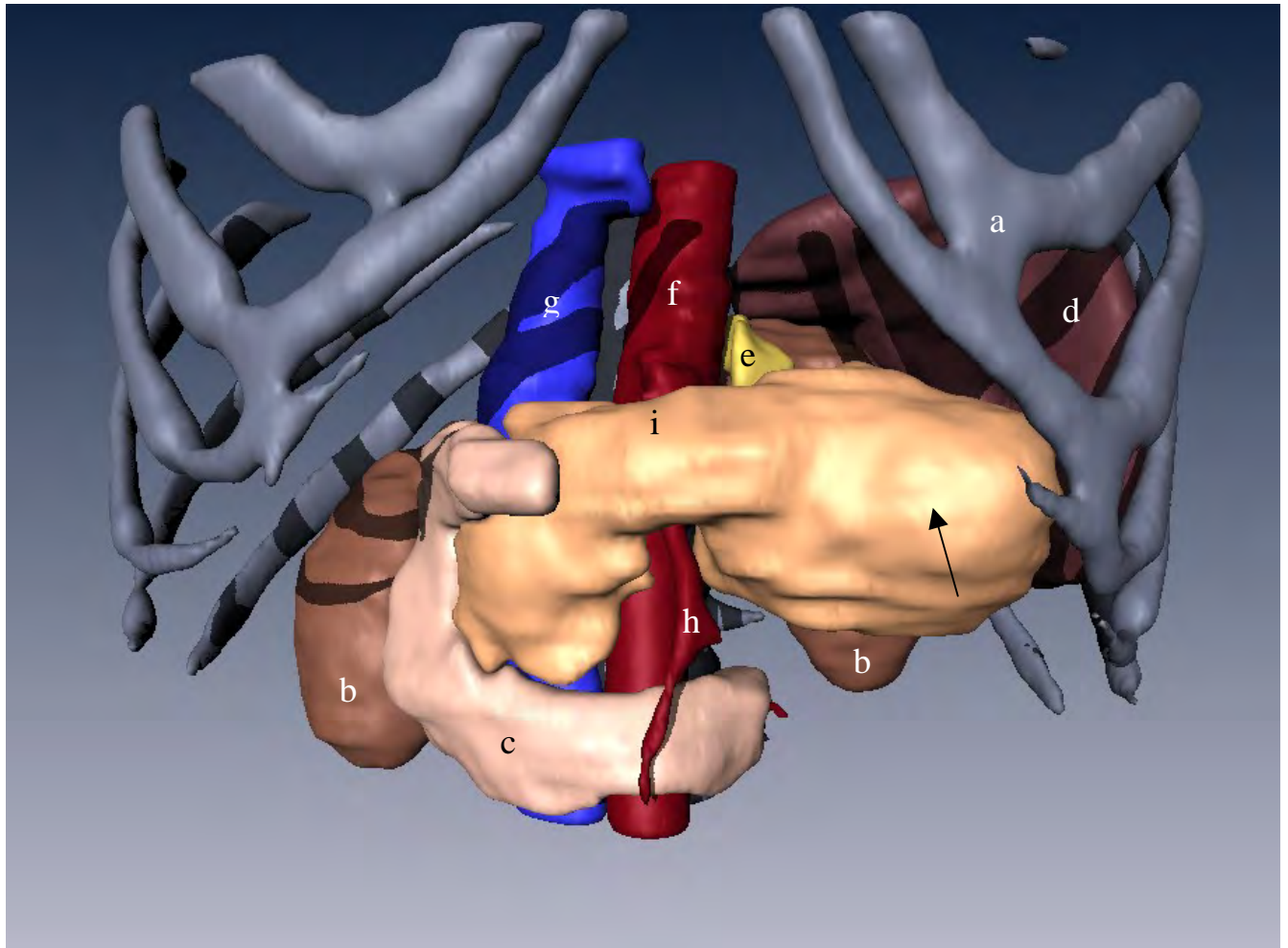


Figure 3: Visualization 1.2 with some organs stripped away to more fully display the pancreatic tumor (black arrow). Organs displayed in this rendering are **a)** skeleton, **b)** kidneys, **c)** duodenum, **d)** spleen, **e)** adrenal gland, **f)** aorta, **g)** vena cava, **h)** superior mesenteric artery, and **i)** pancreas.

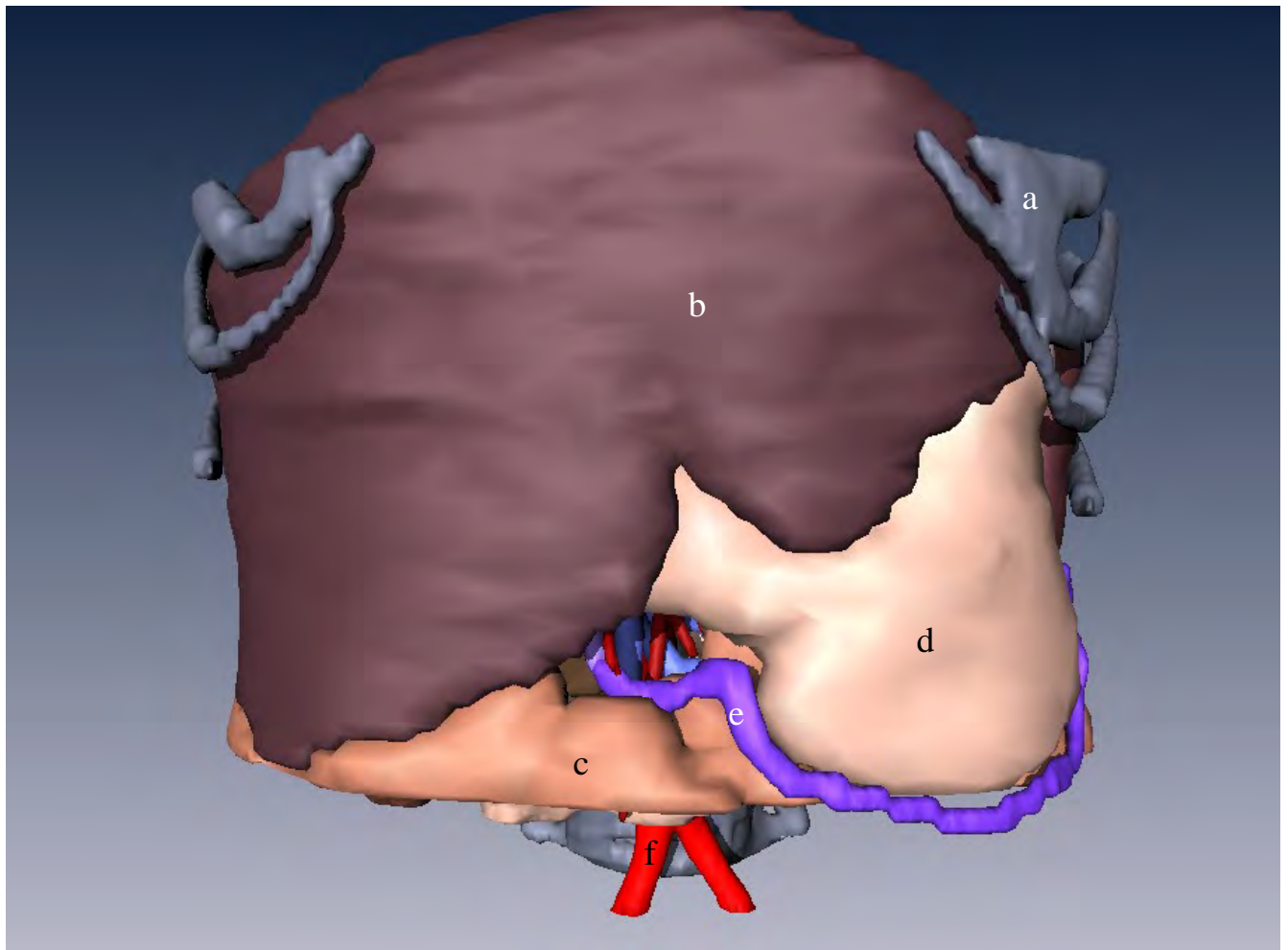


Figure 4: Volumetric rendering of Patient A in version 1.3. Anatomy displayed in this rendering are **a)** skeleton, **b)** liver, **c)** intestines, **d)** stomach, **e)** right gastroepiploic vein, and **f)** common iliac artery.

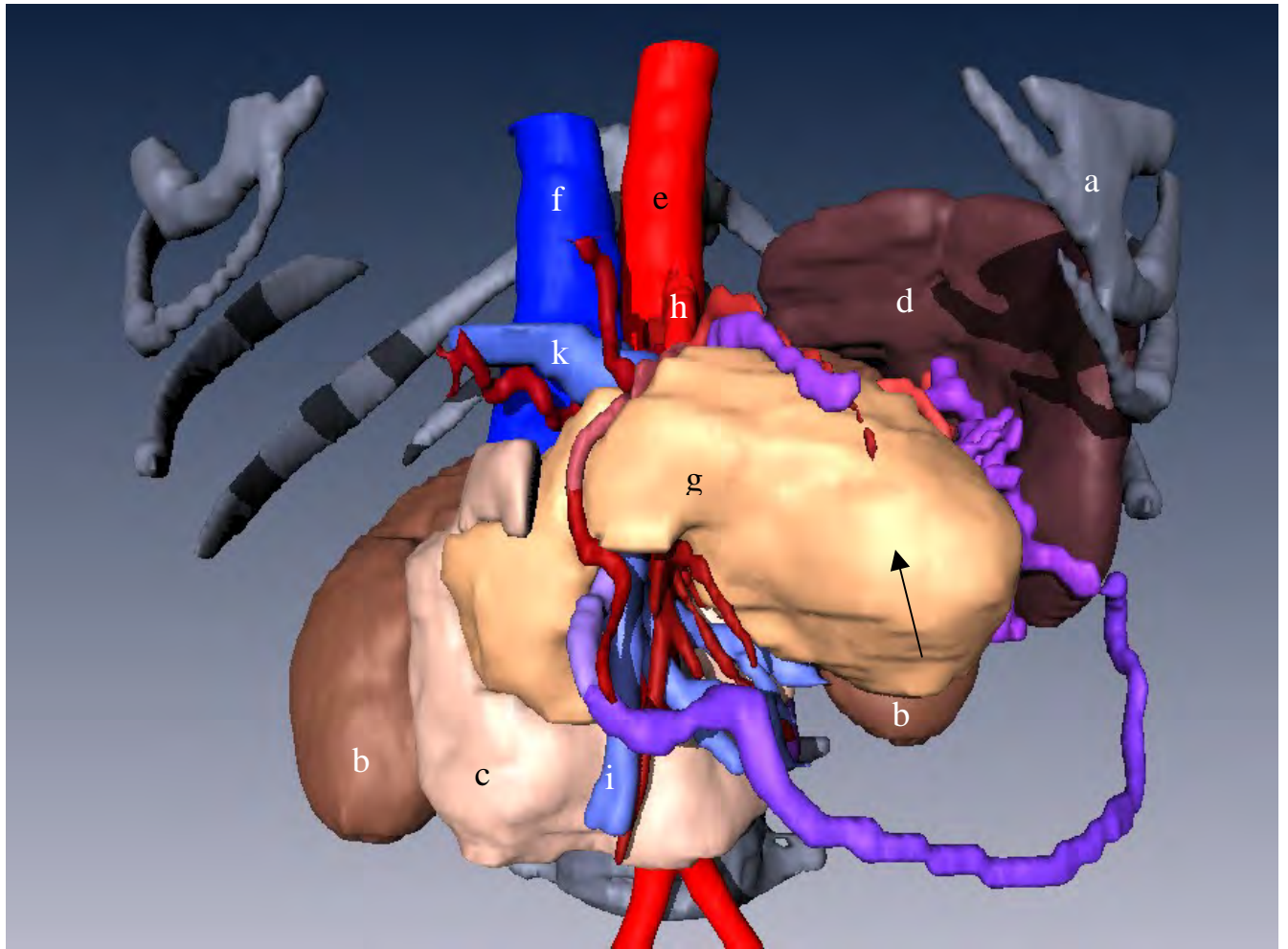


Figure 5: Visualization 1.3 with some organs stripped away to more fully display the pancreatic tumor (black arrow). Organs displayed in this rendering are **a)** skeleton, **b)** kidneys, **c)** duodenum, **d)** spleen, **e)** aorta, **f)** vena cava, **g)** pancreas **h)** superior mesenteric artery, **i)** superior mesenteric vein, **j)** right gastroepiploic vein, **k)** portal vein, and other blood vessels.

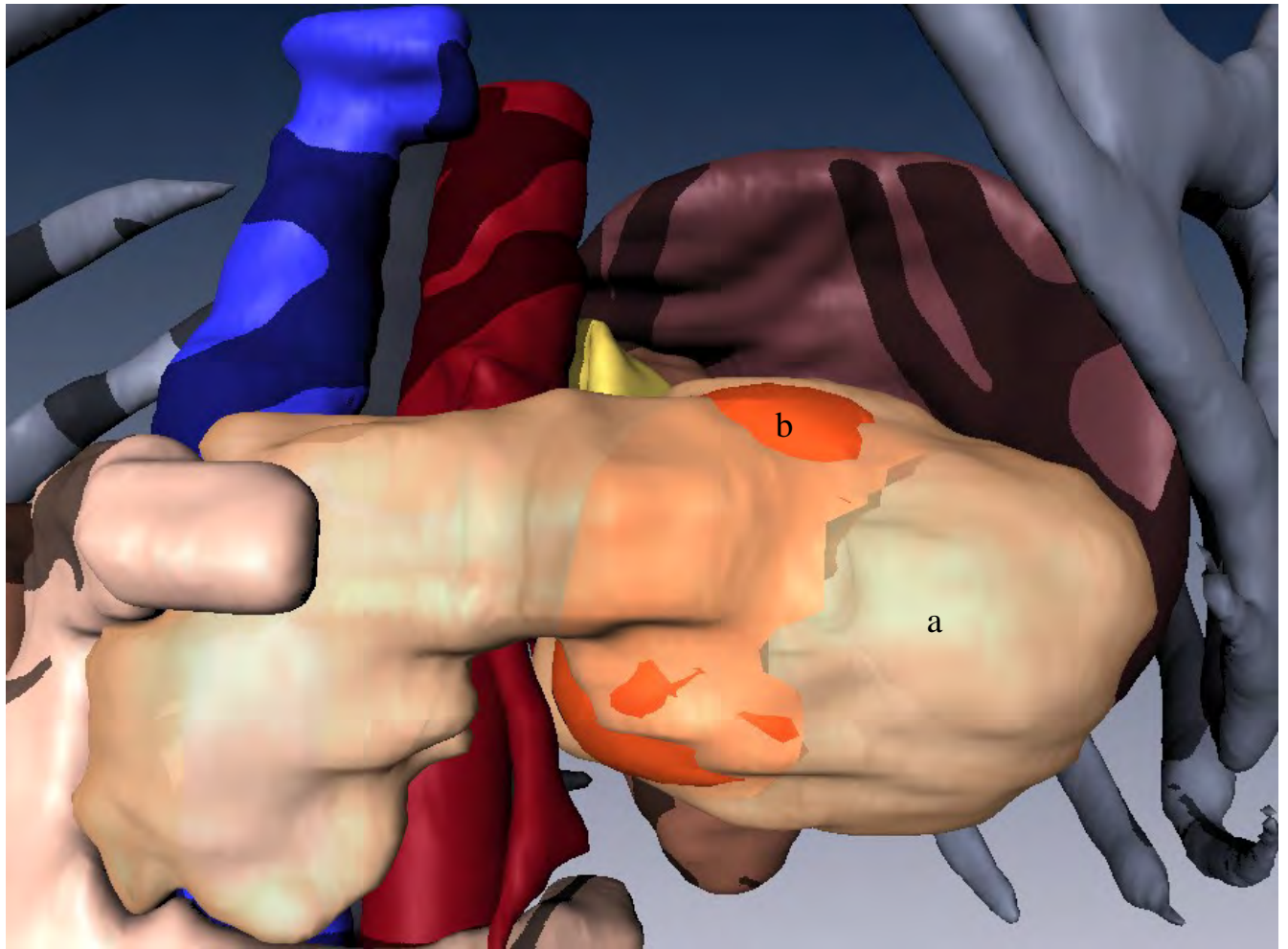
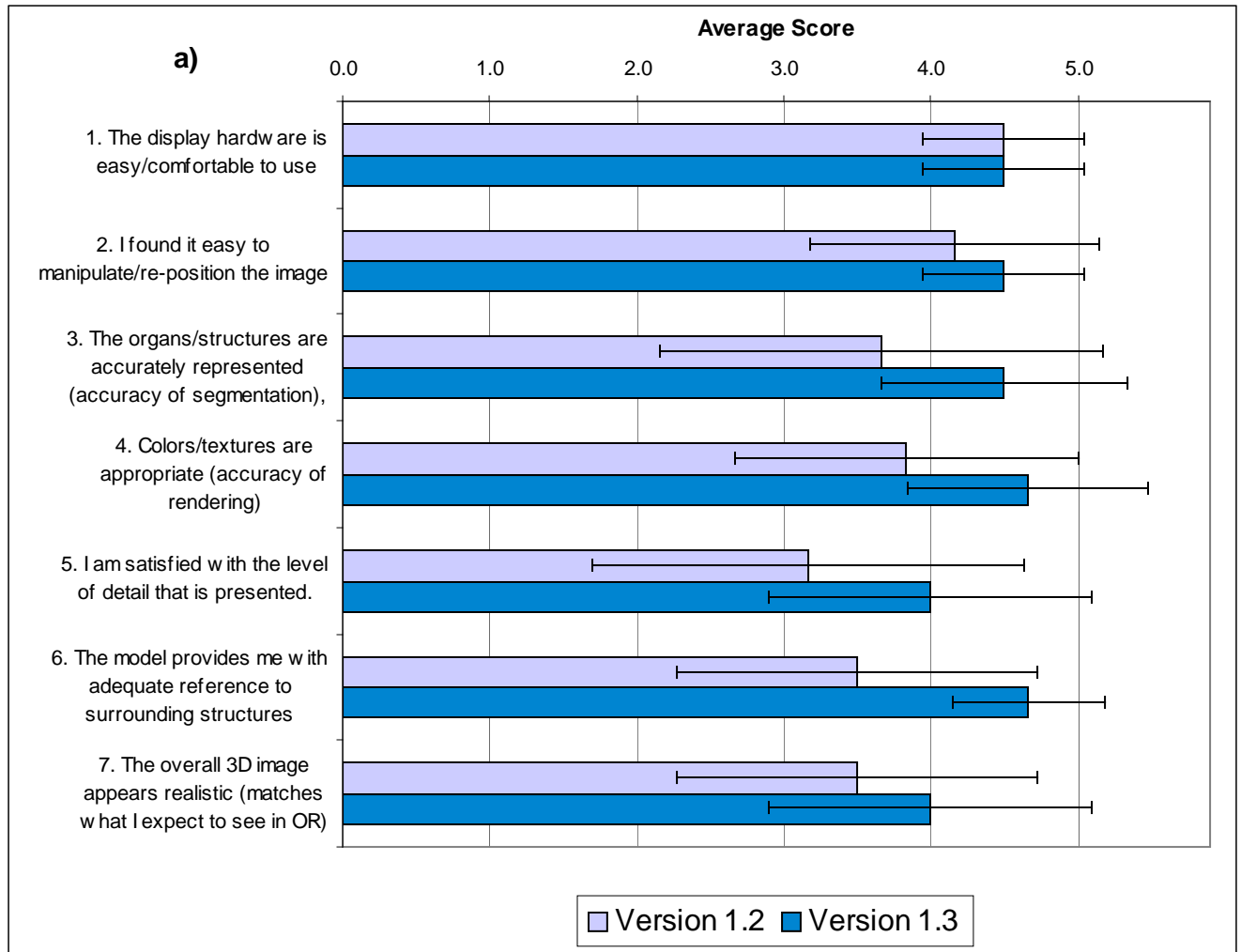
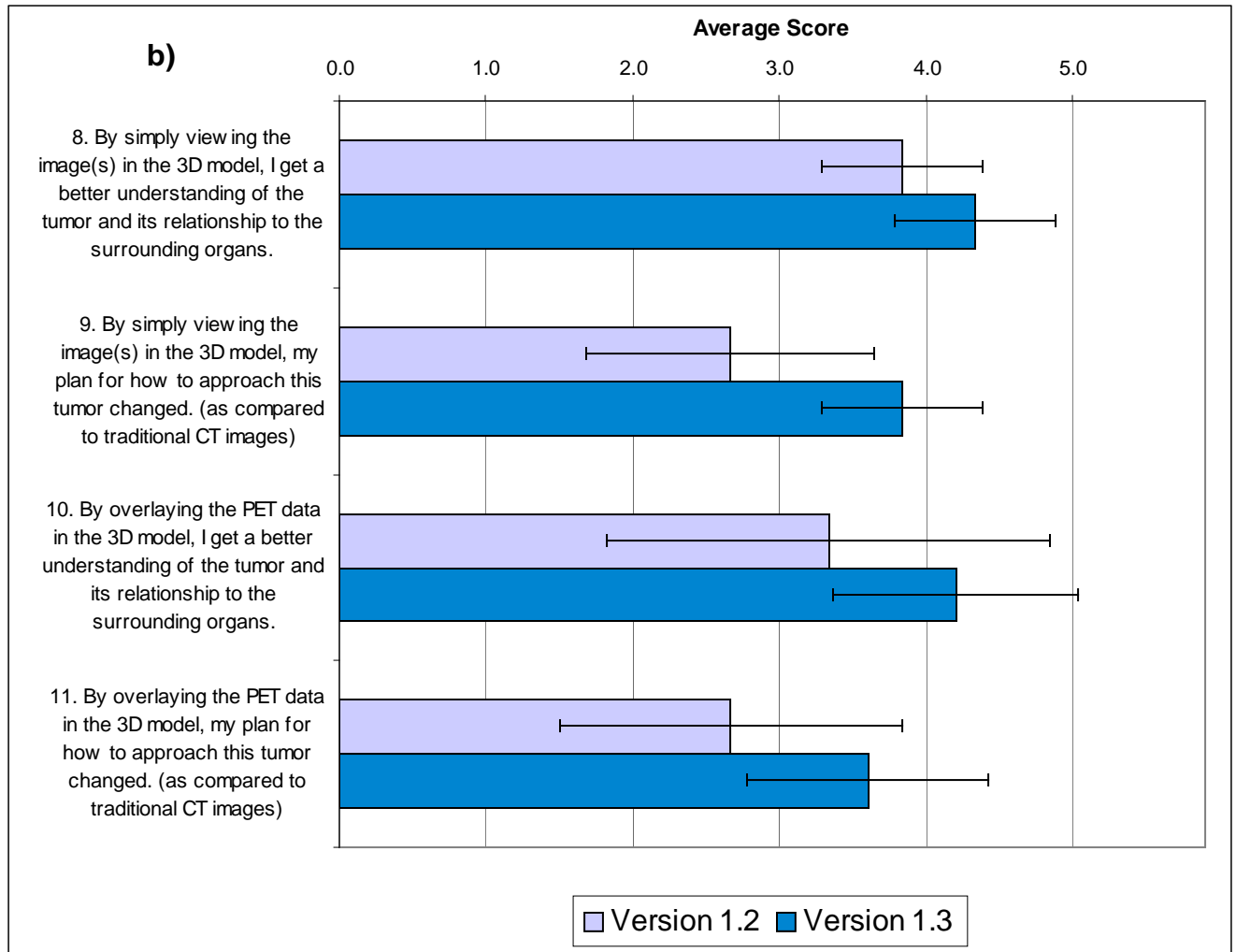


Figure 6: Image depicting a transparent overlay, in version 1.2, of the **a)** pancreas over the surface rendering of high uptake region of ^{18}F FDG in the **b)** pancreatic tumor (orange).





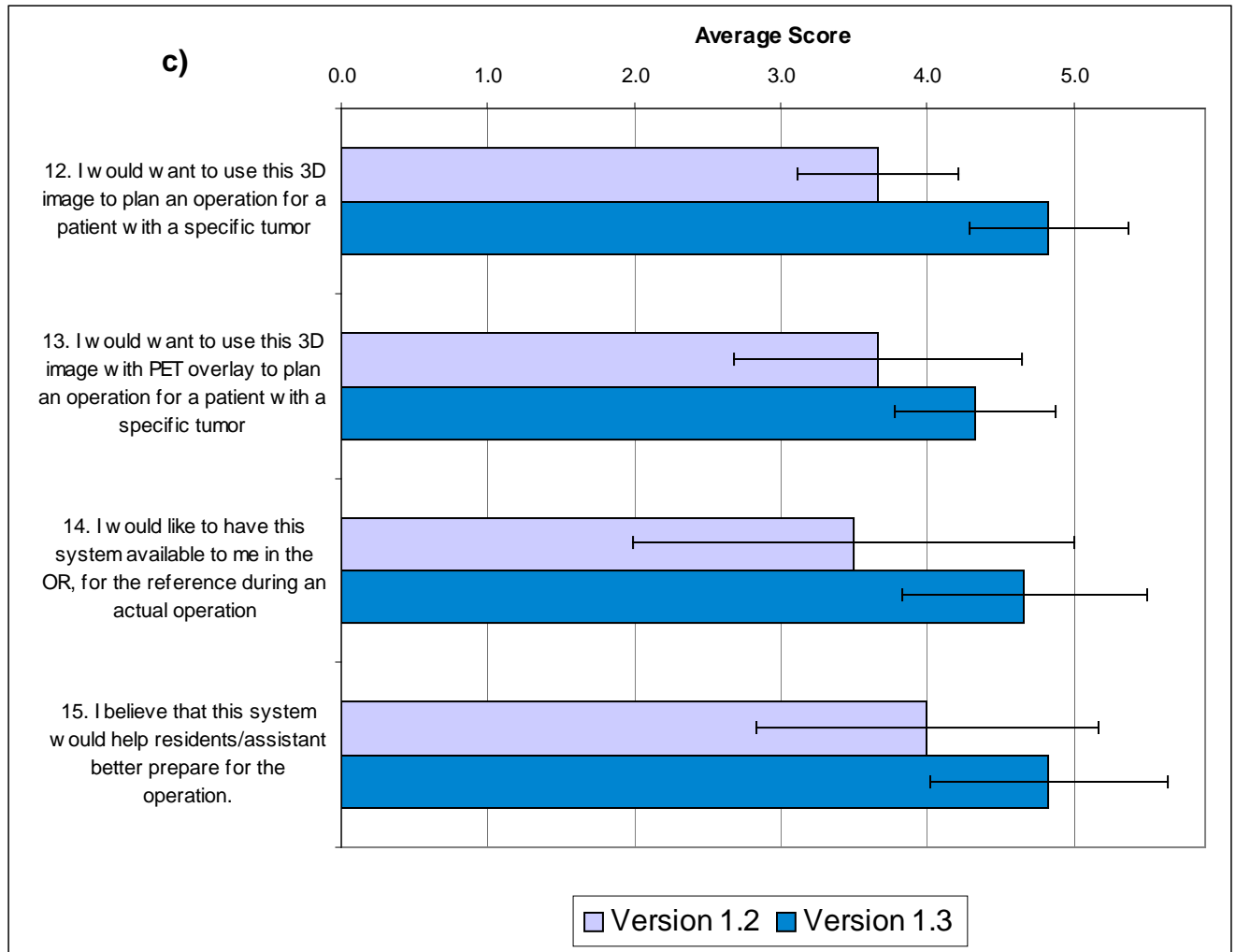


Figure 7: Average scores for version 1.2 and 1.3 of the visualization, with error bars, for questions on **a)** the ease of use and accuracy of models, **b)** whether viewing these models, with or without PET changed their understanding of the tumor, and **c)** what this type system would be applicable to.

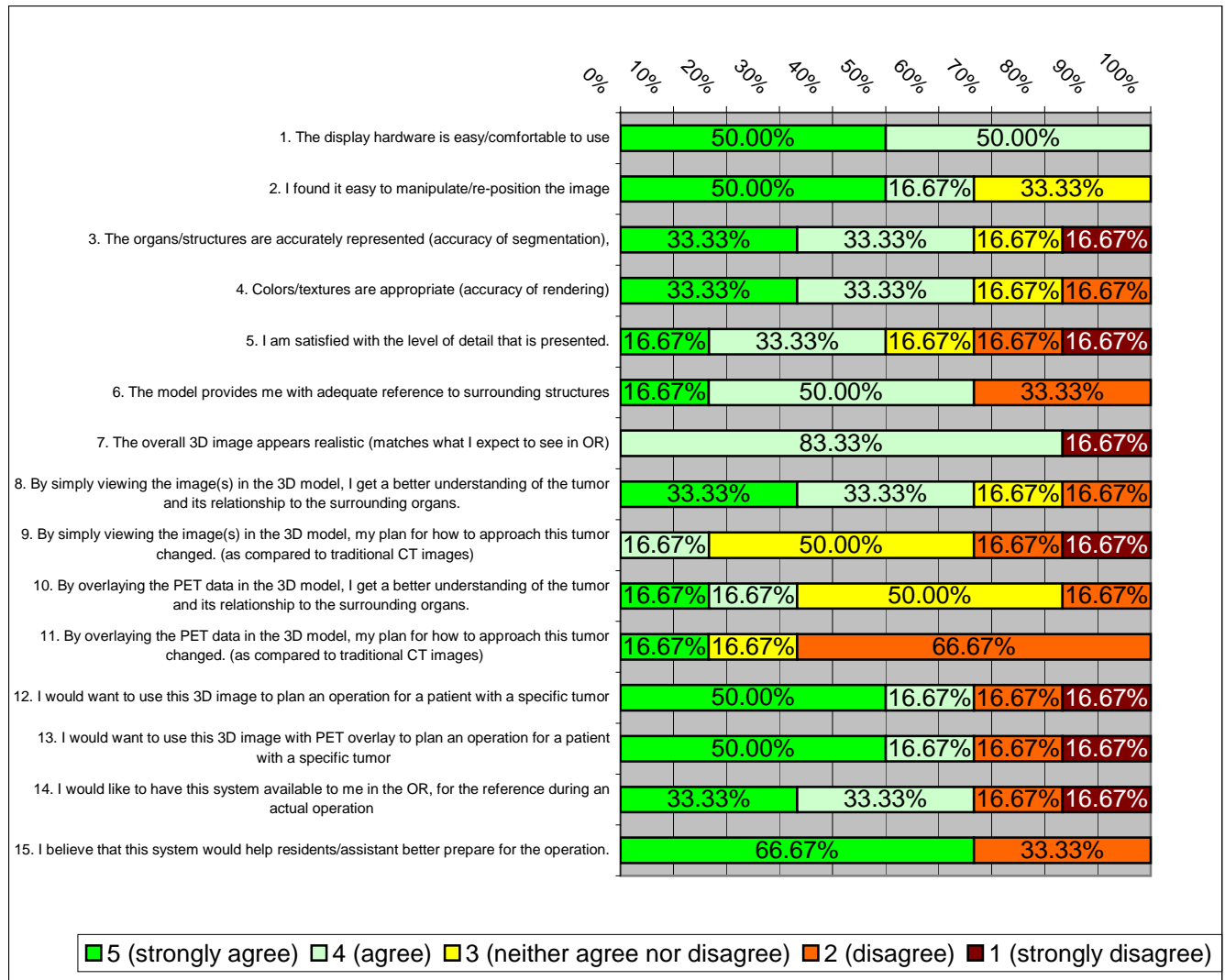


Figure 8: Distribution of surgeon scores in version 1.2 for each question and the percentage of surgeons that assigned that score.

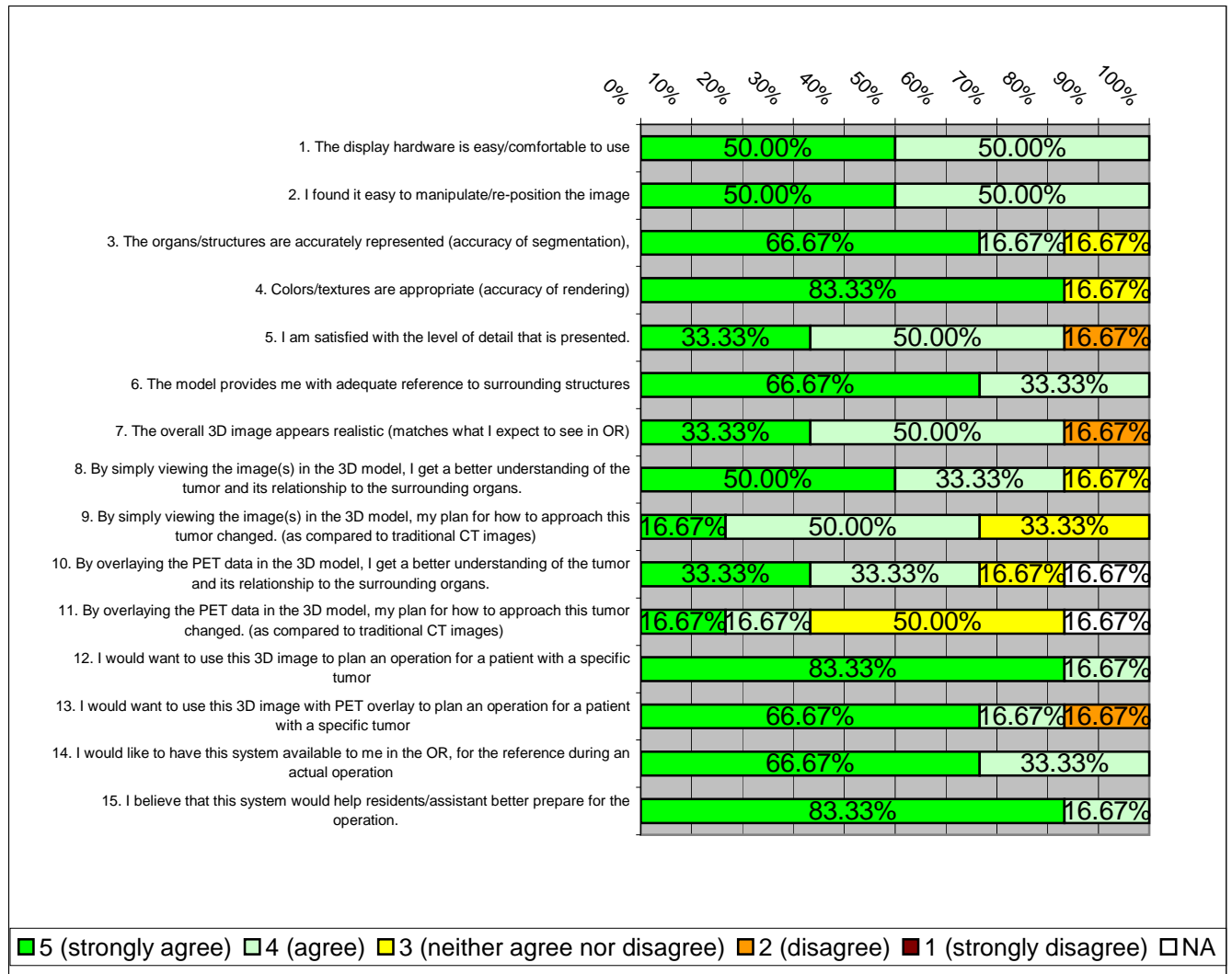


Figure 9: Distribution of surgeon scores in version 1.3 for each question and the percentage of surgeons that assigned that score.